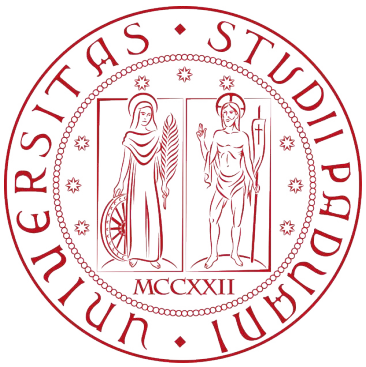

UNIVERSITÀ DEGLI STUDI DI PADOVA

Dipartimento di Fisica e Astronomia "Galileo Galilei"

Master Degree in Physics

Final Dissertation

Looking for axions in exotic, highly magnetised White Dwarf stars

Thesis supervisor

Prof. Luca Di Luzio

Thesis co-supervisor

Dr. Sebastian Hoof

Candidate

Ruben Zatini

Academic Year 2023/2024

"*E vi dico: lasciate ogni speranza,*
o voi che vi accingete a
osservare!"

Bertolt Brecht, *La vita di Galileo*

Abstract

The Peccei-Quinn (PQ) symmetry is a potential extension of the Standard Model that offers a compelling solution to the strong CP problem. This symmetry predicts the existence of a new pseudoscalar particle, the QCD axion, which, along with more general axion-like particles (ALPs), is also a viable dark matter candidate. This thesis focuses on the production of axions in highly magnetized white dwarfs (MWDs) through axion bremsstrahlung and their subsequent conversion into X-ray photons in the star's strong magnetic field. Since astrophysical processes are generally not expected to produce a similar signature, the observation of such a signal could provide strong evidence for the existence of axions. This thesis systematically outlines the procedure for constructing a template for the axion-induced X-ray signal expected from isolated MWDs and shows how this prediction can be used to conduct a statistical analysis of observational data to set constraints on axion interaction strengths. Numerical techniques are then employed to apply this analysis to data from MWD RE J0317-853 observed by the *Chandra* telescope, yielding axion bounds consistent with recent work by Dessert et al. (2019, '22). Finally, this thesis critically examines the currently used methodology and suggests possible extensions and improvements to obtain more accurate statistical inference on axion models with future data.

Contents

Introduction

The Standard Model (SM) of particle physics, despite its numerous successes, leaves many fundamental questions unanswered. These unresolved issues, such as the nature of dark matter and the strong CP problem, suggest the existence of new physics beyond the SM. Among the various proposed extensions, axion physics has recently seen growing interest within the scientific community. This is because it not only provides a compelling solution to two of modern physics' fundamental puzzles through an elegant theoretical framework but also holds promising potential for experimental verification. The QCD axion emerges as a low-energy remnant of a UV symmetry proposed by R. Peccei and H. Quinn (PQ symmetry) to explain the absence of CP violation in quantum chromodynamics (QCD), i.e. the strong CP problem. Additionally, it turns out that this hypothetical particle is also a good dark matter candidate, making its detection even more appealing, as it would "kill two birds with one stone".

From an effective field theory (EFT) perspective, this new pseudoscalar field needs only an axion-gluons vertex to tackle the strong CP problem. However, other couplings with SM fields are possible depending on the specific UV completion that realizes the PQ symmetry, resulting in a rich variety of proposed axion models. Of particular phenomenological interest is the axion interaction with photons, mediated by $g_{a\gamma\gamma}$, as many detection techniques rely on it. Along with it, non-hadronic axion models predict a tree-level coupling to electrons g_{aee}, which is crucial for the phenomenology examined in this thesis. However, the QCD axion is not the only pseudoscalar particle that can extend the SM. Axion-like particles (ALPs) also arise naturally in many extensions of the Standard Model. Although they are not related to the strong CP problem, ALPs share a similar phenomenology with the QCD axion, including interactions with photons and matter. In the following, we will use the term "axions" to refer to both the QCD axion and ALPs.

In this thesis, we will review recent works on axion searches based on X-ray

observations of white dwarf stars (WDs). These extreme astrophysical environments provide a unique observational window to investigate the properties of non-hadronic axion models, which are expected to be efficiently produced in the WD core. The resulting axion flux would partially convert into a potentially detectable flux of X-ray photons due to the interaction with the WD's strong natural magnetic field, providing a signature of the existence of axions. The primary goal of this work is to develop an analysis pipeline for X-ray astronomy data, utilizing Python to consistently perform the necessary numerical computations for WD modeling and data analysis. We will apply this pipeline to real observational data, ultimately setting stringent bounds on axion properties and demonstrating the effectiveness of X-ray observations of WDs as a tool for axion searches.

In chapter 1, we introduce the QCD axion as a solution to the strong CP problem, illustrating its elegant theoretical framework and focusing on two classes of benchmark UV models. In chapter 2, we shift to the phenomenology of the axion. Here, we present an overview of the axion emission processes occurring in astrophysical environments, provide a selection of the axion bounds obtainable from these processes, and prepare the reader for the following chapters, which form the core of the thesis. In chapter 3, we narrow our focus to white dwarfs as targets for axion detection, detailing step-by-step the analysis pipeline for X-ray observations. In chapter 4, we apply the developed procedure to observational data from the *Chandra* telescope observation of the nearby magnetic white dwarf (MWD) RE J0317-853, performing an analysis that sets stringent bounds on the product $g_{aee} \times g_{a\gamma\gamma}$. Finally, in chapter 5, we summarize these results and present our conclusions.

Throughout this work, we will always use natural units where $\hbar = c = k_B = 1$, so that all quantities involving dimensions of length, mass, and time are expressed in dimensions of power of eV. Additionally, for the definition of the dimensionless electric charge e, we will use rationalized units where $\alpha = e^2/4\pi \approx 1/137$ and therefore $e \approx 0.30$. However, depending on the context (astrophysics or laboratory physics), the magnetic field may be expressed in different units. In some cases, it will be given in cgs units using "Gauss", which belongs to an unrationalized system. In other cases, it will be given in "Tesla", which belongs to the SI, a rationalized unit system. Remembering that $1\,\mathrm{T} = 10^4\,\mathrm{G}$, for all calculations involving the magnetic field, the correct formulae will be utilized.

Chapter 1

Axion as a solution to the strong CP problem

In this chapter, we aim to guide the reader through the theoretical motivation behind the introduction of the axion, starting by describing its historical roots and the context in which it was first proposed. In section 1.1, we introduce the so-called $U(1)_A$ problem through the analysis of the QCD Lagrangian, exploring how its resolution consequently leads to the strong CP problem, a significant puzzle in the Standard Model of particle physics. In section 1.2, we present the QCD axion from an EFT point of view, justifying it as a low-energy remnant within the Peccei-Quinn framework, which offers a compelling solution to the strong CP problem. Section 1.3 is dedicated to an overview of possible UV completion models that realize the PQ symmetry, examining various theoretical constructions and their implications for axion physics.

1.1 The QCD axial anomaly

Let us start by writing the Lagrangian of QCD:

$$\mathcal{L}_{\text{QCD}} = \sum_{k=\substack{\text{SM}\\\text{quarks}}} \left(\bar{q}_k i \not{D} q_k - m_k \bar{q}_k q_k + \text{h.c.}\right) - \frac{1}{4} G^a_{\mu\nu} G^{a\,\mu\nu}, \tag{1.1}$$

where we have defined

$$D_\mu = \partial_\mu - ig_s T^a A^a_\mu, \tag{1.2}$$

$$T^a = \frac{\lambda^a}{2}, \tag{1.3}$$

$$G_{\mu\nu} = \partial_\mu A_\nu - \partial_\nu A_\mu + if^{abc} A^b_\mu A^c_\nu, \tag{1.4}$$

where g_s is the strong coupling constant, T^a are the eight generators of the $SU(3)_C$ group, conventionally taken as $T^a = \lambda^a/2$, where λ^a are the Gell-Mann matrices; and f^{abc} are the structure constants of $SU(3)$. In the limit of massless quarks, the Lagrangian in eq. (1.1) enjoys a large global symmetry $U(N)_R \otimes U(N)_L = U(N)_V \otimes U(N)_A$ with N the number of quark flavors. Looking at the mass spectrum of the QCD Lagrangian, we immediately notice a significant energy separation between the masses of the SM quarks. In particular, if we focus only on the u and d quarks, it is sensible to consider the massless limit, since $m_u, m_d \ll \Lambda_{\rm QCD}$. Therefore, we can write the corresponding light quark Lagrangian as follows:

$$\mathcal{L}^{light}_{\rm QCD} = \sum_{k=u,d} \bar{q}_k i \not{D} q_k. \tag{1.5}$$

This Lagrangian enjoys a chiral symmetry $U(2)_R \otimes U(2)_L \simeq SU(2)_V \otimes SU(2)_A \otimes U(1)_V \otimes U(1)_A$ symmetry, where the identification holds because of the isomorphism between the algebras $U(N) \simeq SU(N) \otimes U(1)$. The non-vanishing quark condensate $\langle \bar{q}_k q_k \rangle \neq 0$ spontaneously breaks the symmetry group $U(2)_R \otimes U(2)_L \to SU(2)_V \otimes U(1)_V$. The remaining $U(1)_V \equiv U(1)_B$ symmetry corresponds to baryon number conservation, while $SU(2)_V \equiv SU(2)_I$ is the isospin symmetry. Indeed, it is an experimental fact that $SU(2)_I \otimes U(1)_B$ is a good approximate symmetry of nature, as isospin multiplets appear in the hadron spectrum. The Goldstone theorem tells us that, when global continuous symmetry is spontaneously broken, a spin-0 massless field—the so-called Goldstone boson (GB)—is expected to appear for each generator of the broken symmetry. In the case of a spontaneously broken axial $U(2)_A \simeq SU(2)_A \otimes U(1)_A$, we would therefore expect to see four GBs. What we actually observe are three light pseudoscalar particles, the pions, and an additional particle, the η meson, which, however, has a significantly larger mass. Including the s quark in the QCD chiral symmetry yields a similar phenomenology in the hadronic spectrum, with eight lighter mesons ($\pi^0, \pi^\pm, \eta, K^0, \bar{K}^0, K^\pm$)—corresponding to the $SU(3)_A$ generators—and a ninth significantly more massive meson, the η'. The absence of a ninth Goldstone boson in the hadronic spectrum suggests that

the axial $U(1)_A$ symmetry was never a true symmetry for strong interactions. Indeed, it can be seen that axial transformations on quark fields

$$q_k \to e^{i\alpha\gamma_5} q_k \tag{1.6}$$

are anomalous for the QCD Lagrangian in eq. (1.5), meaning the symmetry is not conserved at the quantum level. For this reason, the corresponding axial current receives a contribution:

$$\partial_\mu J^\mu_A = \frac{g_s^2 N}{16\pi^2} G^a_{\mu\nu} \widetilde{G}^{a\,\mu\nu}, \tag{1.7}$$

where N is the number of fields involved in the axial transformation, i.e. the number of massless quarks. Here we have also introduced the dual gluon field strength

$$\widetilde{G}^a_{\mu\nu} = \frac{1}{2} \varepsilon_{\mu\nu\rho\sigma} G^{a\,\rho\sigma}, \tag{1.8}$$

with the choice $\varepsilon^{0123} = -1$. This anomalous effect can be traced back to the non-invariance of the quark fields path integral measure [1] under the transformation in eq. (1.6)

$$\mathcal{D}q_k \mathcal{D}\bar{q}_k \to \left(e^{-i\alpha \frac{g_s^2}{16\pi^2} \int d^4x\, G^a_{\mu\nu} \widetilde{G}^{a\,\mu\nu}} \right) \mathcal{D}q_k \mathcal{D}\bar{q}_k. \tag{1.9}$$

At first sight, the existence of such an anomaly seems to explain the observed phenomenology in the hadronic spectrum: there is no $U(1)_A$ symmetry to be broken and the Goldstone theorem does not apply. However, the term in eq. (1.7) can be expressed as a total derivative of the Chern-Simons current:

$$G^a_{\mu\nu} \widetilde{G}^{a\,\mu\nu} = \partial_\mu K^\mu = \partial_\mu \varepsilon^{\mu\alpha\beta\gamma} \left(A^a_\alpha G^a_{\beta\gamma} - \frac{g_s}{3} f^{abc} A^a_\alpha A^b_\beta A^c_\gamma \right), \tag{1.10}$$

and thus does not have any effect on the action in perturbation theory, leaving $U(1)_A$ a true symmetry for the action of Lagrangian in eq. (1.5). However, gauge invariance implies the existence of an infinite number of vacua for QCD, classified with the label $|n\rangle$ with $n \in \mathbb{Z}$. Moreover, it is possible to see that there exist configurations of the A_μ field—called *instantons*—that interpolate between different n-vacua and give a non-vanishing contribution to the QCD action, therefore breaking the $U(1)_A$ symmetry. As we will see in the next section, the resolution of this $U(1)$ problem leads directly to another puzzle known as the *strong CP problem*, which is the theoretical motivation to axion

physics.

1.2 The strong CP problem

The existence of instantons — i.e. configurations that connect different n-vacua — motivates the introduction of a θ parameter associated with the true vacuum of QCD $|\theta\rangle$, which is a linear combination of the different vacua $|n\rangle$. The presence of this vacuum, called the θ-vacuum, leads to the emergence of a new term in the QCD Lagrangian in eq. (1.1). This new term is a renormalizable operator compatible with Lorentz invariance and $SU(3)_C$ gauge symmetry:

$$\delta\mathcal{L}^{\theta}_{\text{QCD}} = \frac{g_s^2\theta}{32\pi^2} G^a_{\mu\nu}\widetilde{G}^{a\,\mu\nu}. \tag{1.11}$$

Equation (1.11), also called θ-term, violates P and T, and thus it also violates CP. However, this is not the only CP-violating contribution present in the QCD Lagrangian. In fact, the quark mass terms in eq. (1.1) were assumed to be real, but the more generally

$$m_q\bar{q}_L q_R + \text{h.c.} \to e^{i\theta_q} m_q \bar{q}_L q_R + \text{h.c.} \tag{1.12}$$

The presence of complex phases does not violate Lorentz symmetry or the $SU(3)_C$ gauge symmetry but does violate CP. Usually, this CP-violating term is neglected since it can be reabsorbed into a phase redefinition of the quark fields. However, it becomes important in this context because we also have the additional CP-violating operator in eq. (1.11). We need to quantify the observable impact of these new parameters θ and θ_q. In particular, we can show that only a combination of the two CP-violating parameters θ and θ_q constitutes a physical observable. In order to do so, let us perform an axial transformation $U(1)_A$ on a single quark field

$$q \to e^{i\alpha\gamma_5} q \qquad \text{i.e.} \qquad \begin{cases} q_L \to e^{-i\alpha} q_L \\ q_R \to e^{i\alpha} q_R \end{cases} . \tag{1.13}$$

Under this transformation, it is clear that the corresponding complex phase transforms as $\theta_q \to \theta_q + 2\alpha$. Nevertheless, this transformation also affects the θ-term. As we have shown in the previous section, the $U(1)_A$ symmetry is anomalous under QCD, so the divergence of the single quark axial current

reads:

$$\partial_\mu J_A^\mu = 2m_q i\bar{q}\gamma_5 q + \frac{g_s^2}{16\pi^2} G^a_{\mu\nu}\widetilde{G}^{a\,\mu\nu}. \tag{1.14}$$

Note that the second term has the same form of the θ-term in eq. (1.11). Hence, when performing an axial rotation, anomalous effects induce an additional modification of the Lagrangian proportional to the rotation angle α, resulting in a shift $\theta \to \theta - 2\alpha$. Therefore the linear combination $\bar{\theta} = \theta + \theta_q$ is invariant under a single quark axial transformation. To find the general expression for the physically observable parameter $\bar{\theta}$, one must extend this procedure to generic axial transformations acting on the flavor space. Calling q a quark flavor multiplet of N_f flavors, the mass term in the QCD Lagrangian reads

$$\mathcal{L}^{quark}_{\rm QCD} \supset -\bar{q}_L M_q q_R + \text{h.c.}\,, \qquad M_q = \underbrace{\begin{pmatrix} m_u & & \\ & m_d & \\ & & \ddots \end{pmatrix}}_{N_f}. \tag{1.15}$$

Performing an axial transformation in the flavor space through a $N_f \times N_f$ diagonal matrix Q_a acting on the quark fields

$$q \to e^{i\alpha\gamma_5 Q_a} q, \tag{1.16}$$

the phase of the mass matrix undergoes a shift $M_q \to M_q e^{i2\alpha Q_a}$, or more explicitly

$$\arg\det M_q \to \arg\det M_q e^{i2\alpha Q_a} = \arg\det M_q + 2\alpha\,\mathrm{Tr}\,Q_a. \tag{1.17}$$

One can see that resulting from this transformation, the anomalous shift in the Lagrangian corresponds to the following transformation of the theta term

$$\theta \to \theta - 2\alpha\,\mathrm{Tr}\,Q_a. \tag{1.18}$$

Consequently, the physical observable quantity $\bar{\theta}$ that is invariant under the more general transformation in eq. (1.16) is

$$\bar{\theta} = \theta + \arg\det M_q \tag{1.19}$$

$$= \theta + \arg\det Y_u Y_d \quad \text{in the EW theory.} \tag{1.20}$$

As a result, all the CP-violating effects of the QCD Lagrangian depend on the size of $\bar{\theta}$. Since $\bar{\theta}$ is the sum of two unrelated dimensionless contributions, we might expect it to be of order one. One of the physical observables induced by the presence of CP violation is a non-vanishing neutron electric dipole moment (nEDM). Experiments aimed at measuring the nEDM, without finding it, imply a strong bound on $\bar{\theta}$ size [2], [3]:

$$|d_n|^{\text{exp}} < 1.8 \times 10^{-26}\, e\,\text{cm} \quad \text{at } (2\sigma), \tag{1.21}$$

leading to

$$|\bar{\theta}| < 10^{-10}. \tag{1.22}$$

This extremely small value of $\bar{\theta}$ would thus correspond to a non-trivial cancellation between the two independent quantities in eq. (1.19), thereby raising the so-called *strong CP problem*. In the next section, we will explore a possible solution to this problem, which involves introducing a new chiral symmetry that drives the CP-violating $\bar{\theta}$ term to zero.

1.2.1 The Peccei-Quinn solution and the QCD axion

Among all possible solutions to the strong CP problem, the Peccei-Quinn (PQ) solution is particularly significant, since, as we will see shortly, it leaves a low-energy remnant—*the QCD axion*—which can be experimentally tested.

The PQ solution involves postulating the existence of a new global axial symmetry $U(1)_{\text{PQ}}$, which must satisfy two conditions. First, this symmetry must be anomalous with respect to QCD, allowing the $\bar{\theta}$-term in eq. (1.11) to be absorbed by an anomalous contribution of the type shown in eq. (1.7). Second, the symmetry must be spontaneously broken at a high energy scale, as it is not observed at the energy scales accessible in current experiments. When this happens, it results in a GB pseudoscalar called the QCD axion. From now on, we will refer to the QCD axion simply as the *axion*. The realization of the PQ symmetry is not unique, and numerous UV models incorporating it have been proposed. Some of these models will be discussed in section 1.3. Now we address the axion solution from a bottom-up perspective, and we introduce the axion field in the effective Lagrangian

$$\mathcal{L}_a = \frac{1}{2}(\partial_\mu a)^2 + \mathcal{L}(\partial_\mu a, \psi) + \frac{g_s^2}{32\pi^2}\frac{a}{f_a} G^a_{\mu\nu}\widetilde{G}^{a\,\mu\nu}, \tag{1.23}$$

where f_a is the energy scale of the EFT, also known as the axion decay con-

stant. Consequently, the Lagrangian enjoys a pseudo-shift symmetry:

$$a(x) \longrightarrow a(x) + \alpha f_a, \tag{1.24}$$

which induces a variation in the Lagrangian:

$$\delta\mathcal{L}^a_{\text{QCD}} = \frac{g_s^2\alpha}{32\pi^2} G^a_{\mu\nu}\widetilde{G}^{a\,\mu\nu}, \tag{1.25}$$

allowing the θ-term to be absorbed by the field redefinition $\alpha = -\,\bar{\theta}$. Remarkably, the Vafa-Witten theorem [4] ensures that $\langle a \rangle = 0$, i.e., the minimum of the axion potential is CP-conserving. Therefore QCD dynamics drives the axion to its minimum, eventually solving the strong CP problem. The same QCD dynamics, through the axion-gluon interaction term in eq. (1.23), causes the new particle to acquire a non-vanishing mass m_a. The fact that the axion is not massless does not conflict with the Goldstone theorem, as we constructed $U(1)_{\text{PQ}}$ as an anomalous symmetry from the beginning. The axion mass can be computed at low energy using the tools provided by *chiral perturbation theory* (χPT) and expressed in terms of well-understood hadron physics. Here, we limit ourselves to presenting the final result, referring to [5] for a comprehensive treatment:

$$m_a^2 = \frac{m_u m_d}{(m_u + m_d)^2}\frac{m_\pi^2 f_\pi^2}{f_a^2}, \tag{1.26}$$

where m_π is the pion mass, and f_π is a constant known from the pion decay rate via the weak interaction. Plugging the known values into eq. (1.26), we obtain

$$m_a \simeq 5.7 \left(\frac{10^{12}\,\text{GeV}}{f_a}\right) \mu\text{eV}. \tag{1.27}$$

Phenomenologically speaking, it is important to investigate what possible interactions the axion may have with the SM fields. To solve the strong CP problem, we have shown that the axion must interact with gluons, as indicated in eq. (1.23). However, in general, the $U(1)_{\text{PQ}}$ symmetry can also be anomalous with respect to QED. Therefore, it is necessary to include an axion-photon interaction term in eq. (1.23). Additionally, if SM fermions are PQ charged in the UV, we expect to see a derivative interaction between the axion and fermions. The axion effective Lagrangian can now be written as:

$$\mathcal{L}_a = \frac{1}{2}(\partial_\mu a)^2 + \frac{g_s^2}{32\pi^2}\frac{a}{f_a}G^a_{\mu\nu}\widetilde{G}^{a\,\mu\nu} + \frac{1}{4}g^0_{a\gamma\gamma}aF_{\mu\nu}\widetilde{F}^{\mu\nu} + \sum_f \frac{\partial_\mu a}{2f_a}c_f^0\bar{f}\gamma^\mu\gamma_5 f. \quad (1.28)$$

Here, $F_{\mu\nu}$ is the electromagnetic field strength tensor, $\widetilde{F}^{\mu\nu}$ is its dual, and f represents the SM fermions charged under $U(1)_{\rm PQ}$. The strength of the couplings $g^0_{a\gamma\gamma}$ and c_f^0 depends on the specific UV completion considered. Indeed, we can define E and N as the QED and QCD anomaly coefficients, respectively, so that the PQ current $J^{\rm PQ}_\mu$ is conserved up to the terms:

$$\partial^\mu J^{\rm PQ}_\mu = \frac{g_s^2 N}{16\pi^2}G^a_{\mu\nu}\widetilde{G}^{a\,\mu\nu} + \frac{e^2E}{16\pi^2}F_{\mu\nu}\widetilde{F}^{\mu\nu}. \quad (1.29)$$

After the breaking of the PQ symmetry, the axion Lagrangian will contain the terms:

$$\mathcal{L}_a \supset \frac{a}{v_{\rm PQ}}\frac{g_s^2 N}{16\pi^2}G^a_{\mu\nu}\widetilde{G}^{a\,\mu\nu} + \frac{a}{v_{\rm PQ}}\frac{e^2E}{16\pi^2}F_{\mu\nu}\widetilde{F}^{\mu\nu} + \frac{\partial^\mu a}{v_{\rm PQ}}J^{\rm PQ}_\mu, \quad (1.30)$$

where $v_{\rm PQ}$ is the order parameter of the $U(1)_{\rm PQ}$ symmetry breaking. Imposing in eq. (1.30) the normalization of the Lagrangian introduced in the axion EFT in eq. (1.28), we obtain:

$$f_a = \frac{v_{\rm PQ}}{2N}, \qquad g^0_{a\gamma\gamma} = \frac{\alpha_{\rm EM}}{2\pi f_a}\frac{E}{N}, \qquad c_f^0 = \frac{X_{H_f}}{2N}, \quad (1.31)$$

where for the expression of the axion-fermion coupling we have supposed that the fermion fields receive their masses through a Yukawa term with suitable Higgs fields $\bar{f}_L f_R H_f$. In the next section, we will see explicitly how these terms emerge from the specific UV completion considered. However, It is important to point out that interaction terms between axions and quarks, as well as between axions and photons, emerge regardless of the specific UV model. This can be seen by performing a field-dependent axial transformation of the quark fields to absorb the axion-gluon interaction term in eq. (1.28):

$$q \to e^{i\gamma_5\frac{a}{2f_a}Q_a}q, \quad (1.32)$$

where Q_a is a generic matrix acting on the quark fields. As already said, axial transformations are QCD anomalous, so eq. (1.32) modifies the axion effective Lagrangian in eq. (1.28) with:

$$\delta\mathcal{L}_a^{\rm QCD} = -\frac{a}{f_a}\frac{g_s^2}{32\pi^2}\,\mathrm{Tr}(Q_a)G^a_{\mu\nu}\widetilde{G}^{a\,\mu\nu}. \tag{1.33}$$

Thus, it is possible to rotate away the axion-gluon term by requiring that $\mathrm{Tr}\,Q_a = 1$. Following this field redefinition, the quark kinetic term generates an additional axion-quark interaction term, allowing us to define new axion couplings c_q for the quarks involved in the rotation. Moreover, an extra axion-photon coupling arises because this transformation is also QED anomalous, generating a new $aF_{\mu\nu}\widetilde{F}^{\mu\nu}$ term. One can see that the transformation in eq. (1.32) corresponds to the new couplings:

$$\begin{aligned} c_q &\equiv c_q^0 - Q_a, \\ g_{a\gamma\gamma} &\equiv g^0_{a\gamma\gamma} - (2N_c)\frac{\alpha}{2\pi f_a}\,\mathrm{Tr}\left(Q_a Q_{\rm EM}^2\right), \end{aligned} \tag{1.34}$$

where $Q_{\rm EM}$ is the charge matrix of the quarks involved in the transformation, and N_c is the number of colors. The coupling with the electron, however, does not receive this type of contribution since it is not involved in the axial rotation in eq. (1.32). Notably, the coupling c_e^0 receives a radiative contribution δc_e due to a photon loop, which allows us to write:

$$c_e \equiv c_e^0 + \delta c_e, \tag{1.35}$$

with

$$\delta c_e = \frac{3\alpha^2}{4\pi^2}\left[\frac{E}{N}\log\left(\frac{f_a}{\mu_{\rm IR}}\right) - \frac{2}{3}\frac{4m_d + m_u}{m_u + m_d}\log\left(\frac{\Lambda_\chi}{\mu_{\rm IR}}\right)\right]. \tag{1.36}$$

The first term is associated with the running of the axion-electron coupling from f_a to $\mu_{\rm IR}$, while the second term arises from the axion-pion mixing and is cut off at the χPT breaking scale, approximately $\Lambda_\chi \sim 1\,\mathrm{GeV}$. The parameter $\mu_{\rm IR}$ denotes the energy scale of the physical process, typically $\mu_{\rm IR} \sim m_e$.

Finally, the axion Lagrangian reads:

$$\mathcal{L}_a = \frac{1}{2}(\partial_\mu a)^2 + \frac{1}{4}g_{a\gamma\gamma}aF_{\mu\nu}\widetilde{F}^{\mu\nu} + \sum_f \frac{\partial_\mu a}{2f_a}c_f\bar{f}\gamma^\mu\gamma_5 f. \tag{1.37}$$

These interactions between axion and SM particles are crucial from an experimental point of view, because, as we will see in chapter 2, they enrich the phenomenology of the axion, providing channels for its potential detection.

1.3 Axion models

In this section, we aim to analyze some specific axion models that realize the PQ symmetry in the UV. The simplest UV completion that can be constructed is the PQWW axion model [6]–[9]. The symmetry is realized with two Higgs doublets and the SM quarks, which interact in a Yukawa term:

$$\mathcal{L}_Y = Y_U \bar{q}_L H_u u_R + Y_D \bar{q}_L H_d d_R + \text{h.c.} \tag{1.38}$$

By enforcing the $U(1)_{\text{PQ}}$ symmetry on this term, the PQ charges of the Higgs and quark fields are fixed. The two Higgs fields develop non-vanishing vacuum expectation values (VEVs) $v_u, v_d \neq 0$ through a symmetry-breaking potential:

$$V(H_u, H_d) = \lambda_u \left(|H_u|^2 - \frac{v_u^2}{2} \right)^2 + \lambda_d \left(|H_d|^2 - \frac{v_d^2}{2} \right)^2 + \tilde{V}(|H_u|, |H_d|, |H_u H_d|), \tag{1.39}$$

where $\tilde{V}(|H_u|, |H_d|, |\Phi|, |H_u H_d|)$ contains terms that do not break the PQ symmetry explicitly. In the broken phase, the axion emerges as a combination of the two angular modes of H_u and H_d exponential representations. Since it is contained in the Higgs fields, the axion decay constant will be proportional to the electroweak scale, $v \simeq 246$ GeV. More precisely, it turns out that $f_a = (v/6) \sin 2\beta$, with $\tan\beta = v_u/v_d$. However, high-energy physics experiments ruled out the PQWW model since the small value of f_a does not sufficiently suppress the axion interaction with SM fields. Decay processes of K, J/Ψ, and Υ [10]–[12] put constraints on the axion-quark coupling, which are incompatible with the small PQWW axion decay constant f_a. Therefore, the only viable models are those that require light, weakly interacting axions, where $f_a \gg v$. These models are commonly referred to as *invisible axion models*.

1.3.1 KSVZ models

The KSVZ model [13], [14] is the simplest invisible axion model that one can build. In its most basic form, this model requires the introduction of a new vector-like quark field $Q = Q_L + Q_R$ that transforms under the fundamental representation of $SU(3)_C$, is a singlet under $SU(2)_L$, and is neutral under $U(1)_Y$. Thus, it transforms under the representation $Q \sim (3, 1, 0)$. Along with

this field, a new complex scalar field Φ is introduced with the SM representation $\Phi \sim (1,1,0)$, and it is used to give mass only to the new field Q. The most general renormalizable Lagrangian of this model is:

$$\mathcal{L}_{\text{KSVZ}} = \bar{Q} i \not{\partial} Q + \partial_\mu \Phi^\dagger \partial^\mu \Phi - V(\Phi) + y_Q \Phi \bar{Q}_L Q_R + \text{h.c.} \tag{1.40}$$

These two fields are the only two degrees of freedom charged under the $U(1)_{\text{PQ}}$ symmetry and transform as:

$$\Phi \to e^{i\alpha}\Phi, \quad Q \to e^{-i\alpha/2} Q. \tag{1.41}$$

The potential $V(\Phi)$ is the typical mexican-hat potential

$$V(\Phi) = \lambda_\Phi \left(|\Phi|^2 - \frac{v_{\text{PQ}}^2}{2} \right)^2, \quad \lambda_\Phi > 0. \tag{1.42}$$

This potential spontaneously breaks the symmetry at an energy scale v_{PQ}. Using the standard exponential parametrization of Φ:

$$\Phi = \frac{v_{\text{PQ}} + \rho}{\sqrt{2}} e^{ia/v_{\text{PQ}}}\,, \tag{1.43}$$

we observe the mass spectrum in the broken phase:

$$m_\rho = \sqrt{2\lambda} v_{\text{PQ}}, \quad m_a = 0, \quad m_Q = y_Q \frac{v_{\text{PQ}}}{\sqrt{2}}. \tag{1.44}$$

Requiring $v_{\text{PQ}} \gg v$, the radial mode gets a very large mass and we can integrate it out. In the broken phase, the interaction term reads:

$$\mathcal{L} = -m_Q \bar{Q}_L Q_R e^{ia/v_{\text{PQ}}} + \text{h.c.} \tag{1.45}$$

Through an axion-dependent axial field redefinition,

$$Q \to e^{-i\gamma_5 \frac{a}{2v_{\text{PQ}}}} Q\,, \tag{1.46}$$

we can disentangle the new quark field Q from the axion a and then integrate it out. As a consequence of the axial transformation, the action undergoes a shift:

$$\delta S = \frac{g_s^2}{32\pi^2} \int d^4x \, \frac{a}{v_{\text{PQ}}} G^a_{\mu\nu} \widetilde{G}^{a\,\mu\nu}, \tag{1.47}$$

which results in the axion-gluon term that we have introduced in the EFT in eq. (1.28). By comparing the two Lagrangians, it is possible to match the two

energy scales $v_{\rm PQ} = f_a$. In this simple model, there are no additional model-dependent tree-level interactions with other Standard Model fields, namely $g^0_{a\gamma\gamma} = 0$ and $c^0_f = 0$ for the couplings in eq. (1.28). However, it is possible to introduce an interaction with photons by considering a vector-like quark Q charged under electromagnetism. More broadly, if the field Q transforms under a more general representation $Q \sim (C_Q, I_Q, Y_Q)$, defining $d(I_Q)$ and $d(C_Q)$ the dimension of $SU(3)_C$ and $SU(2)_L$ representation we get the anomaly coefficients introduced in eq. (1.29):

$$E = X_Q \cdot d(I_Q) \cdot T(C_Q) \ , \tag{1.48}$$

$$N = X_Q \cdot d(I_Q) \cdot \mathrm{Tr}\, q_Q^2 \ , \tag{1.49}$$

where X_Q and q_Q are respectively the PQ charge and EM charge of the heavy quark field Q; and $T(C_Q)$ is the color Dynkin index. Hence these models allow for a tree-level coupling with photons $g^0_{a\gamma\gamma}$ (motivated ranges for this coupling can be found in [15]–[17]). However, since no SM fermion carries a PQ charge, we always have a vanishing model-dependent tree-level axion coupling with fermions $c^0_f = 0$. On the other hand, the axion-gluon interaction term makes possible an interaction with hadrons, this is why these axion models are called *hadronic*.

1.3.2 DFSZ models

Another benchmark model for the invisible axion is the DFSZ model [18], [19]. Like the PQWW model, it utilizes a two-Higgs-doublet model (2HDM) to give mass to the SM quarks and extends it with a complex scalar field. Therefore, the SM particle content extension is:

$$H_u \sim (1, 2, -1/2), \quad H_d \sim (1, 2, 1/2), \quad \Phi \sim (1, 1, 0). \tag{1.50}$$

These complex scalar fields, along with the quark and lepton fields, are all charged under the PQ symmetry, which acts on the scalar sector as

$$H_u \to e^{iX_{H_u}\alpha} H_u, \quad H_d \to e^{iX_{H_d}\alpha} H_d, \quad \Phi \to e^{iX_\Phi \alpha}\Phi. \tag{1.51}$$

Setting to zero the PQ charges of left-handed fermions, the $U(1)_{\rm PQ}$ transfor-

mation acts on fermion fields as

$$q_L \to q_L, \quad l_L \to l_L, \quad u_R \to e^{iX_u\alpha}u_R, \quad d_R \to e^{iX_d\alpha}d_R, \quad e_R \to e^{iX_e\alpha}e_R, \tag{1.52}$$

with α the rotation angle. The action of the PQ symmetry on the fermion fields is determined by the Yukawa Lagrangian. We distinguish now between two different DFSZ models, the DFSZ type I and II, which differ on the choice of the Higgs doublet giving mass to electrons. Defining $\tilde{H}_u = i\sigma_2 H_u^*$ the Yukawa Lagrangian reads

$$\mathcal{L}^Y_{\text{DFSZ-I}} = -Y_U \bar{q}_L u_R H_u - Y_D \bar{q}_L d_R H_d - \begin{cases} Y_E \bar{l}_L e_R H_d + \text{h.c.} & \text{DFSZ I} \\ Y_E \bar{l}_L e_R \tilde{H}_u + \text{h.c.} & \text{DFSZ II} \end{cases}, \tag{1.53}$$

requiring the PQ invariance in the two versions of eq. (1.53) we find

$$X_u = -X_{H_u}, \quad X_d = -X_{H_d}, \quad X_e = \begin{cases} -X_{H_d} & \text{DFSZ I} \\ X_{H_u} & \text{DFSZ II} \end{cases}, \tag{1.54}$$

We will focus now on describing the DFSZ-I model, while keeping in mind that the DFSZ-II is recovered by simply replacing $X_{H_d} \to -X_{H_u}$. Introducing a suitable scalar potential

$$V(H_u, H_d, \Phi) = \tilde{V}(|H_u|, |H_d|, |\Phi|, |H_u H_d|) - \lambda H_u H_d \Phi^2 + \text{h.c.} \tag{1.55}$$

we can ensure that all three scalar fields pick up a VEV:

$$\langle H_u \rangle = v_u, \quad \langle H_d \rangle = v_d, \quad \langle \Phi \rangle = v_\Phi. \tag{1.56}$$

The electroweak VEV is $v \simeq 246$ GeV, with $v^2 = v_u^2 + v_d^2$ and $\tan\beta = v_u/v_d$. In the KSVZ model, the axion was associated with the radial mode of the Φ field. Here it is not trivial to identify the axion as the extra term in the potential $V \supset -\lambda H_u H_d \Phi^2$ introduces a projection of the axion also along H_u and H_d. After symmetry breaking, the scalar fields take the values:

$$H_u = \frac{v_u}{\sqrt{2}} e^{i\frac{a_u}{v_u}} \begin{pmatrix} 0 \\ 1 \end{pmatrix}, \quad H_d = \frac{v_d}{\sqrt{2}} e^{i\frac{a_d}{v_d}} \begin{pmatrix} 1 \\ 0 \end{pmatrix}, \quad \Phi = \frac{v_\Phi}{\sqrt{2}} e^{i\frac{a_\Phi}{v_\Phi}}, \tag{1.57}$$

so that the axion is a general combination of the scalar fields' radial modes $a = f(a_u, a_d, a_\Phi)$. By enforcing the Goldstone theorem:

$$\langle 0|J_\mu^{\rm PQ}|a(p)\rangle = iv_{\rm PQ}p_\mu, \tag{1.58}$$

one can see that the axion field is compatible with the definition:

$$a = \frac{1}{v_{\rm PQ}} \sum_{i=H_u,H_d,\Phi} X_i v_i a_i, \quad \text{with} \quad v_{\rm PQ}^2 = \sum_{i=H_u,H_d,\Phi} X_i^2 v_i^2. \tag{1.59}$$

We then need to find an expression for the PQ charges X_i of the scalar sector. By imposing the PQ invariance of $V \supset -\lambda H_u H_d \Phi^2$, and demanding that the PQ current does not couple to the Goldstone boson that is eaten by the Z boson, we obtain:

$$X_\Phi = 1, \quad X_{H_u} = -2\cos^2\beta, \quad X_{H_d} = -2\sin^2\beta, \tag{1.60}$$

where we have exploited the freedom of choosing the value of one of the scalar PQ charges to be one. Now it is possible to invert the relation in eq. (1.59) and obtain an expression for a_u and a_d in terms of a, $v_{\rm PQ}$, and the charges X_{H_u} and X_{H_d}. Then, in the broken phase, the Yukawa Lagrangian reads:

$$\mathcal{L}_{\rm DFSZ}^Y \supset -m_U \bar{u}_L u_R e^{iX_{H_u}\frac{a}{v_{\rm PQ}}} - m_D \bar{d}_L d_R e^{iX_{H_d}\frac{a}{v_{\rm PQ}}} - m_E \bar{e}_L e_R e^{iX_{H_d}\frac{a}{v_{\rm PQ}}} + \text{h.c.} \tag{1.61}$$

Now it is possible to rotate away the axion field a through a set of fermionic axial transformations, generating the QCD and QED anomalous shifts in eq. (1.29). It turns out that for the DFSZ-I model $E = 8$, $N = 3$, while for the DFSZ-II one obtains $E = 2$, $N = 3$.
These transformations also affect the fermionic kinetic terms, leading to the axion-fermion couplings c_f^0 shown in eq. (1.28):

$$c_{u_i}^0 = \frac{1}{3}\cos^2\beta, \quad c_{d_i}^0 = \frac{1}{3}\sin^2\beta, \quad c_{e_i}^0 = \begin{cases} \frac{1}{3}\sin^2\beta & \text{DFSZ I} \\ -\frac{1}{3}\cos^2\beta & \text{DFSZ II} \end{cases}, \tag{1.62}$$

where $i = 1, 2, 3$ is the generation index.

Unlike hadronic KSVZ models, *non-hadronic* DFSZ models induce a tree-level coupling with electrons, leading to testable phenomenological effects. As we will see in chapters 2 and 3, many axion detection strategies are based on

the physical assumption that certain astrophysical environments can effectively produce axions through physical processes mediated by the axion-electron coupling. For this reason, non-hadronic axion models are particularly compelling for many axion searches in astrophysics.

Chapter 2

Selected axion astrophysical bounds

The previous chapter concluded by illustrating how axion couplings to SM fields emerge from various UV completion. In order to understand and develop possible axion detection techniques, it is necessary to investigate the environments in which these interactions can lead to efficient axion production. In this chapter, we will focus on describing various astrophysical environments as possible axion sources. Indeed, being light particles, axions can be produced in low-energy environments, such as the plasma within stars. Moreover, since they interact very weakly with SM particles, axions can escape from stellar cores without being reabsorbed.

In section 2.1, we aim to detail and comprehensively review the possible axion production processes that are at play in stellar plasmas. For each process, we will evaluate the energy loss that these astrophysical environments experience. This will allow us to assess the relative importance of each process under different plasma conditions and will be crucial for quantifying the astronomically observable effects of axion emission. Section 2.2 is dedicated to providing an overview of a selection of axion bounds and hints, discussing qualitatively how different detection strategies can constrain axion properties.

2.1 Axion production in stellar plasma

Since we aim to quantify the energy loss of a star due to axions, we are interested in describing the production of axions in systems where all other species are in thermal equilibrium, while the axion can escape. Under these con-

ditions, we can formulate a general expression for the *axion emissivity*—the energy loss rate per unit volume:

$$\varepsilon = \prod_{i=1}^{N} \int \frac{g_i \mathrm{d}^3 p_i}{2\omega_i (2\pi)^3} f_i(\omega_i) \prod_{j=1}^{N'} \int \frac{g'_j \mathrm{d}^3 p'_j}{2\omega'_j (2\pi)^3} [1 \pm f_j(\omega'_j)] \int \frac{\mathrm{d}^3 p_a}{2\omega_a (2\pi)^3} \omega_a (1 + f_{axion}) \times S \sum_{\text{spins}} |\mathcal{M}|^2 (2\pi)^4 \delta^4 \left(\sum_{j=1}^{N} p_i - \sum_{i=1}^{N'} p'_j - p_a \right), \tag{2.1}$$

where N represents the number of initial-state particles, and N' denotes the number of final-state particles excluding the axion, which has an energy ω_a and four-momentum p_a. The factor S is the symmetry factor for identical particles in the initial and final states, while g_i and g'_j are the degeneracy factor accounting for the internal degrees of freedom of each particle. The phase-space occupation numbers, f_j, follow the usual Bose-Einstein or Fermi-Dirac distributions, normalized so that the density of a given particle species is

$$n_j = \int \mathrm{d}^3 p_j \frac{g_j f_j(\omega_j)}{(2\pi)^3}. \tag{2.2}$$

For the final-state occupation factors in eq. (2.1), the plus sign applies to bosons (due to Bose enhancement), while the minus sign applies to fermions (due to Pauli blocking). The final-state occupation factor for the axions, f_{axion}, can be neglected because, being weakly interacting, axions free stream after being emitted, hence are out of thermal equilibrium. A related useful quantity to measure the impact of axion emission is the energy loss per unit mass, denoted as $\tilde{\varepsilon} = \varepsilon/\rho$ (usually expressed in $\mathrm{erg\,g^{-1}\,s^{-1}}$). Therefore, depending on the process at play in the star, the axion emissivity will be different. Before delving into a review of the various mechanisms of axion production, it is essential to evaluate the impact of the plasma's presence on eq. (2.1). At this stage, it is already evident that the plasma introduces stimulation and blocking factors, but we aim to examine in more detail what other effects are involved.

2.1.1 Plasma effects

Let us continue with a brief description of the key properties of a stellar plasma. This part is mostly based on [20]. Given a star at temperature T and density ρ, it is convenient to introduce the mass fraction parameters X_s for each species s to describe its plasma composition. Then, the number density n_s of a species

with a mass fraction X_s, atomic weight A_s and charge $Z_s e$ is given by

$$n_s = \frac{\rho}{m_u}\frac{X_s}{A_s}, \tag{2.3}$$

where $m_u = 1.66 \times 10^{-24}\,\mathrm{g} = 0.932\,\mathrm{GeV}$ is the atomic mass unit. Using these quantities, we can express the number density of electrons as

$$n_e = \sum_s Z_s n_s = \frac{\rho}{m_u}\sum_s \frac{X_s Z_s}{A_s} = \frac{\rho}{m_u \mu_e}, \tag{2.4}$$

where it was defined the quantity μ_e, the mean molecular weight per electron $\mu_e = (\sum X_s Z_s/A_s)^{-1}$. We also introduce here $Y_e \approx \mu_e^{-1}$ the mean number of electrons per baryon (which is typically $Y_e \approx \frac{1}{2}X_s$ for all the elements but the hydrogen). These quantities, together with the various coupling of axion with SM fields, are the key parameters for determining the impact of the various axion emissivities on stellar evolution.

The first effect of the presence of plasma that we want to discuss is the screening of electric charge due to the polarization of the plasma. Electrostatic fields of electrons and ions are in fact screened by the polarized medium of the star. For a weakly coupled plasma, the Gauss law in momentum space for the electric field potential Φ is modified in [20]

$$\left[k^2 + k_{\mathrm{S}}^2\right]\Phi(k) = \rho(k), \tag{2.5}$$

with k_{S} independent of k. For a point-like source, this results in the electric potential modification

$$\Phi(r) \propto r^{-1} \longrightarrow r^{-1}e^{-rk_{\mathrm{S}}}, \tag{2.6}$$

hence electric charges are screened for distances $r > k_{\mathrm{S}}^{-1}$. As a practical effect of eq. (2.6), for Coulomb processes, the photon inside the squared matrix elements $|\mathcal{M}|^2$ in eq. (2.1) is modified:

$$\frac{1}{|\mathbf{q}|^4} \longrightarrow \frac{1}{(\mathbf{q}^2 + k_{\mathrm{S}}^2)^2}, \tag{2.7}$$

where $\mathbf{q}$ is the momentum carried by the intermediate photon. It turns out that for a nondegenerate plasma, k_{S} is given by the so-called Debye-Hückle (DH) screening scale k_{D}

$$k_{\mathrm{S}}^2 = k_{\mathrm{D}}^2 = \frac{4\pi Z^2 \alpha_{\mathrm{EM}} n}{T}, \tag{2.8}$$

where n is the number density of charged particles in the plasma and T is its temperature. Taking into account the presence of electrons and different ions, the electric field screening scale reads

$$k_{\mathrm{S}}^2 = k_e^2 + k_i^2, \tag{2.9}$$

where k_e is the DH screening scale associated with the electron and k_i is due to the contribution from ions of different species in the plasma. Therefore, the total DH screening scale can be written as

$$k_{\mathrm{S}}^2 = \frac{4\pi\alpha_{\mathrm{EM}}}{T}\left(n_e + \sum_s n_s Z_s^2\right). \tag{2.10}$$

For a strongly degenerate species, eq. (2.5) implies a screening scale

$$k_{\mathrm{S}}^2 = k_{\mathrm{TF}}^2 = \frac{4Z^2\alpha_{\mathrm{EM}} m\, p_{\mathrm{F}}}{\pi}, \tag{2.11}$$

where p_{F} is the Fermi momentum, related to the particle number density by $p_{\mathrm{F}} = (3\pi^2 n_s)^{1/3}$. Typically the degenerate species are the electrons and $k_{\mathrm{TF}}^2 \ll k_{\mathrm{D}}^2$, hence in a plasma of only degenerate electrons, the main contribution to the screening scale comes from the ions and k_{TF}^2 can be safely neglected.
The screening of electric fields is associated with another plasma effect: the correlation of positions and motions of charged particles. Indeed, if a negative charge is at a certain position in the plasma, the probability of finding an electron nearby is reduced due to electrostatic repulsion, while the probability of finding a nucleus nearby increases. To quantify this effect, we need to introduce a quantity that measures the correlation between charged particles in the medium. This effect is captured by the static structure factor $S(\mathbf{q})$ [21], which modifies eq. (2.7) as follows:

$$\frac{1}{|\mathbf{q}|^4} \longrightarrow \frac{S(\mathbf{q})}{(\mathbf{q}^2 + k_{\mathrm{S}}^2)^2}. \tag{2.12}$$

In the case of DH screening (i.e. screening in a weakly coupled plasma), the structure factor reads

$$S(\mathbf{q}) = \frac{\mathbf{q}^2}{\mathbf{q}^2 + k_{\mathrm{S}}^2}, \tag{2.13}$$

finally resulting in

$$\frac{1}{|\mathbf{q}|^4} \longrightarrow \frac{1}{\mathbf{q}^2(\mathbf{q}^2 + k_S^2)^2}. \tag{2.14}$$

We conclude by highlighting that this modification of the Coulomb propagator holds only for a weakly coupled plasma, as it relies on eq. (2.5), which is based on this assumption. Indeed, the expression of the structure factor in eq. (2.13) is misleading for a strongly coupled plasma [22], [23], so it has to be evaluated numerically. In chapter 3, we will show that the typical interior of white dwarf stars is in a strongly coupled regime. Consequently, we cannot use the analytical modification in eq. (2.14) for calculating axion emissivity in that particular environment.

2.1.2 Axion emission processes in stars

Let us now examine the possible axion production processes. The axion Lagrangian written in eq. (1.37) is modified by introducing the relevant operators for understanding axion production in astrophysical environments and for experimental sensitivities. In particular, we introduce the couplings with proton and neutron fields p, n, which arise in the framework of chiral perturbation theory [24]. Therefore, we write axion effective Lagrangian as shown in [5], [25]:

$$\mathcal{L}_a = \frac{1}{2}(\partial_\mu a)^2 - \frac{1}{2}m_a^2 a^2 + \frac{\alpha_{\rm EM}}{8\pi}\frac{C_{a\gamma}}{f_a} a F_{\mu\nu}\tilde{F}^{\mu\nu} + C_{af}\frac{\partial_\mu a}{2f_a}\bar{f}\gamma^\mu\gamma_5 f, \tag{2.15}$$

where the adimensional coefficients $C_{a\gamma}$ and C_{af} have both model-dependent and model-independent contributions:

$$\begin{aligned}
C_{a\gamma} &= \frac{E}{N} - 1.92(4), \\
C_{ap} &= -0.47(3) + 0.88(3)C_u - 0.39(2)C_d - C_{a,\rm sea}, \\
C_{an} &= -0.02(3) + 0.88(3)C_d - 0.39(2)C_u - C_{a,\rm sea}, \\
C_{a,\rm sea} &= 0.038(5)C_s + 0.012(5)C_c + 0.009(2)C_b + 0.0035(4)C_t, \\
C_{ae} &= C_e + \frac{3\alpha^2}{4\pi^2}E\log\left(\frac{f_a}{m_e}\right) - 1.92(4)\log\left(\frac{\rm GeV}{m_e}\right).
\end{aligned}$$

For a better understanding of these couplings, consult [24], [25]. From this point onward, we will use the rescaled couplings:

$$g_{a\gamma\gamma} = \frac{\alpha_{\rm EM}}{2\pi}\frac{C_{a\gamma}}{f_a}, \qquad g_{aff} = C_{af}\frac{m_f}{f_a}. \tag{2.16}$$

From this effective Lagrangian, it is possible to identify the main processes through which axions are produced in astrophysical plasmas:

Process mediated by axion-photon coupling $g_{a\gamma\gamma}$

The Primakoff process, which consists of the conversion of thermal photons into axions in the electrostatic field generated by the plasma (ions or electrons) $\gamma + Ze \to a + Ze$.

Processes mediated by axion-electron coupling g_{aee}

- The Compton process, which involves the scattering of thermal photons off electrons $\gamma + e \to a + e$.
- The electron bremsstrahlung process, $e + Ze \to e + Ze + a$ (also called free-free transition) consists of the emission of an axion by an electron when it interacts with the electrostatic field generated by the plasma (ions or electrons).
- Atomic processes include axio-recombination $e + I \to I^- + a$ (also known as a free-bound transition), where a free electron is captured into an atomic shell, leading to the emission of axions. Another process is axio-deexcitation $I^* \to I + a$ (bound-bound transition), which results in monochromatic axion emission.
- The pair annihilation process $e^- + e^+ \to \gamma + a$, electron-positron pairs can annihilate to produce axions. As we shall see, astrophysical experiments aimed at testing axion properties have poor sensitivity to this process.

In the context of solar axion searches, the atomic transitions are usually grouped with bremsstrahlung and Compton processes in the so-called *ABC processes*.

Processes mediated by axion-nucleon couplings

- The nucleon bremsstrahlung process, $N + N' \to N + N' + a$, a nucleon $N = n, p$ scatters off another nucleon N', emitting an axion. The axion-nucleon couplings g_{ann}, g_{app} mediate the process.

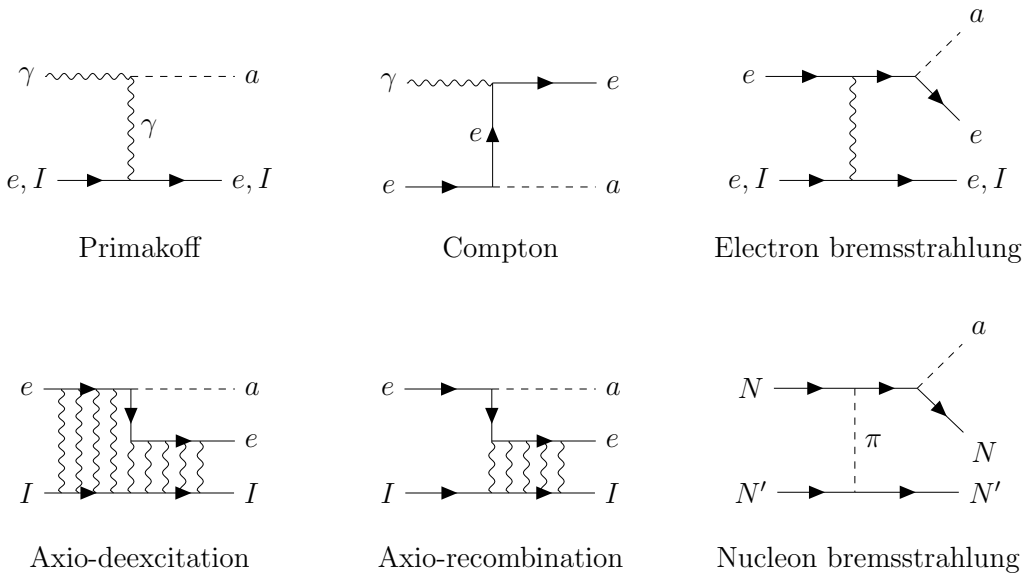

Figure 2.1: The Feynman diagrams for the most relevant axion emission processes in the context of astrophysical searches

- Nuclear reactions in stars can produce axions through axion-nucleon couplings. While we will not cover these processes in detail, it is worth mentioning that one promising observational window involves the nuclear deexcitation of ^{57}Fe, which results in a monochromatic axion emission (see outlook section in chapter 5).

Figure 2.1 summarizes the most important axion production processes in astrophysical environments that we have taken into account in this review.

We now present the axion emissivity per unit mass associated with the processes described, highlighting the dependence on the plasma characteristics introduced in section 2.1.1. By comparing these quantities for different stellar plasma, we can determine which axion emission process dominates in each astrophysical environment. Note, in this thesis the axion energy loss rate per unit volume is denoted by ε to remain consistent with the literature referenced in chapter 3. Consequently, the axion energy loss rate per unit mass is denoted by $\tilde{\varepsilon} = \varepsilon/\rho$. It should be noted that many authors, such as G. Raffelt, denote the first quantity by Q, while the second one is often denoted by ε. For all the subsequent expressions of axion emissivities, T and ρ are in units of Kelvin (K) and grams per cubic centimeter (g cm^{-3}), respectively.

Primakoff process

The first axion production mechanism described is the Primakoff process $\gamma + Ze \rightarrow a + Ze$, which is mediated by the axion-photon coupling $g_{a\gamma\gamma}$. By neglecting degeneracy effects and the plasma frequency, a semi-analytical expression for the energy-loss rate per unit mass due to axion emission can be provided [25]–[27]:

$$\tilde{\varepsilon}_{\rm P} \simeq 2.8 \times 10^{-31} F(\xi) \left(\frac{g_{a\gamma\gamma}}{\rm GeV^{-1}}\right)^2 \frac{T^7}{\rho} \quad {\rm erg\,g^{-1}\,s^{-1}}, \tag{2.17}$$

here $k_{\rm S}$ is the Debye-Hückel screening wavenumber defined in eq. (2.8), while the dimensionless coefficient $F(\xi)$ is a function of $\xi^2 \equiv (k_{\rm S}/2T)^2$ and is of order one under most stellar conditions [26]. The emission strongly depends on the temperature of the environment, as it regulates the population of the thermal photons. General cases with any degree of degeneracy are treated in [28].

Compton process

The Compton process $\gamma + e \rightarrow a + e$ is driven by the axion–electron coupling g_{aee}. In the limit of massless axions with energy $\omega_a \ll m_e$ the cross-section of the process reads [20]

$$\sigma = \frac{1}{3}\alpha \left(\frac{g_{aee}}{m_e}\right)^2 \left(\frac{\omega_a}{m_e}\right)^2. \tag{2.18}$$

In this limit is possible to neglect the recoil of the target electron, so that the incoming photon and outgoing axion will have the same energy ω. This simplifies the integrals to compute the axion emissivity in eq. (2.1), so that it can be written as [20]

$$\varepsilon_{\rm C} = R_{\rm deg} n_e \int \frac{2\, d^3k}{(2\pi)^3} \frac{\sigma\, \omega}{e^{\omega/T} - 1}, \tag{2.19}$$

where n_e is the number density of electrons and T is the temperature. The factor of 2 accounts for the internal degrees of freedom of the photon, while the coefficient $R_{\rm deg}$ accounts for degeneracy effects due to the Pauli suppression of degenerate electrons. Hence, Compton processes are significant when the electrons are non-degenerate. Performing the integral in eq. (2.19), we can compute the axion energy loss rate per unit mass due to Compton scattering in terms of the stellar plasma's properties and the axion-electron coupling g_{aee}, as reported in [20]

$$\tilde{\varepsilon}_{\rm C} \simeq 2.63 \times 10^{-22}\ R_{\rm deg} g_{aee}^2 Y_e T^6 \quad \mathrm{erg\,g^{-1}\,s^{-1}}. \tag{2.20}$$

As anticipated, when the plasma is too dense, electrons' degeneracy starts to play an important role, and the Compton emission of axions is then suppressed.

Electron bremsstrahlung process

We now proceed to describe the emissivity of axion due to axion bremsstrahlung $e + Ze \to e + Ze + a$ processes. Since this type of emission will be crucial in chapter 3, the calculation of the axion emissivity $\varepsilon_{\rm B}$ has been carried out explicitly and in detail in appendix A. Here is simply reported the result in the case of an extremely degenerate plasma, which is in accordance with the literature [29]:

$$\tilde{\varepsilon}_{\rm BD} \simeq 8.59 \times 10^{-7}\ g_{aee}^2 T^4 \sum_s \frac{Z_s^2 X_s}{A_s} F \quad \mathrm{erg\,g^{-1}\,s^{-1}}, \tag{2.21}$$

where the dimensionless factor F is a quantity of order one that accounts for medium effects, including screening of the electric field and interference between different scattering sites discussed in section 2.1.1. From this expression, it can be seen that the emission profile is essentially thermal, as $\varepsilon \propto T^4$ and does not undergo explicit suppression by density as in eqs. (2.17) and (2.20). The non degenerate limit is treated in [28], which reports

$$\begin{aligned}\tilde{\varepsilon}_{\rm BND} = 4.7 \times 10^{1} g_{aee}^2 T^{2.5} \frac{\rho}{\mu_e} \times \\ \times \sum_j \frac{X_j}{A_j} \left[Z_j^2 \left(1 - \frac{5}{8}\frac{k_s^2}{m_e T}\right) + \frac{Z_j}{\sqrt{2}} \left(1 - \frac{5}{4}\frac{k_s^2}{m_e T}\right)\right] \ \mathrm{erg\ g^{-1}\ s^{-1}}.\end{aligned} \tag{2.22}$$

Pair production

In the case of axion pair production, [30] presents the general expression for emissivity and distinguishes between different plasma conditions. However, as pointed out in [20], this process never played a significant role in setting bounds on axions form stellar evolution considerations. This is because neutrino emission via pair annihilation $e^+e^- \to \nu\bar{\nu}$ is generally more efficient, and the observable effects of energy loss for most types of conditions are primarily due to this process. The impact of axion production on stellar evolution rel-

ative to neutrinos is then expected to be most pronounced only in low-mass stars, but under these conditions, Compton-type processes are the dominant mechanism.

Nucleon bremsstrahlung process

In axion models with a sizable coupling with nucleons g_{ann} and g_{app}, the axion can be efficiently produced in some astrophysical environments through $N + N' \to N + N' + a$, with $N, N' = n, p$. This process starts to be relevant for $T > 10\,\mathrm{MeV}$ since it is suppressed by the mass of the pion mediating the interaction, and a high nucleon thermal momentum is needed for the reaction to happen. For this reason, it plays a role only in extreme environments like neutron stars and supernovae. We report here the value of the axion emissivity per unit mass due to nn scattering, for both degenerate and non-degenerate limits [25]

$$\begin{aligned} \tilde{\varepsilon}_{\mathrm{ND}} &\approx 8.0 \times 10^{-17} g_{ann}^2\, T^{3.5} \rho \ \mathrm{erg\ g^{-1}\ s^{-1}}, \\ \tilde{\varepsilon}_{\mathrm{D}} &\approx 5.7 \times 10^{-21} g_{ann}^2\, T^{6} \rho^{-2/3} \ \mathrm{erg\ g^{-1}\ s^{-1}}. \end{aligned} \tag{2.23}$$

The rates for the pp scattering have similar expressions.

Atomic processes

Axio-recombination and atomic de-excitation processes are particularly significant for ions heavier than H and He, which are generally much less abundant. However, it has been shown in [31] that axio-recombination scales more weakly with temperature compared to other g_{aee}-mediated processes, $\tilde{\varepsilon} \propto T^{1.5}$. In low-mass stars, which have lower internal temperatures, this weaker scaling can partially compensate for the low metal abundance, so that for main sequence stars with mass $M \leq 0.2\,M_\odot$ it would be the dominant axion emission process. For typical solar plasma conditions, these processes remain subdominant, contributing about 4% to the total axion flux. Axio-deexcitation contributes even less to the axion flux, exhibiting monochromatic lines in the emission spectrum.

In [32], an estimate of the ABC flux from the Sun was made by observing that axion processes can be scaled to the corresponding processes involving photons.

2.2 Axion bounds and hints

Having detailed the possible axion production processes at play in astrophysical environments, we can now explore the current axion detection strategies that utilize stars as sources. In this section, we aim to provide a brief overview of some astrophysical bounds and hints that have been placed through astronomical observations. Firstly, it is important to distinguish between two conceptually different types of axion detections in astrophysics.

Direct detection

This type of search aims to directly detect astrophysical axion fluxes which, upon entering the experimental apparatus, are converted into a detectable signal. Axion helioscope experiments [33] are paradigmatic experiments of this kind. They utilize the *inverse Primakoff process*, through which axions are converted back into photons when exposed to a macroscopic magnetic field. In this way, solar axion flux can be searched using helioscopes, which are essentially "magnetic telescopes" with an X-ray detector at the far end.

Indirect detection

Axion fluxes can also be detected indirectly when conversion into photons occurs within the natural magnetic field of the star that produced them, or within the Galactic magnetic field. In chapters 3 and 4, which form the core of this thesis, we will extensively discuss the procedure behind a novel detection strategy that exploits axion-photon conversion inside the magnetosphere of white dwarf stars.

Indirect detection also includes searching for macroscopic modifications of astrophysical observables, such as luminosity, temperature, and other measurable properties affected by the novel axion energy sink. Therefore, the key quantities for this type of search are the various axion emissivities $\tilde{\varepsilon}_{\mathrm{X}}$ and the total axion luminosity L_a.

It is important to note that an observed anomaly does not provide definitive axion detection, as there could always be alternative explanations for it, such as inaccuracies in the theoretical stellar models available. Thus, searches based on observed anomalies generally yield bounds on axion properties rather than concrete detections. Nevertheless, when inconsistencies systematically appear, they can be interpreted as hints that can guide other axion detection strategies.

2.2.1 Solar axions

Let us begin our overview by detailing the possible bounds that can be obtained from observations of the Sun. Given its relatively low density, both the Primakoff and Compton processes could play important roles. As mentioned, the key quantity for evaluating the impact of axion emission on stellar evolution is the axion emissivity or energy flux. In fig. 2.2, we compare the solar axion energy flux spectra from Primakoff emission and ABC processes, showing the dominance of the former. Thus, solar axion detection methods based on axion emissivity considerations are primarily sensitive to the Primakoff process and can place bounds on the axion-photon coupling $g_{a\gamma\gamma}$.

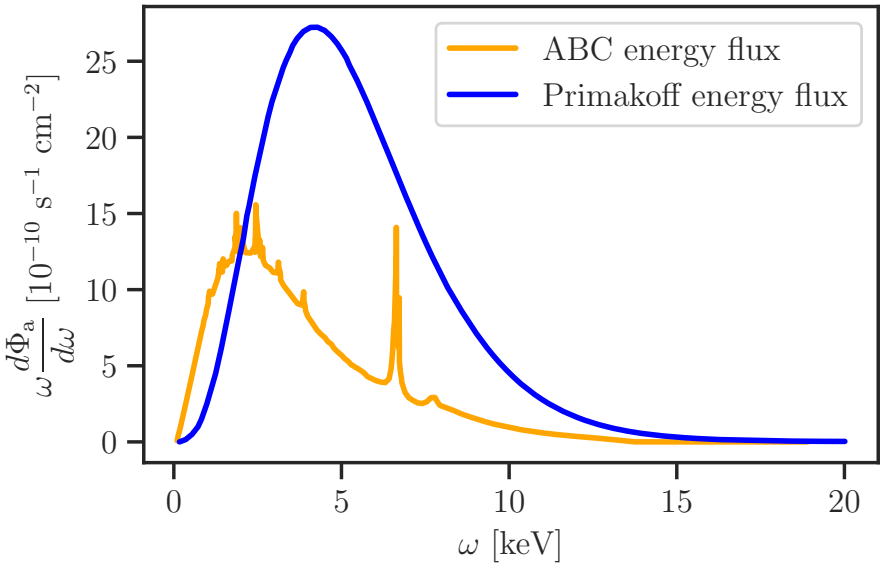

Figure 2.2: Comparison made in [5] of the solar axion energy flux spectra from the Primakoff process and the ABC processes, with $g_{a\gamma\gamma} = 10^{-10}\,\mathrm{GeV}^{-1}$ and $g_{aee} = 10^{-12}$.

Solar age bound

Since axion emission increases the consumption of nuclear energy, for the Sun to have reached its current age, the axion luminosity L_a must not exceed the solar luminosity $L_\odot$ [20]. Since the dominant production process is the Primakoff, we can integrate eq. (2.17) over a standard solar model and find [27], [34]:

$$L_\mathrm{a} = \left(\frac{g_{a\gamma\gamma}}{\mathrm{GeV}^{-1}}\right) 1.85 \times 10^{-3}\,\mathrm{L}_\odot. \tag{2.24}$$

Using the solar age requirement $L_{\rm a} \lesssim L_{\odot}$, this translates in a first rough bound for the axion-photon coupling:

$$g_{a\gamma\gamma} \lesssim 23 \times 10^{-10}\,\mathrm{GeV}^{-1}. \tag{2.25}$$

Solar Be neutrino flux bound

Another effect of a non-vanishing $L_{\rm a}$ is an increased core temperature due to higher nuclear burning necessary to produce axions. Self-consistent models indicate that the temperature increase implies an increment in the terrestrial flux of Be neutrinos [35], [36]. Current measurements of this flux [37] constrain the value of $L_{\rm a}$ and ultimately set a limit on the axion-photon coupling [27]:

$$g_{a\gamma\gamma} \lesssim 6 \times 10^{-10}\,\mathrm{GeV}^{-1}. \tag{2.26}$$

Helioscopes bounds

Given its proximity, the Sun is also used as an axion source for direct detection with axion helioscopes. These instruments require a powerful magnet that produces a strong magnetic field, inducing an axion-photon conversion probability [38]

$$\begin{aligned} p_{\mathrm{a}\to\gamma} &= \left(\frac{g_{a\gamma\gamma}B}{q}\right)^2 \sin^2\left(\frac{qL}{2}\right)\mathcal{F}(qL) \\ &\approx \left(\frac{g_{a\gamma\gamma}BL}{2}\right)^2 \qquad \text{for } |qL| \ll 1, \end{aligned} \tag{2.27}$$

for an axion with energy ω traveling a distance L in a transverse magnetic field B. Here, $q = p_a - p_\gamma$ is the axion-photon momentum difference and $\mathcal{F}(qL)$ is the form factor

$$\mathcal{F}(qL) = \frac{\sin^2(qL/2)}{(qL/2)^2}, \tag{2.28}$$

that gives $\mathcal{F} = 1$ for $|qL| \ll 1$ (*coherent conversion*), and it drops $\mathcal{F} \to 0$ for large values of $|qL|$. Assuming the ultrarelativistic limit, the momentum transfer in vacuum is $q = -m_a^2/2\omega$, meaning that up to certain values of the axion mass m_a, the coherent conversion occurs, and the helioscope sensitivity mass-independent. However, beyond a certain threshold value $m_{\rm th}$, coherence is lost, and the sensitivity of the instrument drops. A possible strategy to regain coherence is to fill the conversion region with a buffer gas that induces

an effective photon mass m_γ, which can be adjusted to match m_a [39].
We report here the results obtained by the CERN Axion Solar Telescope (CAST), a helioscope experiment that is now decommissioned. The experiment used an LHC test magnet with a magnetic field of up to $B = 9\,\mathrm{T}$ over a length of $L = 9.3\,\mathrm{m}$. For small values of the axion mass $m_a < 0.02\,\mathrm{eV}$—which ensure coherent conversion—the CAST experiment set a limit [40]:

$$g_{a\gamma\gamma} < 0.66 \times 10^{-10}\,\mathrm{GeV}^{-1} \quad \text{at } (2\sigma). \tag{2.29}$$

In fig. 2.3 we show the limit set by the CAST experiment together with the projection of IAXO, the next-generation helioscope.

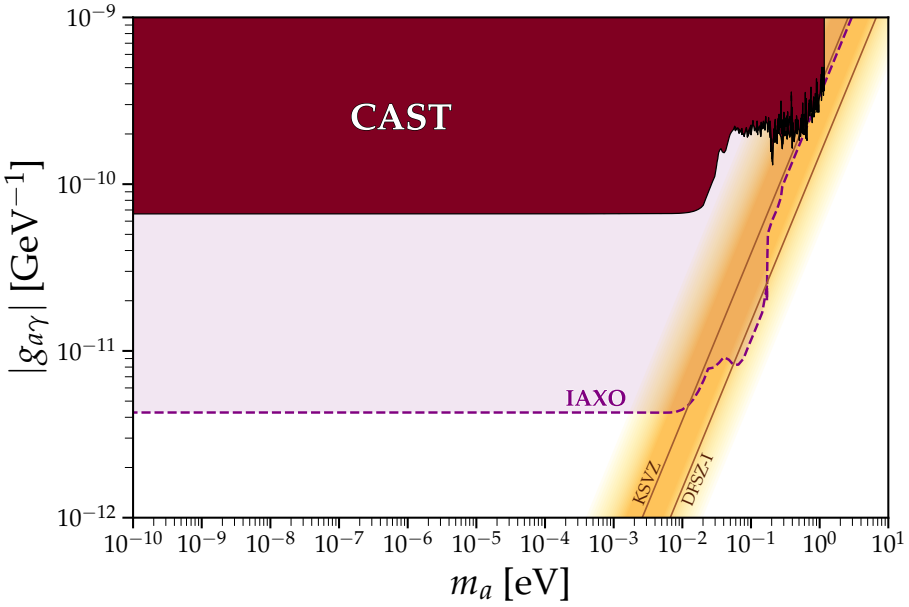

Figure 2.3: The IAXO projections compared to the limits set by the CAST experiment on the $(g_{a\gamma\gamma}, m_a)$ parameter space. Note that for $m_a > 0.02\,\mathrm{eV}$, CAST starts losing sensitivity, which was regained during a buffer gas phase, as highlighted by the "jittery" profile. This plot was obtained using code provided in [41].

In addition to its main result, CAST also investigated other axion production channels in the Sun, enabled by the axion-electron coupling g_{aee} and the axion-nucleon couplings g_{ann}, g_{app}. Indeed, for certain non-hadronic models, the ABC axion flux is comparable to the Primakoff flux, as shown in fig. 2.4. In these well-motivated cases, helioscopes provide limits on the product $g_{aee} \times g_{a\gamma\gamma}$, which is particularly relevant to this thesis. As we will see in chapter 3, non-hadronic axion models that predict tree-level coupling with electrons open up new observational windows for testing axion properties and

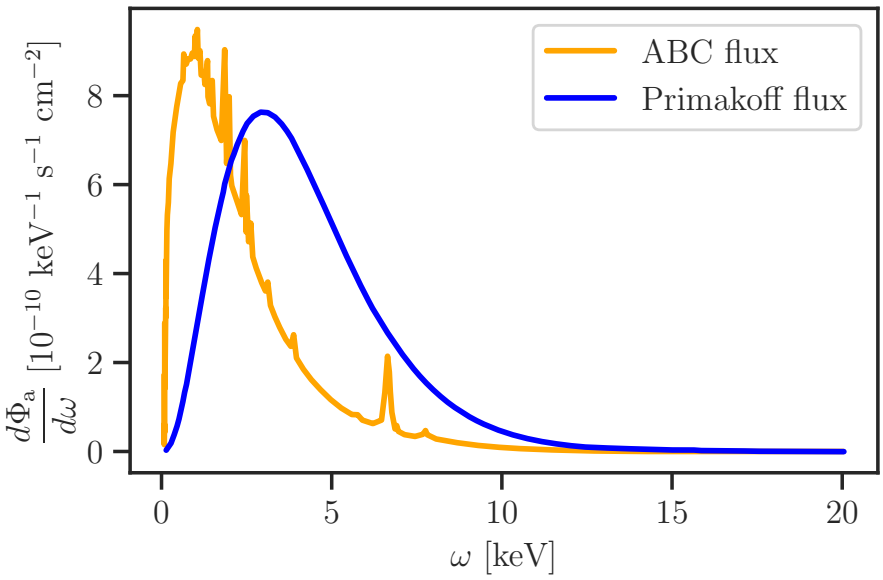

Figure 2.4: Comparison made in [5] of the solar axion flux spectra from the Primakoff process and the ABC processes, using the same coupling values as in fig. 2.2: $g_{a\gamma\gamma} = 10^{-10}\,\mathrm{GeV}^{-1}$ and $g_{aee} = 10^{-12}$.

potential axion discovery.

Within the framework of helioscope experiments, we present the results of an analysis of CAST data [42], which considers g_{aee} as responsible for the production of solar axions through ABC reactions. This analysis yielded the following constraint for low masses $m_a \lesssim 10\,\mathrm{meV}$:

$$g_{aee} \times g_{a\gamma\gamma} < 8.1 \times 10^{-23}\,\mathrm{GeV}^{-1} \quad \text{at } (2\sigma). \tag{2.30}$$

In fig. 2.5 it is reported the parameter space $(g_{aee} \times g_{a\gamma\gamma}, m_a)$ with the result of such analysis.

2.2.2 Globular cluster stars

Next, we explore the bounds on axion couplings that arise from observations of globular cluster (GC) stars. Globular clusters are stable and gravitationally bound systems containing tens of thousands to millions of stars. They are of great interest because their constituent stars formed at approximately the same time and location, with very similar initial conditions. Consequently, their observation allows for the study of stellar evolution, particularly through color-magnitude diagrams (CMD). In these diagrams, surface brightness is plotted against surface temperature, and stars are located in distinctive posi-

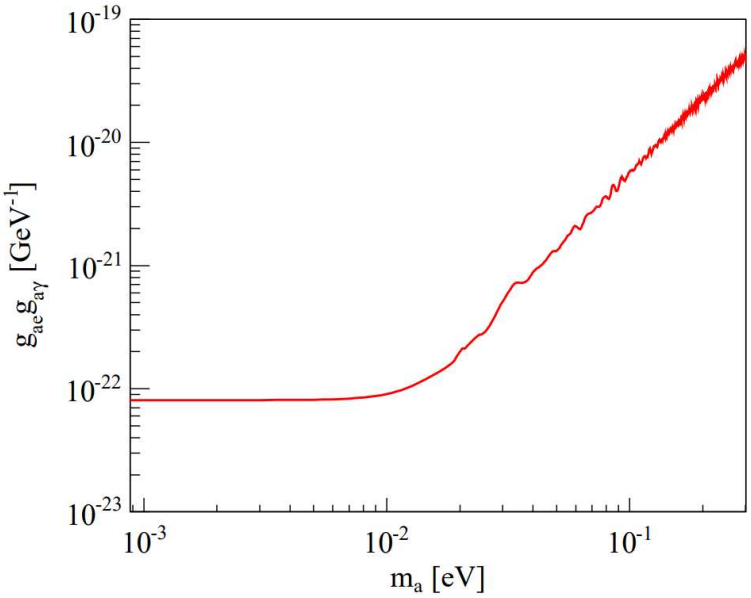

Figure 2.5: CAST constraints on $g_{aee} \times g_{a\gamma\gamma}$ as a function of m_a, obtained under the model dependent assumption that the solar emission is dominated by the ABC reactions mediated by the electron coupling g_{aee}. Plot taken from [42].

tions that represent particular evolutionary stages. We are interested in GCs because the additional axion energy sink affects stellar evolution, leading to observable changes in specific regions of their CMDs. By comparing these expected deviations with observational data, we can set stringent bounds on axion couplings.

Red giant branch tip bound

During the main sequence (MS) phase, stars spend the majority of their lifetimes burning hydrogen. As the hydrogen in the core depletes, they move off the main sequence and, after a transient phase on the sub-giant branch, stars enter the red giant branch (RGB). At this stage, the star is characterized by an inert helium core surrounded by a burning hydrogen envelope. As the envelope expands, the helium core becomes more massive and increasingly contracts, causing its temperature and pressure to rise and developing electron degeneracy. Eventually, the helium in the core ignites in a process known as the *helium flash*, marking the so-called *RGB tip* in the CMD. This occurs when the RGB star has reached approximately $\rho \sim 10^6\,\mathrm{g/cm^3}$ and $T \sim 10^8\,\mathrm{K}$.

The CMD observable used to constrain axions is the luminosity of the RGB tip, which is essentially determined by the combined effects of energy

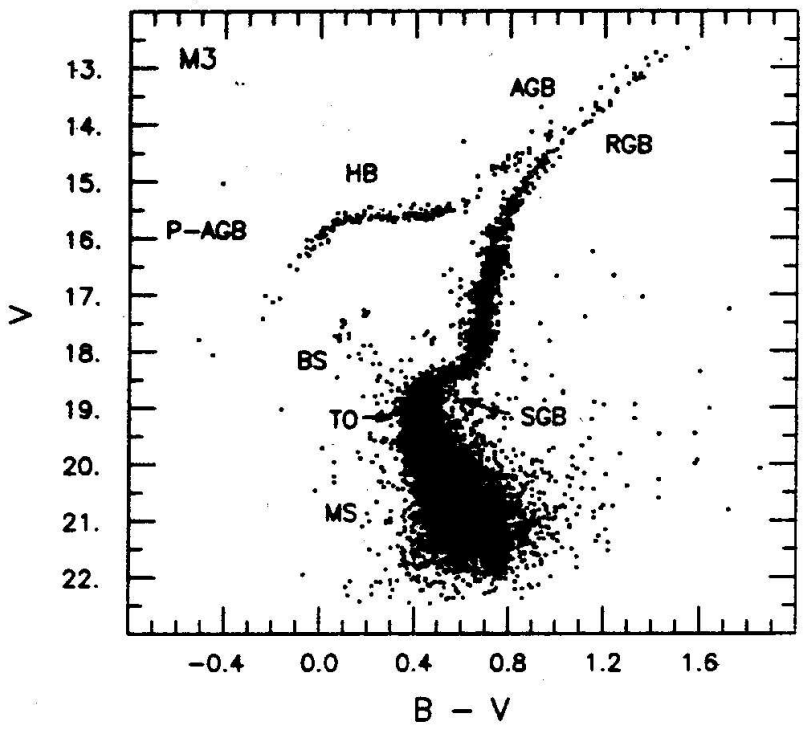

Figure 2.6: Color-magnitude diagram of the M3 globular cluster taken from [43]. This diagram illustrates the distribution of stars based on their brightness and surface temperature, showcasing the various evolutionary stages of the stars within the cluster.

sources, and energy sinks like plasma neutrinos $\gamma \to \nu\bar{\nu}$ [44] and axion emission. Indeed, additional energy losses lead to extra cooling, causing the helium core to grow more before it can ignite. The overall result is a shorter RGB phase, characterized by an RGB tip with higher luminosity [27]. Given the high density and temperature, the dominant mechanism of axion production is axion-bremsstrahlung eq. (2.21), making this CMD observable sensitive to the axion-electron coupling g_{aee}. For a more detailed overview of the different treatments of this RGB tip constraint, refer to [27]. Here, we limit ourselves to reporting the value from a recent analysis [45] that considers observational data from 22 GCs. The resulting bound is:

$$g_{aee} < 1.48 \times 10^{-13} \quad \text{at } (2\sigma) \ . \tag{2.31}$$

R parameter bound

After the helium flash, the core expands, and the star enters the horizontal branch (HB) phase, a stage in stellar evolution where helium fusion occurs in a non-degenerate core. Similarly to the previous case, this evolutionary phase is associated with a CMD observable that allows us to constrain axion properties. Since GC stars are approximately coeval, the number of stars observed in a given portion of the associated CMD is proportional to the time spent by a star in that region. As previously mentioned, axion bremsstrahlung speeds up the RGB phase. Consequently, the number of RGB stars $N_{\rm RGB}$ is affected by the axion-electron coupling g_{aee}. Similarly, axion emission processes shorten the HB phase. Because the helium core expands during this phase, HB stars are less dense compared to RGB stars, having a core density of $\rho \sim 10^4\,\mathrm{g/cm^3}$ and a temperature of $T \sim 10^8\,\mathrm{K}$. For this reason, in HB stars axions are efficiently produced through the Primakoff and Compton processes, and $N_{\rm HB}$ is modified by both $g_{a\gamma\gamma}$ and g_{aee}. An efficient way to quantify the CMD observable impact of the axion couplings g_{aee} and $g_{a\gamma\gamma}$ is the R-parameter:

$$R = \frac{N_{\rm HB}}{N_{\rm RGB}}. \tag{2.32}$$

Typically, an axion model assumption is made neglecting the effects of the axion-electron coupling g_{aee}, so that eq. (2.32) is used to derive bounds on the axion-photon coupling $g_{a\gamma\gamma}$. In [46], [47], data from 39 GCs—which yield an observed value $R_{\rm obs} = 1.39 \pm 0.03$—are compared with the theoretical parametrization:

$$R_{\rm th}(g_{a\gamma\gamma}, Y) = 6.26Y - 0.41\left(\frac{g_{a\gamma\gamma}}{10^{-10}\,\mathrm{GeV}^{-1}}\right)^2 - 0.12, \tag{2.33}$$

where Y is the helium abundance of the GB. Measurements of GCs' helium abundances result in the bound:

$$g_{a\gamma\gamma} < 0.65 \times 10^{-10} \quad \text{at } (2\sigma). \tag{2.34}$$

Here we also present a theoretical parametrization of eq. (2.32) provided in [5], [25] that includes the effects of axion interactions with electrons:

$$R_{\rm th}(g_{a\gamma\gamma}, g_{aee}, Y) = R_0(Y) - F_{a\gamma\gamma}(g_{a\gamma\gamma}) - F_{aee}(g_{aee}), \tag{2.35}$$

where $R_0(Y)$ is a function of the helium abundance Y in the GC, and $F_{a\gamma\gamma}$ and F_{aee} are positive-defined functions of the axion couplings. Reference [48] provides approximate analytical expressions for these functions.

2.2.3 White dwarf bounds and hints

White dwarfs (WDs) represent the final stage of the evolution of low-mass stars ($M \leq 8M_\odot$). After exhausting their nuclear fuel and losing most of their envelopes, they remain as carbon-oxygen stars with masses in the range of $0.5 - 1.4M_\odot$. With no nuclear reactions to counteract gravitational collapse, the star shrinks until electron degeneracy pressure stops the process. As a result, WDs are approximately the size of Earth, resulting in a high density of about $10^6\,\mathrm{g\,cm^{-3}}$. The core temperature, which varies with the age of the star, typically ranges from 10^6 to $10^7\,\mathrm{K}$. Because of this, the Primakoff and Compton processes are suppressed in the core of WDs, making axion bremsstrahlung the most relevant axion production mechanism [29]. On top of that, the high degree of electron degeneracy further suppresses electron-electron interactions, leaving electron-ion axion bremsstrahlung, mediated by the axion-electron coupling g_{aee}, as the dominant process. The evolution of WDs involves contraction and cooling, and adding a novel energy sink would result in an accelerated cooling process. In the following, we will discuss two observables to test the effects of an additional cooling agent, thereby placing bounds on axion properties.

White dwarf luminosity function

The first observable is the White Dwarf Luminosity Function (WDLF), which describes the distribution of the number of white dwarfs in a given stellar population as a function of their luminosity. As this is determined by the rates at which these stars form and cool, an efficient axion production can significantly alter the shape of the WDLF. Notably, the slope is related to the cooling speed of white dwarfs, while the amplitude characterizes the cooling time and the white dwarf birthrate. Simulated WDLFs that incorporate axion cooling effects can be compared to observed WDLFs to constrain g_{aee}. Such computations of the Milky Way galactic disk WDLFs are performed in [49], and subsequently compared with WDLFs obtained using data from both the SDSS [50] and SuperCOSMOS sky surveys [51]. The result of this analysis places the constraint [49]

$$g_{aee} < 2.1 \times 10^{-13} \quad \text{at } (2\sigma). \tag{2.36}$$

To add to this, studies on the WDLF of the Milky Way suggest a systematic excessive cooling compared to what is expected from standard stellar evolution theory [52]. As a result, it is possible to derive a *cooling hint* for the axion-electron coupling, i.e., the value of g_{aee} that best explains the observed anomaly, yielding $g_{aee} \simeq (1.4 \pm 0.3) \times 10^{-13}$ at (1σ) [25].

White dwarf variables

The second important astrophysical observable for white dwarfs is the period change of white dwarf variables (WDVs), a set of white dwarfs whose luminosity pulsates periodically. For these stars, the cooling rate is observationally reflected by a variation in the pulsation period P. In particular, the rate of period change, $\dot{P}/P$, is connected to the rate of change of the core temperature, $\dot{T}/T$—see [53] for a complete overview on the topic. The presence of an extra cooling channel, like the one due to axion production, would accelerate the cooling, resulting in an anomalous larger rate of period change. Indeed, by observing the period variation of several WDs over a few decades, it has been possible to systematically measure a larger variation than theoretically predicted [53]. Assuming this is entirely due to axion emission via bremsstrahlung, eq. (2.21), it is possible to derive bounds and hints for g_{aee}. In particular, we report the results obtained from the analysis of WDV

G117-B15A observations [54]

$$g_{aee} < 6.7 \times 10^{-13} \quad \text{at } (2\sigma). \tag{2.37}$$

Chapter 3

Axion astrophysical bound from white dwarfs X-ray observations

In the previous chapter, we introduced various astrophysical axion detection techniques and discussed some of the bounds obtainable on axion couplings with SM particles. Particularly, we introduced helioscope experiments like CAST and IAXO, which exploit the conversion of an axion flux in a magnetic field to obtain a detectable signal. Now, we introduce another axion detection strategy that similarly utilizes the inverse Primakoff effect to convert an axion flux, produced in the interior of a star, directly into photons within the star's natural magnetic field. This has the significant advantage of achieving a much higher conversion probability $p_{a\to\gamma}$ compared to what can be obtained in a laboratory setting. In fact, from eq. (2.27), it can be inferred that a major practical limit on the conversion probability on Earth is due to our capacity to fill relatively small regions of space $L \sim 10\,\mathrm{m}$ with relatively weak magnetic fields $B \lesssim 10\,\mathrm{T}$ compared to those developed in the magnetosphere of certain stars. In this chapter, we will detail an analysis pipeline for X-ray data from white dwarf observations to constrain axion properties based on this novel phenomenology.. In section 3.1, we will explain why WDs are an excellent candidate for this type of search, and we will go on to characterize in detail the emission of axions from the WD plasma and the subsequent conversion into photons in the external magnetic field. Section 3.2 deals with the modeling of the response function of a typical X-ray telescope. Section 3.3 is devoted to laying out the general statistical analysis principles for this type of experiment.

3.1 White dwarfs as source for axion detection

Among the various types of astrophysical objects, white dwarfs stand out as excellent targets for detecting axion-induced photon flux. The first reason is that, for certain axion models, these stars can be prolific sources of axions. As discussed in section 2.2.3, axions can be produced in the plasma of white dwarfs through electron-ion axion bremsstrahlung, mediated by the axion-electron coupling g_{aee}. Non-hadronic axion models that predict a tree-level coupling to electrons (like DFSZ models) can thus lead to efficient production of axions in the WD plasma, making white dwarfs a well-justified candidate for axion searches.

The second reason is that certain white dwarfs can develop extremely intense magnetic fields, which can convert a significant fraction of emitted axions into detectable photons. During its evolution into a white dwarf, the star undergoes significant shrinkage. Assuming the conservation of magnetic flux during its evolution from the main sequence to the compact star phase [55], this results in certain white dwarfs having very intense magnetic fields. White dwarfs can have magnetic fields ranging from 10^3 to 10^9 G, with over 600 white dwarfs identified as having strong magnetic fields between 2 and 1000 MG [56] (to be compared with the artificial magnetic fields of helioscopes $B < 0.1\,\mathrm{MG}$).

Another factor that makes white dwarfs particularly interesting for indirect axion flux detection is that, under the typical WD core temperature and density conditions, the emission spectrum of axion-induced photons peaks in the X-ray band. Since no other astrophysical processes are expected to produce hard X-ray photons (>0.5 keV) from isolated white dwarf stars [57], [58], they provide a clean environment for this novel type of observation. In table 3.1, we present the typical characteristics of white dwarfs:

Table 3.1: Typical values for properties and conditions of white dwarf stars

Quantity	Value
Mass	$0.5 - 1.4\,M_\odot$
Radius	$(0.4 - 2) \times 10^{-2}\,R_\odot$
Luminosity	$< 10^{-4}\,L_\odot$
Surface Temperature	$< (0.8 - 4.0) \times 10^4\,\mathrm{K}$
Core Temperature	$\sim 10^7\,\mathrm{K}$
Density	$1.8 \times 10^6\,\mathrm{g\,cm^{-3}}$
Composition	C and O
Surface B-field	$\sim (10^3 - 10^9)\,\mathrm{G}$

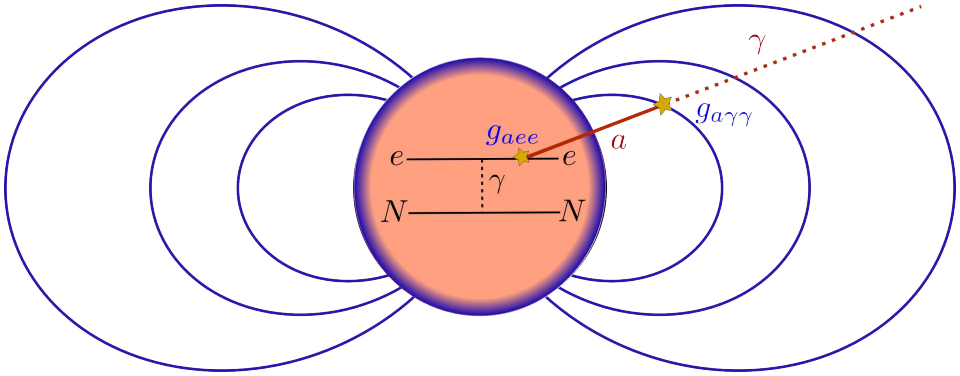

Figure 3.1: The schematic phenomenology behind white dwarf X-ray emission (adapted from [59]): g_{aee} enables axion production in the WD interior through axion-bremsstrahlung, the axion is subsequently converted into X-ray photons by the external magnetic field thanks to the $g_{a\gamma\gamma}$ coupling.

In fig. 3.1 we schematically summarize the phenomenology that motivates X-ray observations of white dwarfs to detect axion emission. Hence, the general expression for the axion-induced photon flux on Earth reads

$$\frac{dF_{\mathrm{a}\gamma}}{d\omega}(\omega) = \frac{dL_{\mathrm{a}}}{d\omega}(\omega) \times p_{\mathrm{a}\to\gamma}(\omega) \times \frac{1}{4\pi d_{\mathrm{WD}}}, \tag{3.1}$$

where d_{WD} is the distance between the WD and the Earth. Note that the axion luminosity spectrum $dL_{\mathrm{a}}/d\omega$ depends on g_{aee}, while the probability conversion is mediated by $g_{a\gamma\gamma}$ through the inverse Primakoff. This is why the spectrum in eq. (3.1) will depend on the product $g_{aee} \times g_{a\gamma\gamma}$ and, consequently, this type of axion detection experiment aims to test such a quantity. The goal of this section is to model the axion-induced photon flux described in eq. (3.1), thereby developing the first part of our analysis pipeline.

3.1.1 Axion emission from white dwarfs

Let us start by computing the axion luminosity of a generic white dwarf. In section 2.1 we have seen that the dominant axion production process in these stars is the axion bremsstrahlung from electron-ion scattering in eq. (2.21). The related axion emissivity spectrum is computed in appendix A in the limit of a vanishing axion mass, yielding the expression:

$$\frac{d\varepsilon_a}{d\omega} = \frac{\alpha_{\mathrm{EM}}^2 g_{aee}^2}{4\pi^3 m_e^2} \frac{\omega^3}{e^{\omega/T} - 1} \sum_s \frac{Z_s^2 X_s \rho}{A_s m_u} F. \tag{3.2}$$

This includes a sum over the species s of nuclei present in the plasma, and the dimensionless quantity F accounts for the medium effects described in section 2.1.1, i.e., charge screening and correlation between ion positions, and is typically of order one. When the mass of the axion becomes comparable to the temperature of the environment in which it is produced ($m_a \sim T$), the expression in eq. (3.2) is no longer valid, as the axion production would be Boltzmann suppressed. To obtain the axion luminosity spectrum of the WD, it is necessary to integrate eq. (3.2) over the entire volume of the white dwarf under study:

$$\frac{dL_{\rm a}}{d\omega}(\omega) = \int dV \frac{d\varepsilon_a}{d\omega}, \tag{3.3}$$

In particular, we assume that the system enjoys spherical symmetry so that the axion luminosity spectrum reads:

$$\frac{dL_{\rm a}}{d\omega}(\omega) = 4\pi \int_0^{\rm R_{WD}} dr\, r^2 \frac{d\varepsilon_a}{d\omega}(r), \tag{3.4}$$

where $\rm R_{WD}$ is the WD radius. Therefore, the quantities needed to compute the spectrum in eq. (3.4) are the various profiles $T(r)$, $\rho(r)$, $X_s(r)$, and $F(r)$. A further simplification is to consider the core temperature constant $T(r) = T$ throughout the star volume, given the high thermal conductivity of the degenerate plasma in white dwarfs [60]. From the expression in eq. (3.4), we can already understand the shape of the spectrum. It is, in fact, a black body-type spectrum, $\frac{dL_{\rm a}}{d\omega} \propto \frac{\omega^3}{e^{\omega/T}-1}$. The Wien displacement law tells us that the emission peak occurs at $\omega \approx 2.82\,T$, which, for typical white dwarf core temperatures of $T \sim 10^7\,\rm K$, corresponds to emission in the keV range, thus justifying observation in the X-ray spectrum.

In order to compute the axion luminosity spectrum, it is essential to have a model for the interior of the star that provides the density ρ and composition X_s profiles of the species s present in the plasma. Typically, these quantities are obtained through numerical simulations of stellar evolution, ensuring that the obtained astrophysical properties match the actual observations of the white dwarf under consideration. On the other hand, the calculation of the medium factor profile $F(r)$ is less straightforward.

3.1.2 Medium effects on axion emission

In appendix A we have derived the formal expression for the medium factor F which we recall here

$$F = \int \frac{d\Omega_2}{4\pi} \int \frac{d\Omega_a}{4\pi} \frac{(1-\beta_F^2)[2(1-c_{12}) - (c_{1a}-c_{2a})^2]}{(1-c_{1a}\beta_F)(1-c_{2a}\beta_F)(1-c_{12})(1-c_{12}+\kappa_s)}, \tag{3.5}$$

where p_F is the electron Fermi energy, β_F is the correspondent electron velocity, and $\kappa_s = k_S/2p_F$. This expression was obtained assuming a weakly coupled plasma and this is not the case for the typical conditions of a WD plasma. In order to show this, we first define the plasma coupling parameter

$$\tilde{\Gamma} = \frac{E_C}{kT}, \tag{3.6}$$

where E_C is the Coulomb energy per ion $E_C = Z_s^2 e^2/4\pi a_s = Z_s \alpha_{EM}/a_s$ with a_s the ion-sphere radius defined by $n_s^{-1} = 4\pi a_s^3/3$, where n_s is the ion density. The ratio in eq. (3.6) quantifies the strength of electrostatic interaction between particles in the plasma relative to their thermal energy. For consistency with the cited literature, a rescaled quantity $\Gamma = 4\pi\tilde{\Gamma}$ will be used. Numerically it is found that

$$\Gamma = 2.275 \times \; Z^2 A^{-1/3} \left(\frac{T}{10^7 \mathrm{K}}\right)^{-1} \left(\frac{\rho}{10^6 \,\mathrm{g\,cm^{-3}}}\right)^{1/3}. \tag{3.7}$$

This quantity effectively measures how strongly the plasma particles interact with each other. Depending on the magnitude of Γ, plasma properties change, $\Gamma < 1$ corresponds to a weakly coupled plasma, $\Gamma \gg 1$ to a strongly coupled plasma. Let us take as an example a white dwarf composed solely of carbon-12 (^{12}C), with a typical density of $\rho = 1.8 \times 10^6 \,\mathrm{g\,cm^{-3}}$ and consider a range of temperatures $T = 10^6 - 10^7$K. Utilizing the expression in eq. (3.7), we obtain a range of values for the coupling parameter $\Gamma \simeq 360 - 35$, hence the plasma of a typical white dwarf is always strongly coupled and F has to be computed numerically. The only numerical parametrization available in the literature is given in [61], [62], which provides fitting functions for the F medium factors for plasmas consisting of a single element. This requires calculating distinct F_s values for each species s present in the white dwarf and then summing them up.We note that this approach to evaluating medium effects may not be entirely adequate. A unified procedure that accounts for the presence of multiple elements in the WD plasma would be necessary. The actual formula

used for the computation of a white dwarf axion emissivity spectrum reads

$$\frac{d\varepsilon_a}{d\omega} = \frac{\alpha_{\rm EM}^2 g_{aee}^2}{4\pi^3 m_e^2} \frac{\omega^3}{e^{\omega/T} - 1} \sum_s \frac{Z_s^2 X_s F_s}{A_s m_u} \rho. \tag{3.8}$$

For the calculation of the various profiles $F_s(r)$, it is necessary to consider another effect due to the size of Γ. When $\Gamma > 178$, the plasma undergoes a phase transition, and the ions arrange themselves in a body-centered cubic lattice [63], [64], a condition that suppresses axion emission. In [61], [62] are provided two separate numerical recipes for F_s depending on the state of the plasma.

3.1.3 Axion-photon conversion

We now turn to the framework used to compute the axion-photon conversion probability in the magnetosphere of a white dwarf. The formula in eq. (2.27) only applies to regions with a constant magnetic field, and thus it does not apply to the natural field of a white dwarf, which varies along the direction of axion propagation. Nevertheless, the starting point for both derivations is always the Lagrangian of axion electrodynamics [65], [66]. Here we make the approximation in which all the emitted axions follow a radial trajectory originating from the center of the white dwarf. In this scenario, and under the assumption that the magnetic field changes over a scale much larger than the wavelength of both the axion and the photon, the equations of motion for the axion and photon fields simplify to a system of first-order differential equations. Using the Weyl gauge $A^0 = A_0 = 0$ and considering trajectories in which the angle with respect to the magnetic field does not vary one can write the mixing equations as [65]

$$\left[i\partial_r + \omega + \begin{pmatrix} \Delta_\parallel & \Delta_B \\ \Delta_B & \Delta_a \end{pmatrix} \right] \begin{pmatrix} A_\parallel \\ a \end{pmatrix} = 0, \tag{3.9}$$

where ω is the axion/photon energy and r is the radial trajectory coordinate. The term $A_\parallel(r)$ represents the vector potential component perpendicular to the propagation direction and along which the external magnetic field has its full projection, while $a(r)$ denotes the axion field. The requirement to consider only trajectories with a constant angle relative to the magnetic field will soon be justified by a specific choice of magnetic field geometry. This simplification allows us to consider the mixing of the axion field only with one component

of the vector potential.

Calling $B(r)$ the magnetic field strength at distance r from WD center, and Θ the constant angle between the radial direction and the magnetic field, the off-diagonal term that induces the mixing reads

$$\Delta_B(r) = \frac{g_{a\gamma\gamma}}{2} B(r) \sin\Theta. \tag{3.10}$$

Hence, the coupling $g_{a\gamma\gamma}$ governs the mixing, so we expect the final photon flux to depend on this quantity. Also, note that a magnetic field $B_T = B\sin\Theta$ transverse to the direction of motion of the axion/photon is necessary to induce the mixing. The axion diagonal term reads

$$\Delta_a = -\frac{m_a^2}{2\omega}, \tag{3.11}$$

and accounts for the slight momentum differences in the vacuum between axion and photon states. Similarly to what we have seen for the conversion in helioscopes, the transition is maximized for small axion masses m_a, i.e. when we have a coherent superposition of the two particles [67]. The other diagonal term is due to QED vacuum birefringence effects, which lead to [65]

$$\Delta_\parallel(r) = \frac{7}{2}\,\omega\,\xi(r)\sin^2\Theta, \tag{3.12}$$

with $\xi(r) = (\alpha_{\rm EM}/45\pi)[B(r)/B_{crit}]^2$ and $B_{crit} = m_e^2/e \approx 4.41\times10^{13}\,\mathrm{G}$. This term is due to a refractive index for $A_\parallel$ greater than unity, which is induced by the presence of a magnetic field. The magnetic field B of the white dwarf thus has two opposite effects: it facilitates mixing through Δ_B, but makes the photon and axion less degenerate through $\Delta_\parallel$, making oscillation more difficult. However, this latter effect is suppressed by the strong $B_{\rm crit}$ and therefore it starts to play a role only for strong magnetic fields. One can check that, for a choice of $g_{a\gamma\gamma} = 10^{-11}\,\mathrm{GeV}^{-1}$ — i.e. the order of magnitude of the current bound for low-mass axions — and $\omega = 10\,\mathrm{keV}$, the ratio $\Delta_\parallel/\Delta_B$ becomes bigger than unity for values $B_T \gtrsim 100\,\mathrm{MG}$.

The conversion probability of an axion into a photon, $p_{\mathrm{a}\to\gamma}$, is calculated by solving eq. (3.9) and comparing the squared magnitude of an initially pure axion state with the asymptotic solution for the electromagnetic vector potential. If the external magnetic field B were constant along a trajectory of length L, solving eq. (3.9) would yield the result in eq. (2.27). In appendix B we show that, in the weak mixing limit, one can use the formalism of time-perturbation

theory to obtain a perturbative expansion of the amplitude of the transition. At the leading order (LO), the corresponding conversion probability is given by

$$p_{\mathrm{a}\to\gamma} = \left| \int_{\mathrm{R_{WD}}}^{\infty} dr' \Delta_B(r') e^{i\Delta_a r' - i\int_{R_{\mathrm{WD}}}^{r'} dr'' \Delta_{\parallel}(r'')} \right|^2, \tag{3.13}$$

where the integral starts at the white dwarf surface since we are assuming that X-ray photons produced inside the star are reabsorbed and cannot escape. The conversion probability clearly depends on the geometry assumed for the magnetic field of the WD. In a first approximation, the magnetic field of a star can be approximated to a pure magnetic dipole. Under this assumption, the magnetic field of the WD expressed in spherical coordinates (r, θ, ϕ) reads

$$\mathbf{B}(r,\theta) = \frac{|\mathbf{m}|}{4\pi r^3}\Big[3\hat{\mathbf{r}}(\hat{\mathbf{m}}\cdot\hat{\mathbf{r}}) - \hat{\mathbf{m}}\Big], \tag{3.14}$$

where $\mathbf{m}$ is the magnetic dipole moment, which verifies $|\mathbf{m}|/4\pi = B_0 \mathrm{R}_{\mathrm{WD}}^3/2$ with B_0 is the value of the field at the surface and directed along the magnetic axis. Using this magnetic field modeling, it follows that radial trajectories have a constant angle with respect to the magnetic field $\mathbf{B}$. Using a magnetic dipole the entries of the mixing matrix in eqs. (3.10) to (3.12) read

$$\Delta_B(r,\theta) = \frac{1}{2} g_{a\gamma\gamma} B_T(r,\theta), \tag{3.15}$$

$$\Delta_a(\omega) = -\frac{m_a^2}{2\omega}, \tag{3.16}$$

$$\Delta_{\parallel}(r,\theta,\omega) = \frac{7}{2}\,\omega\,\frac{\alpha}{45\pi}\Big(\frac{B_T(r,\theta)}{B_{crit}}\Big)^2. \tag{3.17}$$

Since the coordinate θ corresponds to the angle between the trajectory and the magnetic pole $\hat{\mathbf{m}}\cdot\hat{\mathbf{r}} = \cos\theta$, the transverse magnetic field $B_T = \mathbf{B}\cdot\hat{\boldsymbol{\theta}}$ reads

$$B_T(r,\theta) = \frac{B_0}{2}\Big(\frac{R_{WD}}{r}\Big)^3 \sin\theta. \tag{3.18}$$

Therefore the conversion probability $p_{\mathrm{a}\to\gamma}$ depends on the axion-photon coupling $g_{a\gamma\gamma}$, the axion mass m_a, its energy ω, the field strength B_0, the viewing angle θ, and the white dwarf radius $\mathrm{R_{WD}}$.

As reported in [59], for a dipole magnetic field and in the limit of massless

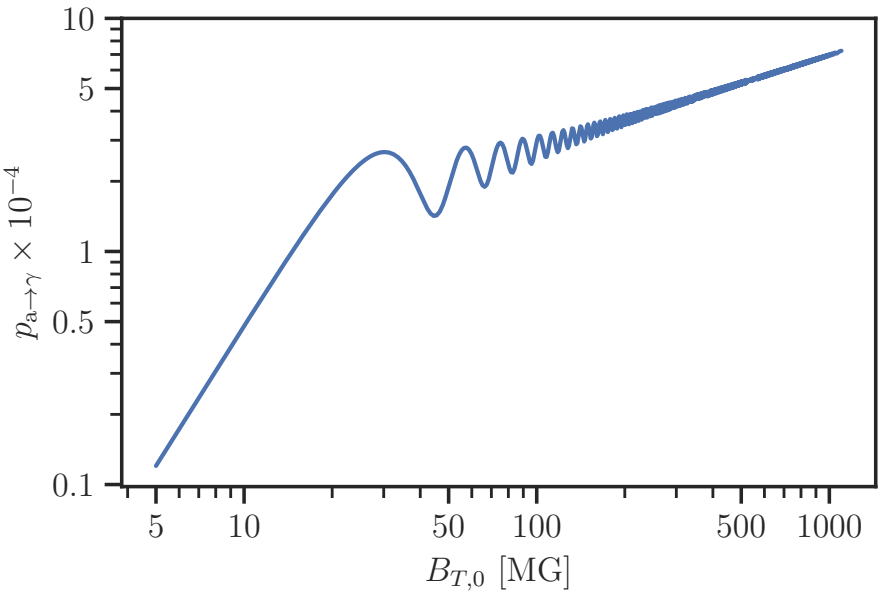

Figure 3.2: The RE J0317-853 conversion probability $p_{a\to\gamma}$ for different values of $B_{T,0}$. For this plot we used $g_{a\gamma\gamma} = 10^{-11}\,\mathrm{GeV}^{-1}$, $\omega = 10\,\mathrm{keV}$ and $\mathrm{R_{WD}} = 0.004 R_\odot$, a typical WD radius

axion $m_a \to 0$, the conversion probability can be expressed analytically as

$$p_{a\to\gamma} = \frac{(\Delta_{B,0}\mathrm{R_{WD}})^2}{(\Delta_{\parallel,0}\mathrm{R_{WD}})^{\frac{4}{5}}} \left| \frac{\Gamma(\frac{2}{5}) - \Gamma(\frac{2}{5}, -\frac{i}{5}\Delta_{\parallel,0}\mathrm{R_{WD}})}{5^{\frac{3}{5}}} \right|^2 , \tag{3.19}$$

where $\Gamma(z)$ is the gamma function, $\Gamma(a,z)$ is the upper incomplete gamma function, $\Delta_{B,0}$ and $\Delta_{\parallel,0}$ are the two functions in eqs. (3.15) and (3.17) taken for the transverse magnetic field $B_{T,0}$ evaluated at the surface $r = \mathrm{R_{WD}}$. Figure 3.2 shows the plot of eq. (3.19) as a function of $B_{T,0}$. As previously mentioned, when the magnetic field is not too intense, the contribution of $\Delta_{B,0}$ is dominant in eq. (3.19), and $p_{a\to\gamma}$ increases significantly with $B_{T,0}$. However, as $B_{T,0}$ increases, the contribution due to $\Delta_{\parallel,0}$ becomes more evident, slowing the growth of the conversion probability.

We can now ask what exactly the massless limit assumed to derive this analytical expression means. To evaluate the impact of the axion mass m_a on the integral in eq. (3.13), we define the *critical mass index* as the ratio between the quantities in the exponent

$$I(r, m_a) = \left| \frac{\Delta_a(m_a) r}{\int_{R_{\mathrm{WD}}}^{r} dr' \Delta_\parallel(r')} \right| . \tag{3.20}$$

Conservatively, we have chosen typical values $B_{T,0} = 100\,\mathrm{MG}$ and $\omega = 1\,\mathrm{keV}$ for the magnetic field of the WD and the energy of the axion, respectively. When this parametric expression reaches the order of unity, the axion mass starts to play a significant role, and the approximated expression in eq. (3.19) ceases to be valid. Naturally, this ratio also depends on the distance r considered in the calculation of $p_{\mathrm{a}\to\gamma}$. However, using the dipole magnetic model, it is observed that already at distances $r \sim 10\,\mathrm{R_{WD}}$, the amplitude of the integrand has dropped by almost four orders of magnitude, meaning the substantial contribution to the conversion probability has already been evaluated. Therefore, we can set $r = 10\,\mathrm{R_{WD}}$ in eq. (3.20) and observe that $I \lesssim 1$ for axion masses $m_a \lesssim 10^{-5}\,\mathrm{eV}$.

Using eq. (3.13)—or eq. (3.19) in the axion massless case—we can compute the energy probability profile $p_{\mathrm{a}\to\gamma}(\omega)$ needed in eq. (3.1). Once the distance to the white dwarf under observation, d_{WD}, is determined, we have all the necessary ingredients to calculate the axion-induced X-ray flux $dF_{\mathrm{a}\gamma}/d\omega$ in terms of the product of the couplings $g_{aee} \times g_{a\gamma\gamma}$.

3.2 Modeling the detector response

Let us continue with the description of our pipeline. Given that the final goal is to perform a statistical analysis of the data from an observation, it is crucial to incorporate the response of the instrument used into our signal model. In general, characterizing the response and performance of a measurement system is complex, as they depend on several parameters. Here, we will focus on two fundamental aspects relevant to the type of astrophysical observations we are interested in.

3.2.1 Bandwidth and energy resolution

The energy bandwidth is defined as the energy interval over which the instrument has adequate detection efficiency, i.e. over which it is observationally employed. The effective area $\mathcal{A}_{\mathrm{eff}}(\omega)$ of the telescope accounts for the geometric area of the mirror and any factors in vignetting, obscuration, and detector quantum efficiency. This quantity helps us select the suitable energy range, cutting off both very low and very high energies where the detector's efficiency drops. Indeed, given the axion-induced flux spectrum $\mathrm{d}F_{\mathrm{a}\gamma}/\mathrm{d}\omega$, the differential number of expected photons with energy ω after a T_{obs} observation is given by

$$\omega \frac{\mathrm{d}N_{\mathrm{true}}}{\mathrm{d}\omega}(\omega) = \frac{\mathrm{d}F_{\mathrm{a}\gamma}}{\mathrm{d}\omega}(\omega)\mathcal{A}_{\mathrm{eff}}(\omega)T_{\mathrm{obs}}. \tag{3.21}$$

However, this is still not the final observed spectrum. In fact, within the bandwidth of the instrument, the energy resolution can play an important role, quantifying the capability of measuring the energy separation between two equally strong spectral lines. For a quantitative handling of the data, the energy resolution is taken into account through the use of convolutions, so that the measurement result can be described by a convolution of the real signal and the response function of the telescope:

$$\frac{\mathrm{d}N_{\mathrm{obs}}}{\mathrm{d}\omega}(\omega) = \int_{-\infty}^{+\infty} \frac{\mathrm{d}N_{\mathrm{true}}}{\mathrm{d}\omega'}(\omega') \times R(\omega, \omega')\, d\omega'. \tag{3.22}$$

Here $R(\omega, \omega')$ is the spectral response function of the instrument, which describes how the observed energy ω of the photons is distributed relative to their actual energy ω'. Hence, the integral over the unobserved true energy in eq. (3.22) gives the mean of the energy signal, weighted according to the impact of the measuring system. Typically the spectral response function is a Gaussian function

$$R(\omega, \omega') = R(\omega - \omega') = \frac{1}{\sqrt{2\pi}\sigma}\, e^{-\frac{(\omega-\omega')^2}{2\sigma^2}}.$$

We will soon see in section 3.2.2 the implementation of a Gaussian response function in the signal convolution. Since some statistical analyses require binned data, it is sensible to divide the expected signal in eq. (3.22) in N_{bins} of width $\Delta\omega_i$. Finally, integrating eq. (3.21) over $\Delta\omega_i$, we obtain the expected number of observed photons in the i-th energy bin:

$$N_{\mathrm{obs},i} = \int_{\Delta\omega_i} \frac{\mathrm{d}N_{\mathrm{obs}}}{\mathrm{d}\omega}\, d\omega. \tag{3.23}$$

Hence, our model predicts the number of photon counts in the i-th energy bin due to axion emission $s_i \equiv N_{\mathrm{obs},i} \propto (g_{aee} \times g_{a\gamma\gamma})^2$. Already at this stage, assuming a likelihood distribution for the number of observed photons n_i during the observation, it would be possible to conduct a statistical analysis to constrain the value of $g_{aee} \times g_{a\gamma\gamma}$, or to make an axion discovery claim.

3.2.2 The point spread function

Let us now discuss the parameters related to the spatial distribution of the signal. Since we are interested in narrow-field imaging, i.e. on the observation of a single source (the white dwarf), we will disregard the *field of view* (FOV) parameter, assuming that the effective area is spatially constant. However, it is necessary to incorporate the spatial spreading of the signal into the model. Similar to the energy response function, the telescope's spatial resolution effect is handled through the convolution of the incoming signal with a spatial response function, known as the *point spread function* (PSF), which describes how the true signal is spread across the detector's surface. In our case, the observed white dwarf can be considered a point-like source, so that the incoming signal is a two-dimensional Dirac delta in the detector coordinates (x, y).

Modeling the PSF of an instrument is quite complex and requires consideration of various physical contributors, such as optics, detector characteristics, and atmospheric effects (for ground-based telescopes). Here, we continue developing our signal template by using a Gaussian function as a simple parametrization for the telescope's PSF.

The convolution of a point-like signal with a Gaussian function in two dimensions (with detector coordinates related to some astronomical coordinates of the source) results in a shift and intensity modulation of the Gaussian, based on the position and intensity of the point-like signal. Consider an incoming point-like signal in the detector coordinates

$$I_{\text{in}}(x, y) = I_0 \cdot \delta(x - x_0)\, \delta(y - y_0),$$

that has a peak I_0 at (x_0, y_0) and is zero elsewhere. The Gaussian function $G(x, y)$, is described by:

$$G(x, y) = \frac{1}{2\pi\sigma_x\sigma_y} e^{-\left(\frac{(x-\mu_x)^2}{2\sigma_x^2} + \frac{(y-\mu_y)^2}{2\sigma_y^2}\right)}, \tag{3.24}$$

where (μ_x, μ_y) is the center of the Gaussian and (σ_x, σ_y) are the standard deviations along the x- and y-axes. The convolution of I_{in} with $G(x, y)$ defines the measured signal:

$$I_{\text{out}}(x, y) = (I_{\text{in}} * G)(x, y) = \int I_0 \cdot \delta(u - x_0)\delta(v - y_0) G(x - u, y - v)\, du\, dv. \tag{3.25}$$

Applying the delta's property, which "samples" the function with which it is

convoluted at the point where the delta is nonzero, we obtain:

$$I_{\text{out}}(x, y) = I_0 \cdot G(x - x_0, y - y_0). \tag{3.26}$$

This means that the measured signal result is simply the Gaussian function translated so that its center is at the point (x_0, y_0), with the original intensity modulated with I_0.

In section 3.2.1, we saw that the expected signal intensity in the i-th energy bin is $N_{\text{obs},i}$. Considering the telescope's spatial resolution, the observed signal becomes

$$S_i(x, y) = N_{\text{obs},i} \cdot G(x - x_0, y - y_0), \tag{3.27}$$

where (x_0, y_0) is the position of the white dwarf expressed in detector coordinates. The standard deviations (σ_x, σ_y) are characteristic of the instrument used and the specific observation performed.

The most common types of detectors employed in X-ray telescopes are CCD (Charge-Coupled Device) sensors. They consist of a grid of tiny, light-sensitive elements called pixels. Although the EM signal arrives at the detectors as a continuous function, the discrete pixels in the detectors integrate it and measure the intensity of the wave in their respective area. We can reproduce this *pixellation* process by integrating eq. (3.27) over a grid that matches the detector's pixel layout. Therefore, the signal template we have built provides $s_{i,j} \propto (g_{aee} \times g_{a\gamma\gamma})^2$, the predicted number of axion-induced photon counts in the i-th energy bin and the j-th detector pixel.

3.3 Statistical analysis

We now outline the general principles for performing statistical analysis in the context of X-ray observations of WD that we have just described. This section is mostly based on [68], [69]. We are dealing with a counting experiment where the data $n_{i,j}$ represent independent measurements of the number of events observed in the i-th energy bin and the j-th pixel. Consequently, the data are well described by a Poisson likelihood function:

$$L(\boldsymbol{\theta}) = \prod_{i=1}^{N_{\text{bin}}} \prod_{j=1}^{N_{\text{pix}}} \frac{\mu_{i,j}(\boldsymbol{\theta})^{n_{i,j}} e^{-\mu_{i,j}(\boldsymbol{\theta})}}{n_{i,j}!}, \tag{3.28}$$

where

$$\mu_{i,j}(\boldsymbol{\theta}) = s_{i,j}(\theta_s) + b_{i,j}(\boldsymbol{\theta}_b), \tag{3.29}$$

are the contributions from the signal and the background, respectively, and depend on the model parameters $\boldsymbol{\theta} = \{\theta_s, \boldsymbol{\theta}_b\}$. In our case, the signal parameter θ_s is proportional to $(g_{aee} \times g_{a\gamma\gamma})^2$.

We construct now the hypothesis testing procedure to carry out to make a discovery claim or to set an upper limit for the value of $g_{aee} \times g_{a\gamma\gamma}$. For this purpose, we start defining the null hypothesis H_0 that predicts only background, and the signal hypotheses H_1 (which can be parameterized by θ_s). To test a hypothesized value of θ_s, we define the *log-likelihood ratio* test statistic as:

$$t(\theta_s) = -2 \ln \left(\frac{L(\theta_s, \hat{\hat{\boldsymbol{\theta}}}_b)}{L(\hat{\theta}_s, \hat{\boldsymbol{\theta}}_b)} \right). \tag{3.30}$$

Here, $L(\theta_s, \hat{\hat{\boldsymbol{\theta}}}_b)$ is the likelihood function evaluated at the hypothesized value of θ_s and the conditional maximum likelihood estimates (MLEs) $\hat{\hat{\boldsymbol{\theta}}}_b$ of the background parameters $\boldsymbol{\theta}_b$ (and thus is a function of θ_s). The denominator in the logarithm, $L(\hat{\theta}_s, \hat{\boldsymbol{\theta}}_b)$, represents the likelihood function evaluated at the global MLEs of both the signal and background parameters, $\hat{\theta}_s$ and $\hat{\boldsymbol{\theta}}_b$, respectively. High values of $t(\theta_s)$ correspond to a high incompatibility between the data and the tested signal model. The level of disagreement can be quantified using the p-value, formally defined as:

$$p(\theta_s) = \int_{t(\theta_s)_{\text{obs}}}^{\infty} f(t(\theta_s)|\theta_s)\, dt(\theta_s), \tag{3.31}$$

where $f(t(\theta_s)|\theta_s)$ is the probability density function of the statistic $t(\theta_s)$ under the hypothesis θ_s, the second argument gives the value of θ_s assumed for the data distribution. It is also called the *sampling distribution* for the test statistic $t(\theta_s)$. The quantity $t(\theta_s)_{\text{obs}}$ is the value of $t(\theta_s)$ observed from the data.

The p-value allows us to determine the significance with which a certain hypothesis can be rejected. If the null hypothesis H_0 is rejected in favor of the signal hypothesis, we could claim a discovery. Conversely, if our goal is to set limits, the test will be performed on the θ_s signal hypothesis. A low p-value would therefore indicate that such a signal is unlikely given the observed data, allowing us to set an upper limit on θ_s. Then, we define two test statistics, to be used respectively for a discovery claim and for determining the upper limit

on θ_s.

Discovery test statistic

With the purpose of testing the hypothesis with $\theta_s = 0$, we define the test statistic as follows:

$$q(0) = \begin{cases} t(0) = -2\ln\left(\dfrac{L(0,\hat{\hat{\boldsymbol{\theta}}}_b)}{L(\hat{\theta}_s,\hat{\boldsymbol{\theta}}_b)}\right) & \hat{\theta}_s \geq 0, \\ 0 & \hat{\theta}_s < 0, \end{cases} \tag{3.32}$$

where we have chosen to consider only "physical" signal, i.e. models with $\theta_s \geq 0$. If $\hat{\theta}_s < 0$ is found for such models, the best agreement with data occurs for $\theta_s = 0$, so that $q(0) = 0$. This ensures that there cannot be a disagreement between the null hypothesis and the data if the best estimate of the signal is less than zero.

Upper limit determination test statistic

If our goal is determining an upper limit for the signal parameter θ_s, we use the following statistic to test a θ_s signal hypothesis:

$$q(\theta_s) = \begin{cases} -2\ln\left(\dfrac{L(\theta_s,\hat{\hat{\boldsymbol{\theta}}}_b)}{L(0,\hat{\boldsymbol{\theta}}_b(0))}\right) & \hat{\theta}_s < 0, \\ -2\ln\left(\dfrac{L(\theta_s,\hat{\hat{\boldsymbol{\theta}}}_b)}{L(\hat{\theta}_s,\hat{\boldsymbol{\theta}}_b)}\right) & 0 \leq \hat{\theta}_s \leq \theta_s, \\ 0 & \hat{\theta}_s > \theta_s. \end{cases} \tag{3.33}$$

Note that in this case, it is $\hat{\theta}_s > \theta_s$ that does not belong to the rejection region, while if $\hat{\theta}_s < 0$, we use again $\hat{\theta}_s = 0$ as the best estimate for the signal.

In both statistics, the p-value quantifies the disagreement between the data and the hypothesis. Its value is calculated similarly to eq. (3.31), and a sampling distribution for the considered test statistic is needed to evaluate the integral. Fortunately, in the large sample limit, asymptotic formulas can be obtained for the test statistics defined eqs. (3.32) and (3.33). Indeed, the works of Wilks [70] and Wald [71] ensure that the test statistic $t(\theta_s)$ in eq. (4.11) follows a χ^2 distribution with one degree of freedom in the asymptotic limit. These approximations become exact in the large sample limit and have been found to provide accurate results even for fairly small sample sizes [68]. For

very small data samples, Monte Carlo methods can always be used to determine the required distributions.

Chapter 4

Data analysis of RE J0317-853

Having outlined the general framework for axion detection in isolated white dwarfs, we now turn to a specific case study. In this chapter, we will review the results from two key papers: [59] (hereafter referred to as Paper I) and [72] (hereafter referred to as Paper II). By reproducing their results, we aim to demonstrate the effectiveness of the pipeline illustrated in chapter 3.

Paper I proposes observing the X-ray spectrum of the magnetic white dwarf star (MWD) RE J0317-853. This star is an ideal candidate for such observations due to its high core temperature, strong magnetic field, and relative proximity to Earth. These factors contribute to a high expected flux of axion-induced X-ray photons, making RE J0317-853 an optimal target for axion searches (The reader should refer to Section I of the supplementary material in Paper I for a comparison list of WDs, which was constructed using catalogs from [56], [73], [74].).

In Paper II, the authors detail the results of a $\sim$ 40 ks observation of RE J0317-853 conducted with the *Chandra* X-ray telescope. The absence of an observed X-ray signal during this observation allowed the authors to set stringent constraints on the product of the axion-electron and axion-photon couplings, $g_{aee} \times g_{a\gamma\gamma}$.

In section 4.1 we compute the axion-induced X-ray flux spectrum of RE J0317-853. Section 4.2 is dedicated to modeling the *Chandra* instrument response function. Finally in section 4.3 we derive the upper limit on $g_{aee} \times g_{a\gamma\gamma}$.

4.1 Axion-induced X-ray flux from RE J0317-853

Let us apply the procedure outlined in section 3.1 to calculate the axion-induced X-ray flux of RE J0317-853. This section will detail each step and present the quantitative results of the calculations. To help the reader follow the computations, a list of key observations and derived properties of RE J0317-853 is provided in table 4.1.

Table 4.1: Characteristics of the MWD RE J0317-853. Notice the agreement with the values reported in table 3.1.

Quantity	**Value**	**Authors**	**Ref.**
Mass	$1.2 - 1.4\ M_\odot$	Kulebi et al. (2010)	[75]
Radius	$0.003 - 0.004\ R_\odot$	Kulebi et al. (2010)	[75]
Effective temperature	$30\,000 - 50\,000$ K	Barstow et al. (1995)	[76]
Magnetic field	$200 - 800$ MG	Burleigh et al. (1999)	[77]
Rotation period	~ 725 seconds	Ferrario et al. (1997)	[78]
Distance	~ 30 pc	Brown et al. (2021)	[79]
Core temperature	~ 1.38 keV	Dessert et al. (2022)	[72]
Composition	Mainly C, O, Ne, Mg	Dessert et al. (2022)	[72]
Density	$10^6 - 10^8$ g/cm^3	Dessert et al. (2022)	[72]

4.1.1 RE J0317-853's axion emissivity spectrum

We start by detailing the procedure followed to compute the axion emissivity spectrum due to the electron-ion axion bremsstrahlung, we recall here its expression introduced in eq. (3.2)

$$\frac{d\varepsilon_a}{d\omega} = \frac{\alpha_{\rm EM}^2 g_{aee}^2}{4\pi^3 m_e^2} \frac{\omega^3}{e^{\omega/T} - 1} \sum_s \frac{Z_s^2 X_s F_s}{A_s m_u} \rho, \tag{4.1}$$

To evaluate the axion emissivity spectrum for RE J0317-853, we have employed the model of its interior presented in Paper II. In this model, the core temperature $T_c = 1.388(5)$ keV was estimated using WD cooling sequences provided by [80]. This estimation was achieved by fitting the available models over the cooling age to the measured absolute magnitude bands data [74]. This procedure also led to selecting $M_{\rm WD} = 1.22\,M_\odot$ as the best value for the mass of RE J0317-853. The composition and density profiles X_s and ρ of

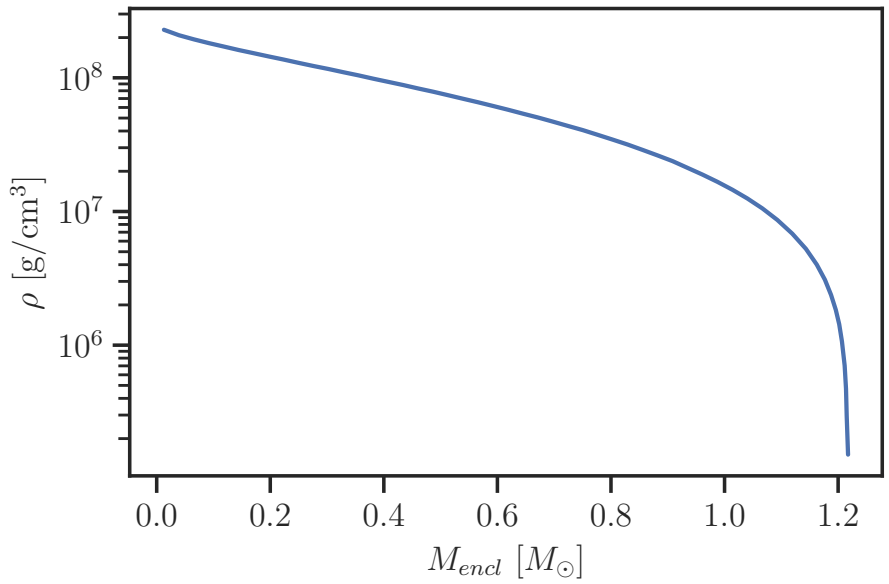

Figure 4.1: Density profile ρ of RE J0317-853 as a function of the mass coordinate M_{encl}. This plot was obtained from the supplementary material of Paper II.

RE J0317-853 were obtained from numerical simulations in Paper II. These simulations tracked the evolution of a white dwarf with RE J0317-853's mass from its formation until it cooled to below the observed luminosity. The density and composition profiles for the four most abundant ions in RE J0317-853 are reported as a function of the *mass coordinate* $M_{encl} = \int_0^{r'} 4\pi r'^2 \rho dr'$ in the supplementary material of Paper II.

We digitized these profiles using the plot digitization software [81], which allowed us to create datasets for numerical calculations using Python. The resulting density and composition profile plots are shown in figs. 4.1 and 4.2.

Numerical Computation of F_s Factors

As mentioned in the previous chapter, the plasma in white dwarfs is strongly coupled, requiring numerical methods to calculate the medium factors F_s for the four species shown in fig. 4.2. First, we computed the profiles of Γ_s for each species using eq. (3.7), identifying the value of M_{encl} at which the phase transition $\Gamma = 178$ occurs, as displayed in fig. 4.3.

Depending on the plasma state at each spherical slice of the WD, we selected the appropriate fitting function for F_s from [61], [62]. These F_s parametrizations were numerically implemented using Python, resulting in

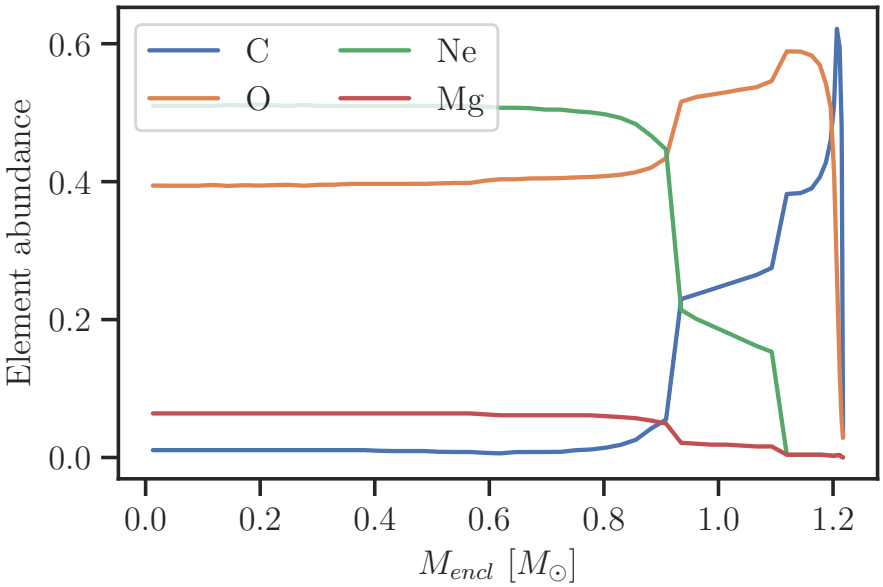

Figure 4.2: Abundance profiles X_s of the four most abundant ions in RE J0317-853 as a function of the mass coordinate M_{encl}. This plot was obtained from the supplementary material of Paper II.

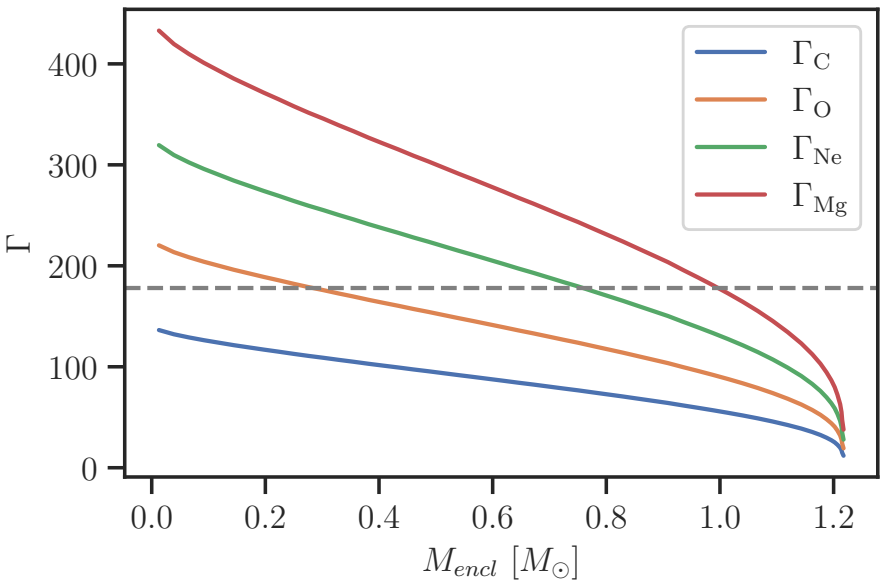

Figure 4.3: Profiles of the coupling parameter Γ_s for the four most abundant species in RE J0317-853. The *dotted gray line* correspond to the threshold value $\Gamma = 178$ at which the phase transition takes place.

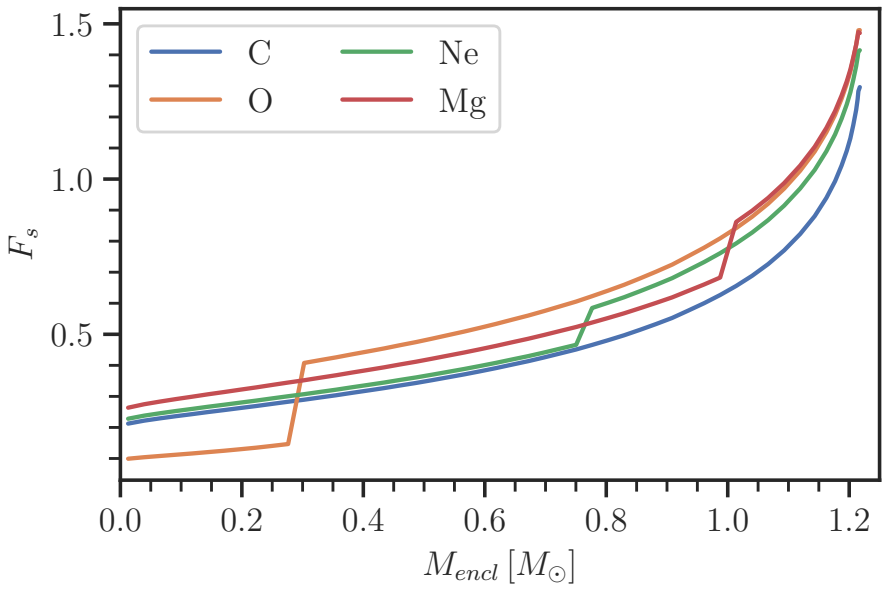

Figure 4.4: The F_s profile for the four most abundant species in RE J0317-853 obtained from the implementation of [61], [62] parametrization in our Python script.

the profiles shown in fig. 4.4.

We also define a weighted sum of the F_s factors:

$$\bar{F} = \frac{\sum_s F_s w_s}{\sum_s w_s} \quad \text{with} \quad w_s = \frac{Z_s^2 X_s}{A_s}, \tag{4.2}$$

which allows us to evaluate the weighted contribution of the various species. The profile is shown in fig. 4.5.

Notice that as one moves toward the center of the star, the density increases, and the plasma becomes increasingly strongly coupled, eventually transitioning to the solid lattice phase. These two different plasma states explain the jumps in the profiles and highlight the axion emission suppression due to the solid phase of the plasma.

In fig. 4.6, we also show the plot for the sum over the species s in eq. (4.1), comparing it with the one presented in Paper II. The difference between the two curves is mainly due to the profile of F_{O}, which differs significantly from that calculated in Paper II. This discrepancy can be attributed to an implementation error in the parameterization used, which does not have a significant impact when integrated into the overall profile of the WD to obtain the axion luminosity.

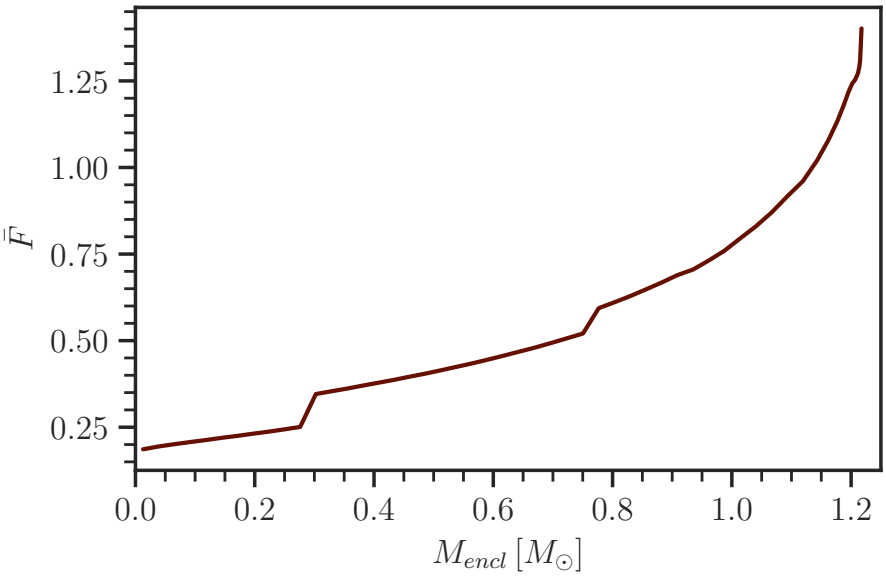

Figure 4.5: Weighted sum of the F_s medium factors of RE J0317-853 shown in fig. 4.4

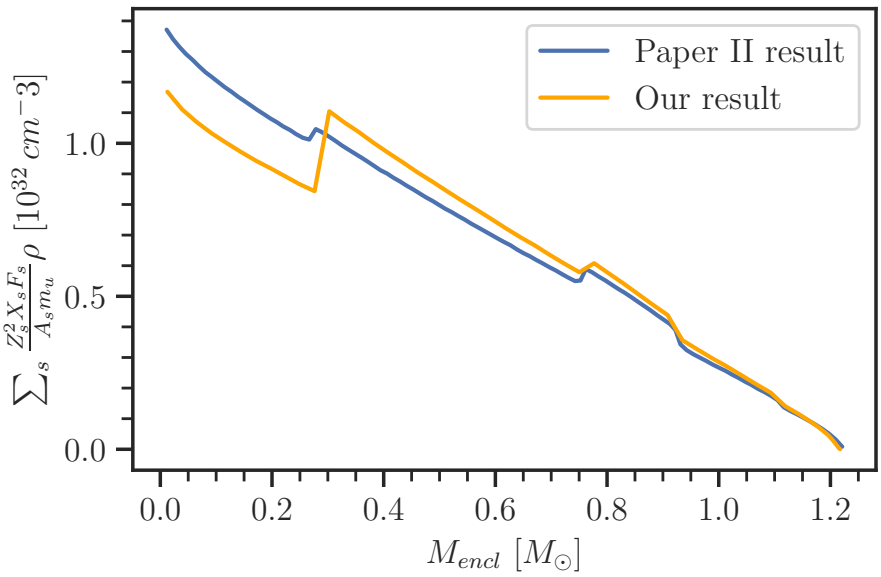

Figure 4.6: *Yellow line*: The profile of the sum in eq. (4.1) obtained using our routine. *Blue line* The same profile shown in the supplementary material of Paper II.

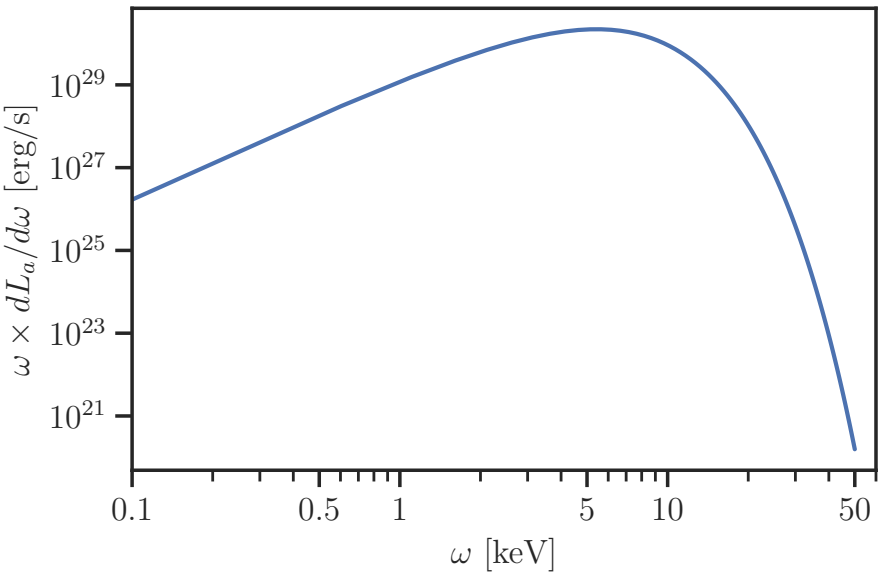

Figure 4.7: Axion luminosity spectrum of RE J0317-853, obtained by setting $g_{aee} = 10^{-13}$ and $T = 1.383\,\mathrm{keV}$. Note that the emission spectrum peaks at energies $\omega \gtrsim \mathrm{keV}$.

RE J0317-853 axion luminosity spectrum

We can now proceed to calculate the axion luminosity spectrum of RE J0317-853 using the expression in eq. (3.4):

$$\begin{aligned}\frac{dL_{\mathrm{a}}}{d\omega}(\omega) &= \int_0^{\mathrm{R_{WD}}} dr\, 4\pi r^2 \frac{d\varepsilon_a}{d\omega}(r) \\ &= \frac{\alpha_{\mathrm{EM}}^2 g_{aee}^2}{4\pi^3 m_e^2} \frac{\omega^3}{e^{\omega/T}-1} \int_0^{\mathrm{R_{WD}}} dr\, 4\pi r^2 \rho(r) \sum_s \frac{Z_s^2 X_s F_s}{A_s m_u}(r) \\ &= \frac{\alpha_{\mathrm{EM}}^2 g_{aee}^2}{4\pi^3 m_e^2} \frac{\omega^3}{e^{\omega/T}-1} \int_0^{M_{\mathrm{WD}}} dM_{encl} \sum_s \frac{Z_s^2 X_s F_s}{A_s m_u}(M_{encl}).\end{aligned} \tag{4.3}$$

The integration was performed using the `scipy.integrate` package. The result, shown in fig. 4.7, was obtained by selecting a value of $g_{aee} = 10^{-13}$, i.e., the current limit placed on the axion-electron coupling (see eq. (2.31)). For the temperature, we chose the conservative value $T = 1.383\,\mathrm{keV}$.

As anticipated, the axions are emitted in the keV energy range, with a peak near $\omega \sim 3\,T$. This spectrum can be analytically integrated over all energies to determine the total axion luminosity. Our calculation yields:

$$L_{\rm a} \simeq 7.84 \times 10^{-4}\,{\rm L}_\odot.$$

This result is consistent with the axion luminosity value reported in Paper II, which is approximately $L_{\rm a} \approx 8 \times 10^{-4}\,{\rm L}_\odot$.

4.1.2 Axion-photon conversion in RE J0317-853's magnetosphere

Following section 3.1.3, we now turn to the computation of the energy profile of the axion-photon conversion probability $p_{{\rm a}\to\gamma}(\omega)$ induced by RE J0317-853's magnetic field. To do so, we use the general expression in eq. (3.13), which we report here:

$$p_{{\rm a}\to\gamma} = \left| \int_{\rm R_{WD}}^{\infty} dr' \Delta_B(r') e^{i\Delta_a r' - i\int_{R_{\rm WD}}^{r'} dr'' \Delta_\parallel(r'')} \right|^2 . \tag{4.4}$$

We have decided to restrict our computation to the case of vanishing axion mass $m_a \to 0$; however, the following method is entirely general and allows for calculating the probability even outside this massless regime. In order to compute the integral in eq. (3.13), we employed numerical methods. Before presenting the results of the computation, we describe the precautions taken into account when performing the numerical integration of eq. (3.13):

- First, we used the pure dipole magnetic field model described in eq. (3.14) to determine the integration upper bound, $\rm R_{max}$, which has to be used in place of `np.inf`. This was done in order to make code executions faster and to avoid unstable behavior and numerical errors of the integration function `scipy.integrate.quad`. The quantity $\rm R_{max}$ was determined by gradually increasing its value and observing when the integral converges to the correct profile given by the axion massless analytical result in fig. 3.2. We have found that at $\rm R_{max} \sim 20\,R_{WD}$ the conversion probability already matches the analytical result.

- Secondly, when we implemented the functions in eqs. (3.15) to (3.17) in `Python`, we optimized them using the `@njit` decorator from the `Numba` library [82]. This optimization was necessary because these functions are called iteratively within loops and by the `scipy.integrate.quad` function. The `@njit` decorator from the `Numba` library significantly reduces execution times by performing just-in-time (JIT) compilation

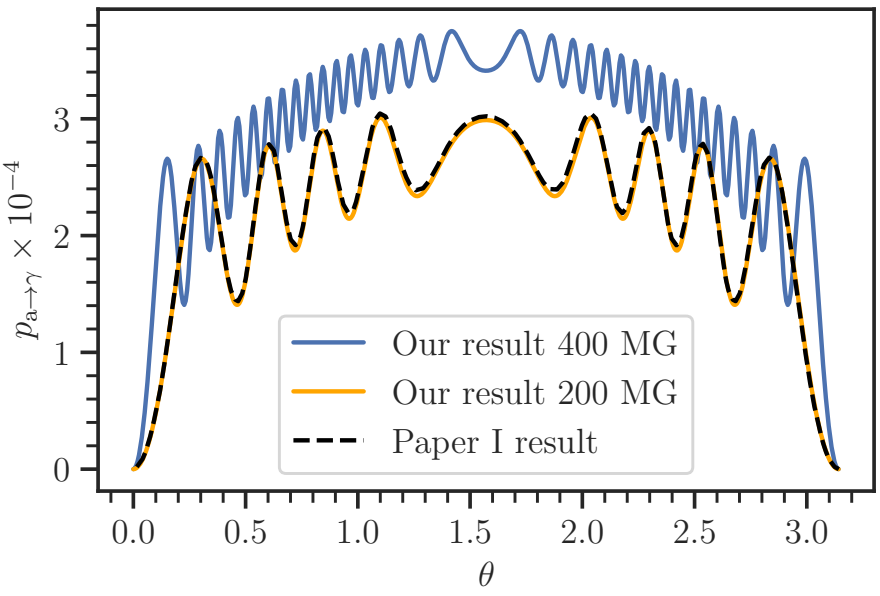

Figure 4.8: The RE J0317-853 conversion probability $p_{a\to\gamma}$ for different values of θ, the angle between the magnetic axis and the radial trajectory, choosing $\omega = 10\,\text{keV}$, $m_a = 10^{-9}\,\text{eV}$, and $g_{a\gamma\gamma} = 10^{-11}\,\text{GeV}^{-1}$. We show both the $B_0 = 400\,\text{MG}$ and $B_0 = 200\,\text{MG}$ results, comparing them to the plot shown in the supplementary material of Paper I

of the decorated functions, avoiding the slowdowns typically associated with Python's interpreted execution.

Given these precautions for the numerical integration of eq. (3.13), we computed the conversion probability $p_{a\to\gamma}$ as a function of the angle θ between the trajectory and the magnetic axis. This allowed us to perform a consistency check with the results shown in Paper I. Figure 4.8 shows the comparison between the plot obtained from our numerical integration and the one presented in Paper I.

As illustrated, using $B_0 = 200\,\text{MG}$ in our Python script yields the same plot as presented in Paper I, which was claimed to be obtained with $B_0 = 400\,\text{MG}$. Despite this discrepancy, we successfully validated our code's accuracy by reproducing the analytical result shown in fig. 3.2. Therefore, we can confidently assert that our code functions correctly, as an error by a factor of 2—such as that between 200 MG and 400 MG—would have been evident.

Having established the reliability of our numerical integration procedure, we can now proceed to calculate the key quantity of interest: the conversion probability $p_{a\to\gamma}(\omega)$ as a function of axion/photon energy ω. To achieve this, it is crucial to understand the geometry of the star's magnetic field, as $p_{a\to\gamma}$

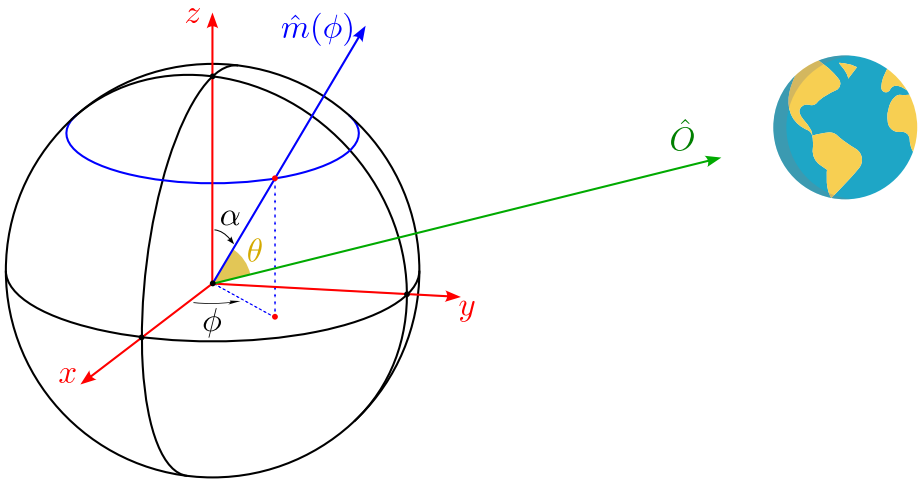

Figure 4.9: Illustration explaining the choice of the coordinate system (x, y, z) and the resulting relationship between the angle θ (between the photon trajectory towards Earth and the magnetic axis) and the angle ϕ (which parameterizes the precession of the dipole moment $\hat{m}$). The right-handed orthonormal basis is chosen such that the WD's rotation axis aligns with the $\hat{z}$-direction, while the remaining x- and y-axes are selected so that the vector pointing to Earth $\hat{O}$ does not project onto the x-axis. The angular coordinates (α, ϕ) are taken as typically done for spherical coordinates. Note the choice of α as the polar angle, since θ was already used.

depends on the angle θ. According to [77], RE J0317-853 observations are well explained by a dipole magnetic field with $B_0 = 363\,\mathrm{MG}$, a $\alpha_O = 51°$ angle between the rotational axis and the observer, a $\alpha_m = 20°$ angle between the rotational axis and the magnetic axis, and a 19% offset along the magnetic axis. To simplify the calculations, we neglected the axis offset and implemented a pure dipole model. Furthermore, to remain consistent with Paper II, we used a magnetic field strength $B_0 = 400\,\mathrm{MG}$.

First, the angle θ can be parameterized in terms of the azimuthal angle ϕ of the dipole moment $\hat{m}$, which varies uniformly with the rotation of RE J0317-853 around its axis. Using our chosen coordinate system described in fig. 4.9, we can express $\theta(\phi)$ as:

$$\theta(\phi) = \arccos\left(\sin\alpha_O \, \sin\alpha_m \, \sin\phi + \cos\alpha_O \cos\alpha_m\right). \tag{4.5}$$

For a fixed axion/photon energy ω, the conversion probability $p_{\mathrm{a}\to\gamma}$ depends on the value of ϕ at which the axion is emitted in our direction, i.e., $p_{\mathrm{a}\to\gamma}(\phi) = p_{\mathrm{a}\to\gamma}(\theta(\phi))$. Given that RE J0317-853's rotation period is $\sim 725\,\mathrm{s}$ [77], which is short compared to the observation time of $\sim 40\,\mathrm{ks}$, it is reasonable to compute

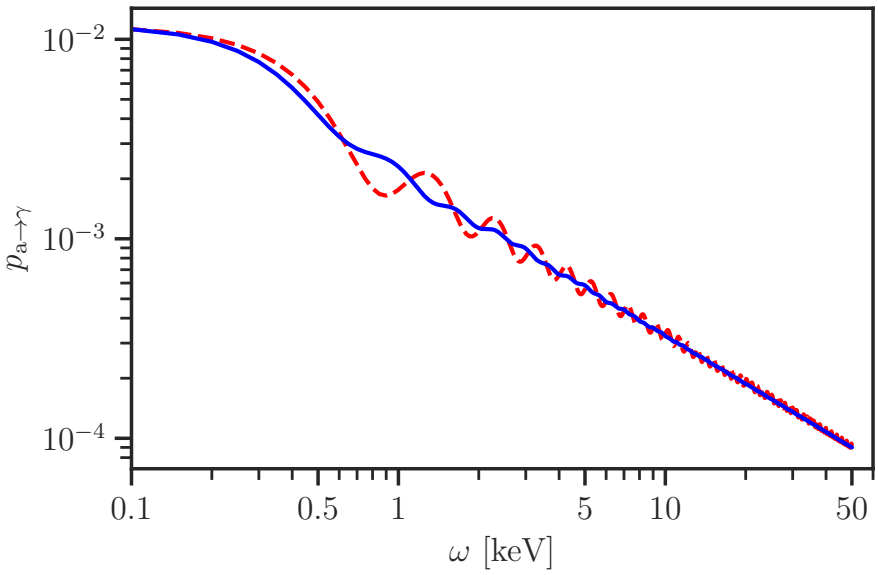

Figure 4.10: *Solid blue line*: The RE J0317-853 conversion probability $p_{a\to\gamma}(\omega)$ as a function of photon energy ω, obtained by averaging over ϕ. *Dotted red line*: The same probability profile but for a fixed angle $\theta = 51°$. Both profiles are calculated for $m_a = 10^{-9}\,\text{eV}$ and $g_{a\gamma\gamma} = 10^{-11}\,\text{GeV}^{-1}$.

$p_{a\to\gamma}$ for a large number of events at uniformly distributed ϕ and then take the average.

$$\langle p_{a\to\gamma}\rangle_\phi = \frac{1}{2\pi}\int_0^{2\pi} p_{a\to\gamma}(\phi)d\phi. \tag{4.6}$$

In practice, we generate a set of uniformly distributed ϕ values and use the relationship between θ and ϕ to find the corresponding θ values. For each θ, we calculate the conversion probability $p_{a\to\gamma}$. We then numerically integrate these probabilities over the range of ϕ values using the trapezoidal rule, implemented with the `np.trapz` function from the `Numpy` library. This process is repeated for a range of energy values $\omega \in [0, 50]\,\text{keV}$, resulting in the energy profile of the average conversion probability $\langle p_{a\to\gamma}\rangle_\phi(\omega)$. In fig. 4.10, we plot this averaged probability profile compared to the result obtained for a fixed angle $\theta = 51°$. Note that, given the characteristics of the magnetic field of RE J0317-853 and the energy range of interest for the axions $\omega \sim 1 - 50\,\text{keV}$, it is possible to use the critical mass index defined in eq. (3.20) with $r = \text{R}_{\text{max}}$ to verify that the massless limit we are considering is a good approximation for low axion masses $m_a \ll 10^{-5}\,\text{eV}$. Therefore, all the results obtained from the analysis will be valid in this specific low-mass range.

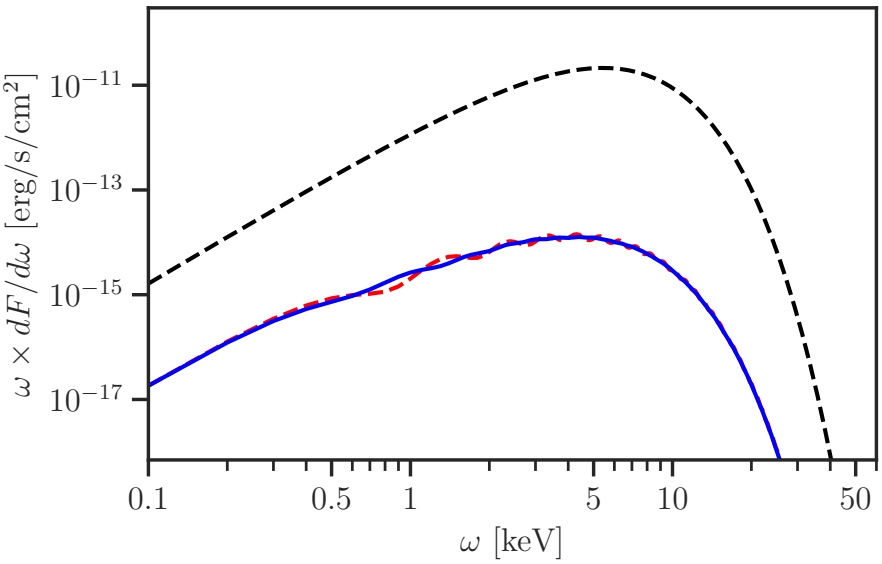

Figure 4.11: *Dotted black line*: The axion flux spectrum of RE J0317-853 computed from the result obtained in section 4.1.1. *Solid blue line*: The axion-induced photon flux spectrum of RE J0317-853 obtained using the averaged $\langle p_{a\to\gamma}\rangle$ energy profile calculated as described in eq. (4.6). The *red dotted line* shows the result for a fixed angle $\theta = 51°$. All plots are obtained by setting $g_{aee} = 10^{-13}$ and $g_{a\gamma\gamma} = 10^{-11}\,\mathrm{GeV}^{-1}$.

Using eq. (3.1), the last quantity needed to compute the axion-induced X-ray flux spectrum is the distance of RE J0317-853 from Earth. Parallax measurements from *Gaia*-DR3 [79] set the RE J0317-853 distance to $d_{\mathrm{WD}} = 29.38(2)\,\mathrm{pc}$. Using a conservative value of $d_{\mathrm{WD}} = 29.40\,\mathrm{pc}$, we obtain the profile shown in fig. 4.11.

4.2 *Chandra* instrument response functions

In this section, we apply the procedure for instrument response modeling described in section 3.2 to the observation of RE J0317-853 with the *Chandra* telescope. To start, we report the characteristics of the observation described in Paper II, where the MWD RE J0317-853 was observed using the Chandra ACIS-I instrument without a grating for a total observation time of $T_{\mathrm{obs}} = 37.42\,\mathrm{ks}$.

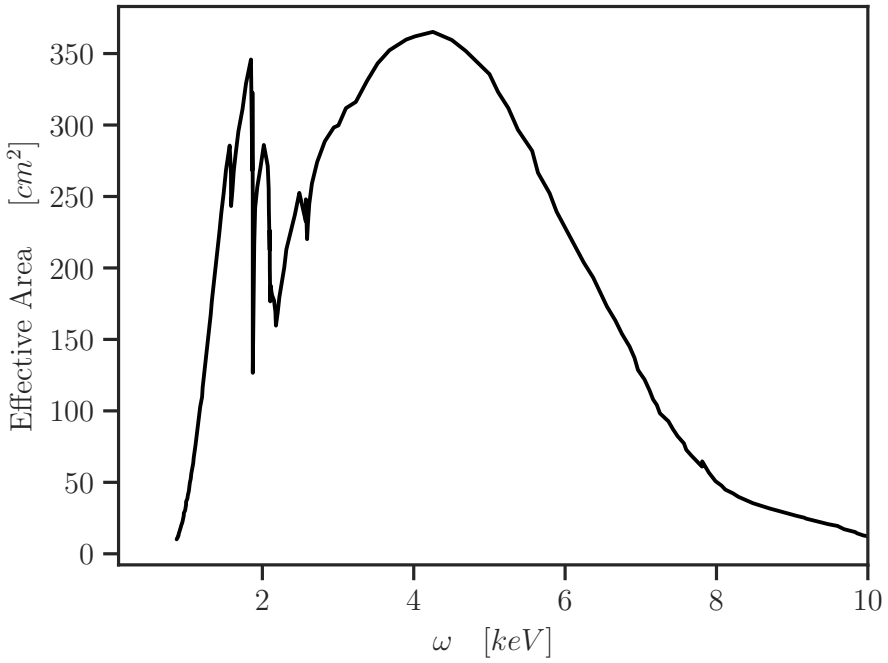

Figure 4.12: Effective area of the ACIS-I detector of the *Chandra* Telescope. Note the energy range of the telescope efficiency. Plot digitized from [83].

4.2.1 *Chandra* energy response funtion

The first instrument parameter we need to determine is the energy bandwidth of the observation. To illustrate this, the effective area profile of the ACIS-I CCDs is shown in fig. 4.12. This profile was obtained by digitizing the effective area plot from the *Chandra* Proposers' Observatory Guide (POG) [83] in a dataset that was subsequently fitted using splines, specifically employing the `PchipInterpolator` routine from the `scipy` library in Python. Using piecewise-cubic Hermite interpolating polynomials (PCHIPs) ensures that the interpolated curve is monotonic between the data points [84], avoiding unrealistic overshoots in the effective area curve.

To maintain consistency with the analysis performed in Paper II, we adopt their choices for energy signal cut-offs and binning. Thus, the expected observed photon signal is divided into four energy bins, each with a width of 2 keV, ranging from 1 to 9 keV. Given that the bin width $\Delta\omega = 2\,\mathrm{keV}$ is more than 20 times greater than the energy resolution of the ACIS detector ($\lesssim 100\,\mathrm{eV}$), the energy response function described in section 3.2.1 has a negligible effect and is therefore omitted from the analysis.

Now, we construct a histogram describing our signal prediction similar to

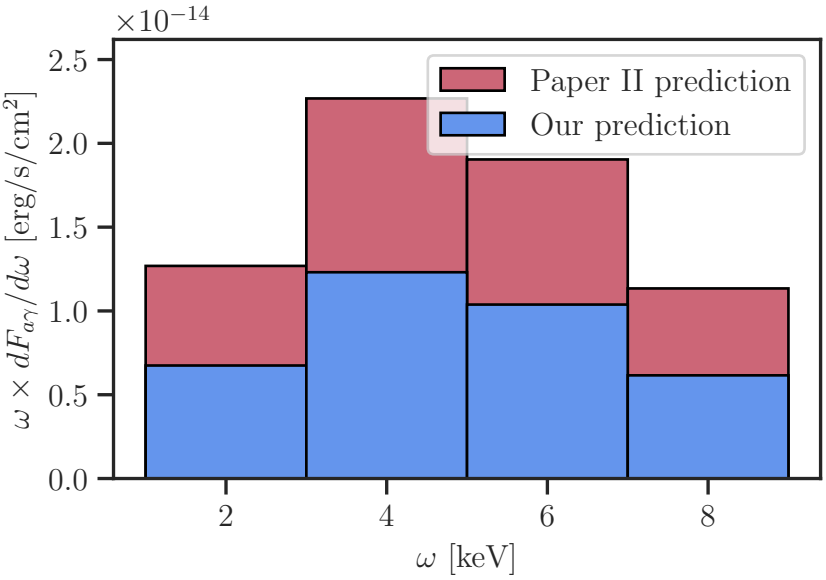

Figure 4.13: Comparison between the $\omega \times \frac{dF_{a\gamma}}{d\omega}$ histogram for RE J0317-853 as reported in Paper II and the one obtained from our signal prediction. The product of couplings is set to $g_{aee} \times g_{a\gamma\gamma} = 10^{-24}\,\mathrm{GeV}^{-1}$.

the one shown in Paper II. By defining the bin centers $\bar{\omega}_i = \{2, 4, 6, 8\}\,\mathrm{keV}$, we compute our histogram entries as:

$$h_i = \bar{\omega}_i \times \int_{\Delta\omega_i} \frac{\mathrm{d}F_{a\gamma}}{\mathrm{d}\omega}\,\mathrm{d}\omega \times \frac{1}{\Delta\omega_i} \quad i = 1, ..., 4. \tag{4.7}$$

We compare the two histograms in Figure 4.13. We observe an overall factor of approximately 1.85 between the two results, indicating that our procedure successfully recovers the same flux spectrum shape obtained in Paper II but predicts a less intense signal. This discrepancy could be due to certain steps, such as the calculation of the F_s medium factors and the computation of the conversion probability, which were challenging to reproduce and required approximations.

Finally, we calculate the number of expected photons observed in the i-th energy bin by following the procedure outlined in section 3.2.1. The result is shown in fig. 4.14. For both histograms, the integrals over the energy bins were performed numerically using the `np.trapz` function.

4.2.2 *Chandra* PSF

The final step in obtaining the signal template for the observation described in Paper II is the implementation of the PSF for the *Chandra* telescope. In

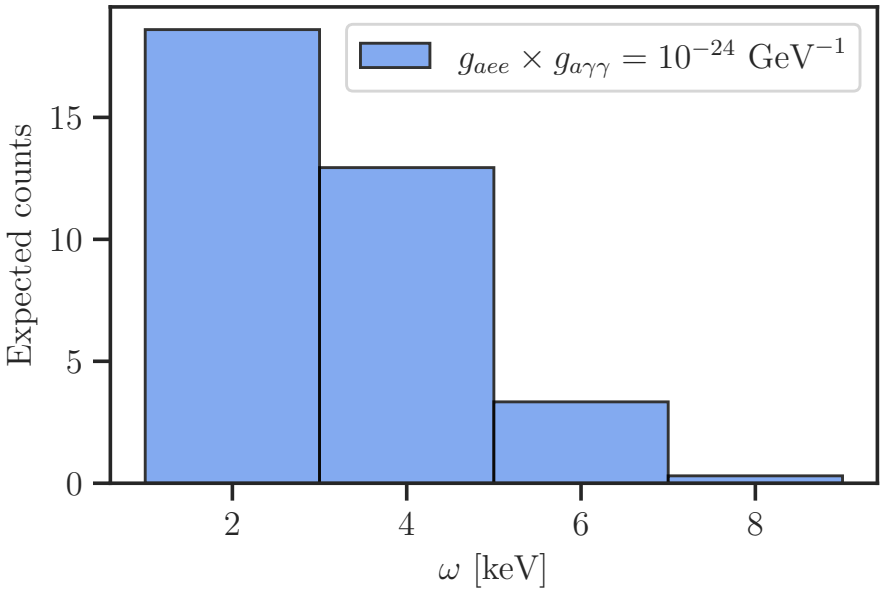

Figure 4.14: Histogram for the expected number of photons from the *Chandra* observation of RE J0317-853. The product of couplings is set to $g_{aee} \times g_{a\gamma\gamma} = 10^{-24}\,\mathrm{GeV}^{-1}$.

Paper II, the CIAO (Chandra Interactive Analysis of Observations) software was used [85]. To adapt our PSF Gaussian parameterization efficiently, we base it on the signal template shown in Paper II, adjusting the source position (x_0, y_0) and standard deviations (σ_x, σ_y) to reproduce it as closely as possible.

Regarding the pixelation process, we reconstructed a pixelated grid in our Python script to emulate the pixels of the ACIS-I detector of *Chandra* based on the signal template image from Paper II. As described in section 3.2.2, for each of the four energy bins, the PSF-convoluted signal was integrated over the grid using the `scipy.integrate.dblquad` function for double numerical integrations. The result for the first energy bin is shown in fig. 4.15. The same image also shows the region of interest (ROI) that will be considered in the data analysis, consistent with what was done in Paper II.

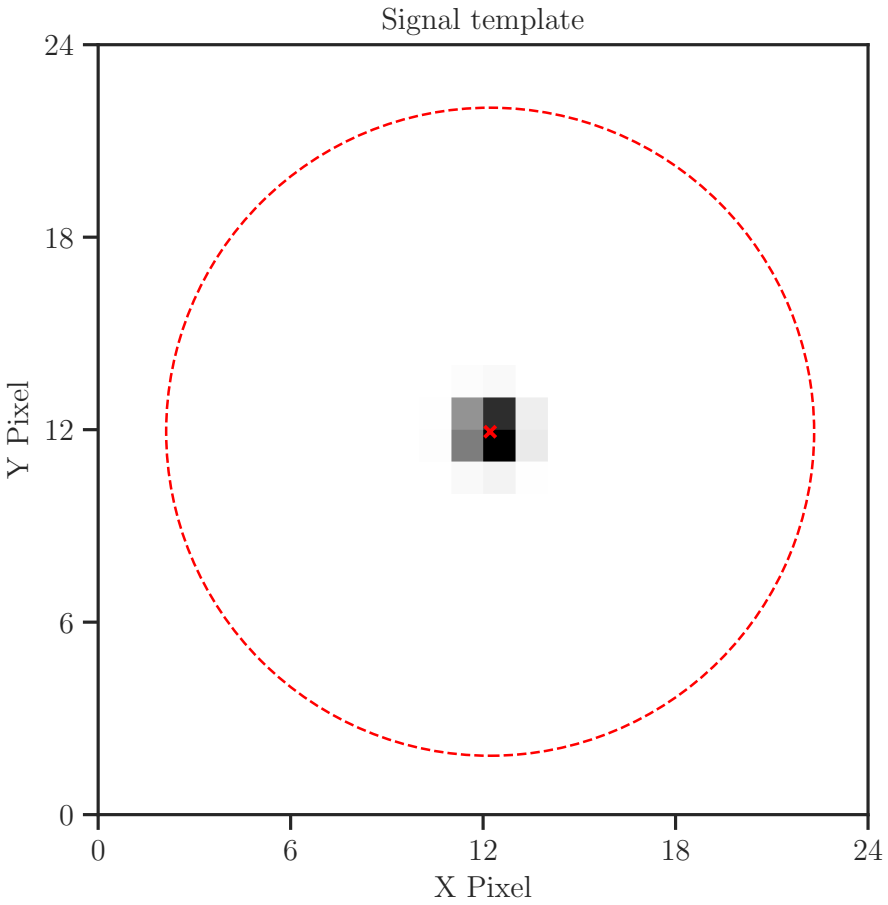

Figure 4.15: Signal template for the first energy bin of the axion-induced X-ray signal from the *Chandra* observation of RE J0317-853. The region of interest (ROI) considered in the data analysis is also indicated, consistent with the approach taken in Paper II.

4.3 Upper limit from RE J0317-853 observation

We now present the results of the RE J0317-853 observation with *Chandra* as described in Paper II. The authors provide a pixelated counts map obtained after data reduction of their observational data. Based on that map, we inserted the observed counts into our grid to perform the data analysis within our framework. We plot in fig. 4.16 our pixelated counts' map.

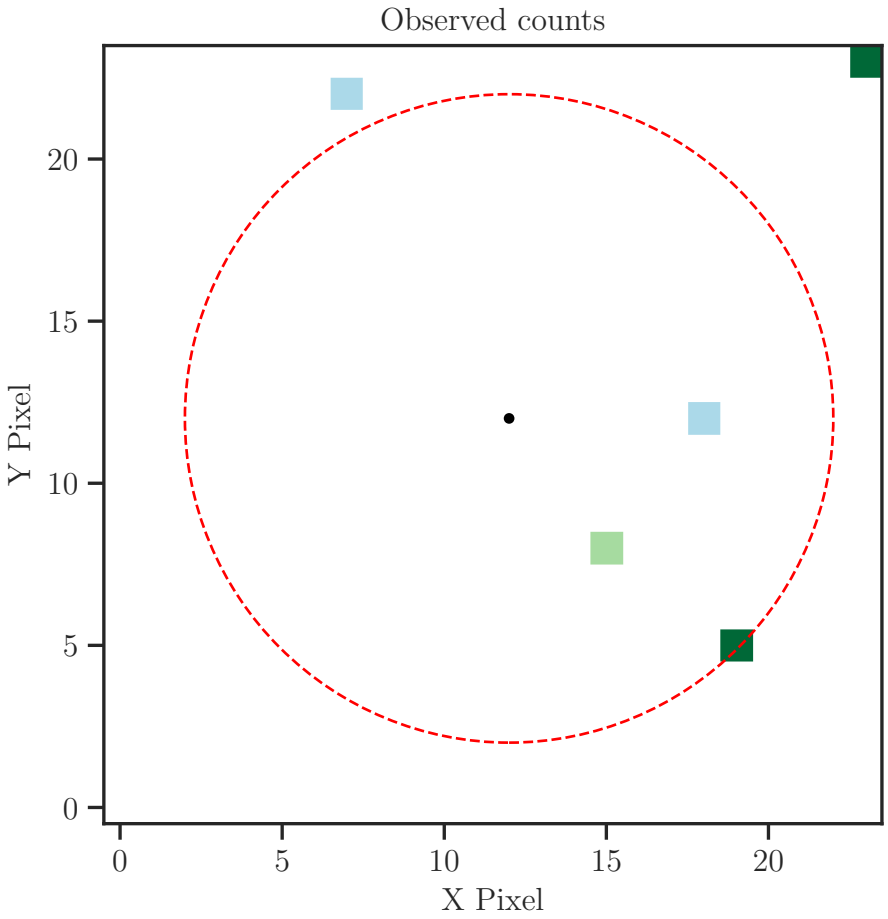

Figure 4.16: Pixelated map of the photon counts observed during the *Chandra* observation of RE J0317-853 after data reduction. The map shows the distribution of observed counts, with no clear excess of photons in the vicinity of the source.

As shown in the figure, the data indicate no clear excess of photons in the vicinity of the source. We proceed to set an upper limit on $g_{aee} \times g_{a\gamma\gamma}$, as described in section 3.3.

4.3.1 A simplified analysis

Before conducting the statistical analysis within the framework that includes spatial information given by the *Chandra* PSF, we will simplify the process by considering only the energy spectrum information of the expected and observed signals. Firstly, we eliminate the two observed counts that are outside the region of interest. In this simplified analysis, the histogram in fig. 4.17 summarizes the observational data.

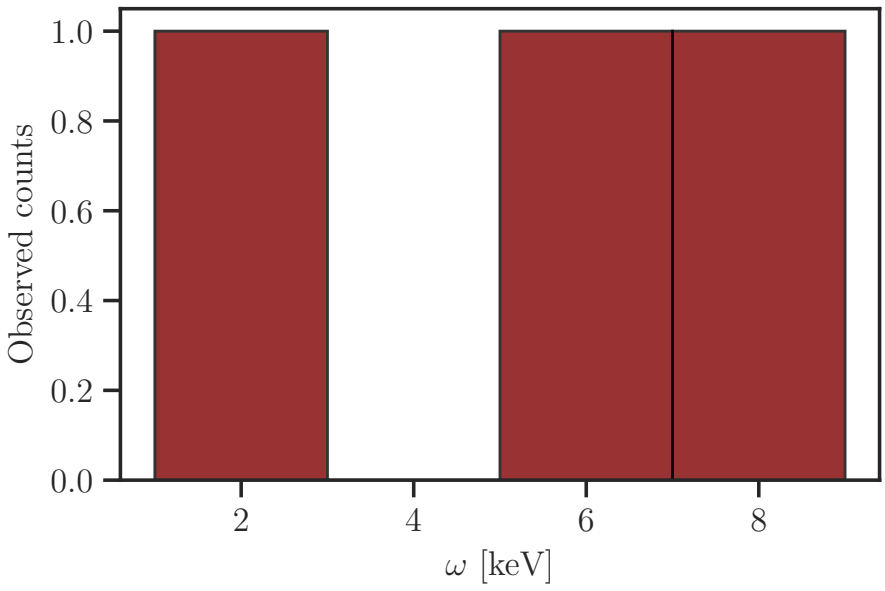

Figure 4.17: Histogram of the observed photon counts from the *Chandra* observation of RE J0317-853.

As described in section 3.3, we proceed to analyze the data $\{n_i\}$ using the Poisson likelihood:

$$L(\boldsymbol{\theta}) = \prod_{i=1}^{4} \frac{\mu_i(\boldsymbol{\theta})^{n_i} e^{-\mu_i(\boldsymbol{\theta})}}{n_i!}, \tag{4.8}$$

where

$$\mu_i(\boldsymbol{\theta}) = s_i(\theta_s) + b_i(\boldsymbol{\theta}_b). \tag{4.9}$$

The signal parameter θ_s is defined by normalizing $g_{aee} \times g_{a\gamma\gamma}$ with the typical energy scale of our prediction:

$$\theta_s = \left(\frac{g_{aee} \times g_{a\gamma\gamma}}{10^{-24}\,\mathrm{GeV}^{-1}} \right)^2. \tag{4.10}$$

The background parameters $\boldsymbol{\theta}_b$ depend on the specific choice of background model utilized. In our statistical analysis, different models will be considered, evaluating the impact of this choice on the upper limit found for θ_s (and consequently for $g_{aee} \times g_{a\gamma\gamma}$). To do this, we first have to select the correct log-likelihood test statistic as expressed in eq. (3.33). Let us now detail the general steps followed to implement the statistical analysis routine in our script:

1. **Compute the best-fit parameters**: Compute the MLEs for the pa-

rameters, $\hat{\boldsymbol{\theta}} = \{\hat{\theta}_s, \hat{\boldsymbol{\theta}}_b\}$ by performing a global minimization of

$$-\ln\left(L(\theta_s, \boldsymbol{\theta}_b)\right),$$

using the `scipy` minimization function `minimize` [86].

2. **Construct $q(\theta_s)$ profile for a range of θ_s values**: Since we have always found the MLE for the signal to be $\hat{\theta}_s \geq 0$, we construct the test statistics

$$q(\theta_s) = -2\ln\left(\frac{L(\theta_s, \hat{\hat{\boldsymbol{\theta}}}_b)}{L(\hat{\theta}_s, \hat{\boldsymbol{\theta}}_b)}\right), \tag{4.11}$$

where $\hat{\hat{\boldsymbol{\theta}}}_b$ are the background parameters optimized for a fixed value of θ_s. Therefore, we have performed iterative conditional optimizations on the background parameters for a range of θ_s values, each time using the best-fit background parameters from the previous iteration as the initial guess. This way, the function eq. (4.11) is evaluated on a grid of θ_s.

3. **Determine the upper limit**: Finally we constrain θ_s at the 95% level of significance. We exploit the asymptotic formula for the test statistic in eq. (4.11), as explained at the end of section 3.3. Thus, we identify the value of θ_s at which the $q(\theta_s)$ crosses the threshold $\bar{q} = 3.84$, finally obtaining the confidence upper limit for $g_{aee} \times g_{a\gamma\gamma}$ by inverting eq. (4.10).

These steps are independent of the specific background model employed in the analysis. Let us see this procedure effectively at play for different background models.

Free background model

In this background model, the four background counts in each energy bin are directly considered as nuisance parameters, $\boldsymbol{\theta}_b = \{b_i\}$. The best parameters are found to be $\{\hat{\boldsymbol{\theta}}_b\} = \{n_i\}$ so that the data are all explained by the background. We followed the procedure just detailed, obtaining the following bound for $g_{aee} \times g_{a\gamma\gamma}$ for low axion masses $m_a \ll 10^{-5}\,\text{eV}$:

$$g_{aee} \times g_{a\gamma\gamma} \lesssim 3.39 \times 10^{-25}\,\text{GeV}^{-1} \quad \text{at } (2\sigma). \tag{4.12}$$

Constant background model

Let us now consider the simplest background model, i.e. the one parametrized by a single parameter $\boldsymbol{\theta}_b = C$ that predicts the same counts in each energy bin $b_i = C$. Again the best signal parameter found through ML estimation is $\hat{\theta}_s = 0$, while the background parameter is found to be $\hat{C} \simeq 0.75$. Our analysis yielded the following constraint for low masses $m_a \ll 10^{-5}\,\text{eV}$:

$$g_{aee} \times g_{a\gamma\gamma} \lesssim 3.35 \times 10^{-25}\,\text{GeV}^{-1} \quad \text{at } (2\sigma). \tag{4.13}$$

Linear background model

We consider here a model for which the background signal varies linearly in the signal spectrum:

$$\frac{dN_{\text{bkg}}}{d\omega} = M \cdot \left(\frac{\omega}{1\,\text{keV}}\right) + Q. \tag{4.14}$$

This model implies that the number of background counts in the i-th energy bin $[2i-1, 2i+1]\,\text{keV}$ is given by

$$\begin{aligned} b_i &= \int_{\Delta\omega_i} \frac{dN_{\text{bkg}}}{d\omega} d\omega = \left(\frac{M}{2} \cdot [(2i+1)^2 - (2i-1)^2] + Q \cdot \Delta\omega_i\right) \times \text{keV} \\ &= (4M \cdot i + 2Q) \times \text{keV} \equiv m \cdot i + q \qquad i = 1, ..., 4, \end{aligned} \tag{4.15}$$

where we have defined the dimensionless parameters $\{m, q\}$ by a proper normalization of $\{M, Q\}$. In this case, the background parameters are $\boldsymbol{\theta}_b = \{m, q\}$. We repeat the analysis routine and we find the low axion mass $m_a \ll 10^{-5}\,\text{eV}$ constraint:

$$g_{aee} \times g_{a\gamma\gamma} \lesssim 3.63 \times 10^{-25}\,\text{GeV}^{-1} \quad \text{at } (2\sigma). \tag{4.16}$$

Power law background model

The last model we will analyze is a two-parameter power-law background model. This background model is well-motivated physically, as power-law spectra frequently appear in astrophysics [87]. In particular, accreting binary systems can produce X-ray falling spectra that can be modeled with a power-law distribution [58], [88]. Similarly to the linear case, we start from a background spectrum

$$\frac{dN_{\rm bkg}}{d\omega} = K \cdot \left(\frac{\omega}{1\,\text{keV}}\right)^{-\alpha}, \tag{4.17}$$

so that the background counts in the i-th energy bin, $i = 1, ..., 4$ are expressed as

$$\begin{aligned} b_i = \int_{\Delta\omega_i} \frac{dN_{\rm bkg}}{d\omega} d\omega &= \begin{cases} \dfrac{K}{-\alpha+1} \cdot [(2i+1)^{-\alpha+1} - (2i-1)^{-\alpha+1}] \times \text{keV} & \alpha \neq 1 \\ K \cdot \ln\left(\dfrac{2i+1}{2i-1}\right) \times \text{keV} & \alpha = 1 \end{cases} \\ &= \begin{cases} \dfrac{k}{-\alpha+1} \cdot [(2i+1)^{-\alpha+1} - (2i-1)^{-\alpha+1}] & \alpha \neq 1 \\ k \cdot \ln\left(\dfrac{2i+1}{2i-1}\right) & \alpha = 1 \end{cases} \end{aligned} \tag{4.18}$$

Again, we have defined the background parameters $\boldsymbol{\theta}_b = \{k, \alpha\}$ to be dimensionless quantities. We repeat the analysis routine and we find the constraint for $m_a \ll 10^{-5}\,\text{eV}$:

$$g_{aee} \times g_{a\gamma\gamma} \lesssim 3.80 \times 10^{-25}\,\text{GeV}^{-1} \quad \text{at } (2\sigma), \tag{4.19}$$

The constraints obtained from this simplified analysis are approximately two orders of magnitude stronger than the one obtained from the CAST experiment for low axion masses in eq. (2.30).

We present in fig. 4.18 the plots showing the log-likelihood ratio profiles $q(\theta_s)$ for the different background models, along with the corresponding results. It is noteworthy that for the first three background models, the global optimization of the likelihood yielded $\hat{\theta}_s = 0$, with the background signal fitting all the observed counts. However, for the power-law background model, the minimum was obtained at $\hat{\theta}_s \simeq 0.18$, suggesting a non-vanishing axion signal as the best fitting model. We can now use the discovery statistic defined in eq. (3.32) to assess the no-signal hypothesis H_0. Given the low value obtained

$$q(0) \simeq 0.14,$$

we conclude that the observed counts are very well explained by the background only, thus we cannot reject the null hypothesis H_0 due to its low statistical significance.

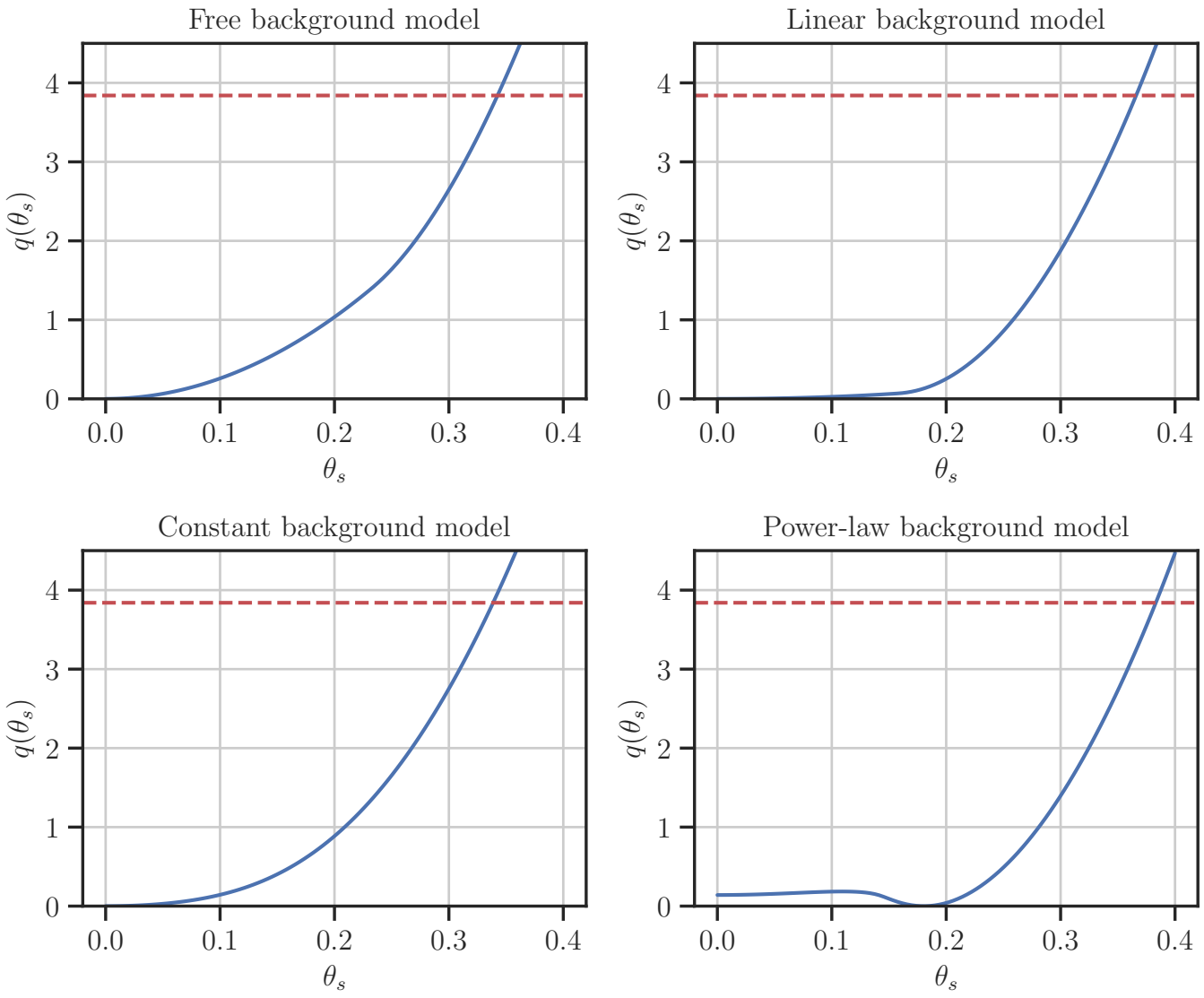

Figure 4.18: *Blue solid lines*: The log-likelihood profiles $q(\theta_s)$ obtained implementing different background models. The *red dotted line* corresponds to the 95% C.L. threshold obtained using the large-sample limit, $\bar{q} = 3.84$.

4.3.2 Including spatial information

We now add a layer of complexity to our analysis by considering the spatial spreading of the signal. Similar to the previous case, we analyze the data using the Poisson likelihood:

$$L(\boldsymbol{\theta}) = \prod_{i=1}^{N_{\text{bin}}} \prod_{j=1}^{N_{\text{pix}}} \frac{\mu_{i,j}(\boldsymbol{\theta})^{n_{i,j}} e^{-\mu_{i,j}(\boldsymbol{\theta})}}{n_{i,j}!}, \tag{4.20}$$

where $n_{i,j}$ represent independent measurements of the number of events observed in the i-th energy bin and the j-th pixel, N_{pix} is the number of grid's pixel considered in the analysis, and $\mu_{i,j}(\boldsymbol{\theta}) = s_{i,j}(\theta_s) + b_{i,j}(\boldsymbol{\theta}_b)$. We have previously described how the pixelation process of the histogram in fig. 4.14 yields the signal prediction $s_{i,j}$ for every choice of $g_{aee} \times g_{a\gamma\gamma}$ (and thus is a function of the normalized signal parameter θ_s). The background models discussed earlier can be easily extended to this new framework by considering $b_{i,j}(\boldsymbol{\theta}_b) = b_i(\boldsymbol{\theta}_b)$ to be the same for every pixel j within the same energy bin i.

As mentioned earlier, pixels outside the region of interest will be excluded from the analysis. This was implemented in our script using a circular mask that excludes pixels in our grid that are farther from the source than the ROI radius. The number N_{pix} is reduced accordingly.

We now run again our analysis routine in this new framework for the different background models. This time, the various models do not lead to significant differences, all yielding the same upper limit for θ_s. We choose to report the limit obtained using the free background model, consistently with the analysis performed in Paper II,

$$g_{aee} \times g_{a\gamma\gamma} \lesssim 2.30 \times 10^{-25}\,\text{GeV}^{-1} \quad \text{at } (2\sigma), \tag{4.21}$$

for axion masses $m_a \ll 10^{-5}\,\text{eV}$. In fig. 4.19 we show the log-likelihood ratio profile resulting from our analysis. As expected, adding spatial information to the analysis results in a significantly stronger limit on $g_{aee} \times g_{a\gamma\gamma}$. Let us now compare this result with the one reported in Paper II for the same mass range:

$$g_{aee} \times g_{a\gamma\gamma} \lesssim 1.30 \times 10^{-25}\,\text{GeV}^{-1} \quad \text{at } (2\sigma). \tag{4.22}$$

The two results are similar, but the one found through our analysis is slightly weaker. We comment here on the possible reasons for this discrepancy:

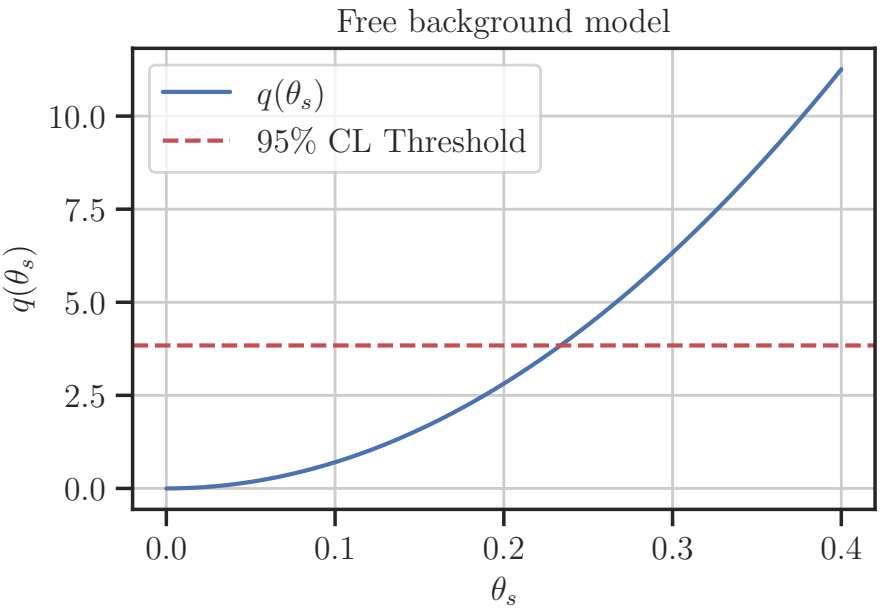

Figure 4.19: Upper limit obtained by incorporating the spatial distribution of the signal in our statistical analysis and using the free background model.

- As highlighted in fig. 4.13, our signal prediction $s_{i,j}$ differs from the one of Paper II by a multiplicative factor of approximately 1.85. Adjusting for this factor, we obtain a much closer limit:

$$g_{aee} \times g_{a\gamma\gamma} \lesssim 1.70 \times 10^{-25}\,\mathrm{GeV}^{-1} \quad \text{at } (2\sigma).$$

  explaining part of the discrepancy.

- We used the large-sample limit to determine the test statistic's threshold that constrains θ_s, even though the observation we are analyzing falls within a low-count regime. Paper II, on the other hand, performed Monte Carlo simulations to set the 95% confidence level threshold, which could explain the remaining difference in the obtained limit.

We emphasize that Monte Carlo simulations have shown that the asymptotic formulas employed in our analysis still provide reasonable results in our case [68].

Chapter 5

Conclusions

In this thesis, we have developed an analysis pipeline for X-ray data from WD observations aimed at probing axion properties. In doing so, we have critically examined and extended the current methodology in the literature, developing Python scripts for performing the numerical computations required in the analysis. We have applied this procedure to the *Chandra* observation of MWD RE J0317-853, utilizing the data and information provided in Dessert et al. (2019, '22) [59], [72] to obtain an upper limit on $g_{aee} \times g_{a\gamma\gamma}$. We now summarize the key results obtained in this thesis:

- Our analysis of RE J0317-853 X-ray data from *Chandra* yielded a limit on $g_{aee} \times g_{a\gamma\gamma}$ in line with [72].
- We extended the current procedure to include several physically motivated background models and quantitatively assessed their impact on the limit on $g_{aee} \times g_{a\gamma\gamma}$.
- In appendix A, we thoroughly calculated the axion emissivity due to electron-ion bremsstrahlung for an extremely degenerate plasma. We corrected a mistake in the expression shown in [20], a result also confirmed by [89].
- We identified a structural limitation for the numerical calculation of the medium factor F in the expression for axion emissivity. The only framework provided in the literature (detailed in [61], [62]) includes parameterizations for F only for a WD plasma composed of a single element. In realistic cases where multiple elements are present, the currently followed procedure may not be entirely adequate.

We provide the reader with an outlook and suggest possible improvements for future analyses and projects of this type:

- Although the different background models implemented did not significantly alter the limit set on $g_{aee} \times g_{a\gamma\gamma}$ using RE J0317-853 observational data, they could have a stronger impact in future analyses.

- We may extend the analysis to specific axion models, particularly non-hadronic axion models, which predict a sizable axion-electron coupling g_{aee}. While the sensitivity of these searches applies to regions of the parameter space most relevant for ALPs, even non-canonical QCD axion models could be impacted by the achievable bounds (see [90], [91] for instance).

- Different processes could extend the analysis, such as the emission of 14.4 keV axions by thermally excited ^{57}Fe nuclides through axion-nucleon coupling [92]–[94]. These axions could be converted in the WD's magnetic field, providing a detectable hard X-ray signal. An analysis similar to the one conducted in this thesis could place significant limits on the product of $g_{a\gamma\gamma}$ with the axion-nucleon coupling.

- Finally, although the pipeline was constructed for analyzing X-ray data from WD observations, we emphasize that it serves as a general and flexible analysis framework. Each component is "self-contained" and can be easily adapted to different phenomenologies and observations. For example, the axion emissivity calculation can be modified for other axion production processes in different astrophysical environments. Additionally, the magnetic field geometry can be modified for axion-photon conversion in contexts other than a pure magnetic dipole field.

Appendix A

Axion bremsstrahlung

Consider the axion effective Lagrangian term describing the axion-electron interaction:

$$\mathcal{L}_{aee} = g_{aee}\frac{\partial_\mu a}{2m_e}\bar{e}\gamma^\mu\gamma_5 e. \tag{A.1}$$

This term can be recast in a pseudoscalar basis, provided that we restrict to a single GB attached to an external fermion line. This is indeed the case for axion bremsstrahlung. Hence, in this context, the Lagrangian term is equivalent to:

$$\mathcal{L}_{aee} = -ig_{aee}a\bar{e}\gamma_5 e. \tag{A.2}$$

The Feynman rule associated with this interaction is:

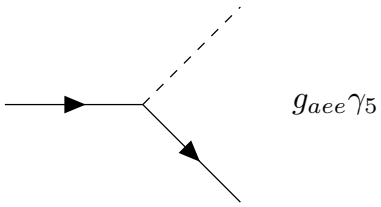

Moreover, the Feynman rule for the QED vertex is

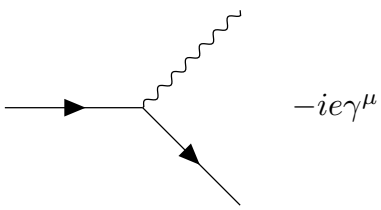

We can use them to first calculate the Axion radiation from an external leg

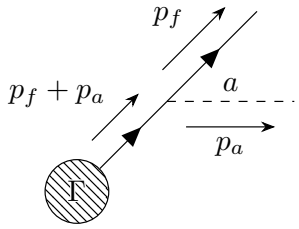

$$\begin{aligned}
&= g_{aee}\bar{u}'\gamma_5 \frac{i}{\not{p}_f + \not{p}_a - m}\Gamma(p_f + p_a) \\
&= ig_{aee}\bar{u}'\gamma_5 \frac{(\not{p}_f + \not{p}_a) + m}{(p_f + p_a)^2 - m^2}\Gamma(p_f + p_a) \\
&= -ig_{aee}\bar{u}' \frac{(\not{p}_f - m) + \not{p}_a}{m_a^2 + 2p_f \cdot p_a}\gamma_5\Gamma(p_f + p_a) \\
&= ig_{aee}\bar{u}' \frac{\gamma_5 \not{p}_a}{m_a^2 + 2p_f \cdot p_a}\Gamma(p_f + p_a).
\end{aligned}$$

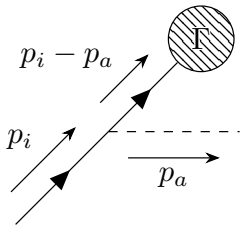

$$\begin{aligned}
&= ig_{aee}\Gamma(p_i - p_a)\frac{(\not{p}_i - \not{p}_a) + m}{(p_i - p_a)^2 - m^2}\gamma_5 u \\
&= ig_{aee}\Gamma(p_i - p_a)\frac{\gamma_5 \not{p}_a}{m_a^2 - 2p_i \cdot p_a}u.
\end{aligned}$$

Now let us compute the amplitude for the axion emission due to bremsstrahlung $e^- + (A, Z) \to e^- + (A, Z) + a$ in the limit of static and heavy nuclei:

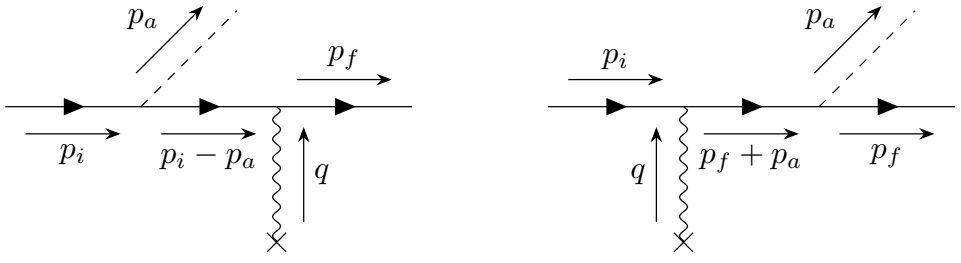

The amplitudes for the two diagrams are denoted with $\mathcal{M}_1$ and $\mathcal{M}_2$ respec-

tively. Then the amplitudes read

$$\mathcal{M}_1 = ig_{aee}\bar{u}'\big(-ie\not{A}_{ext}\big)\frac{\gamma_5\not{p}_a}{m_a^2-2p_i\cdot p_a}u = \frac{Ze^2g_{aee}}{\left|\mathbf{q}\right|^2}\bar{u}'\Big[\frac{\gamma^0\gamma_5\not{p}_a}{m_a^2-2p_i\cdot p_a}\Big]u, \quad \text{(A.3)}$$

$$\mathcal{M}_2 = ig_{aee}\bar{u}'\frac{\gamma_5\not{p}_a}{m_a^2+2p_f\cdot p_a}\big(-ie\not{A}_{ext}\big)u = \frac{Ze^2g_{aee}}{\left|\mathbf{q}\right|^2}\bar{u}'\Big[\frac{\not{p}_a\gamma^0\gamma_5}{m_a^2+2p_f\cdot p_a}\Big]u. \quad \text{(A.4)}$$

Where we have used the fact that the external Coulomb field in momentum space reads $A^{\mu}_{ext}(\mathbf{q}) = \Big(Ze/\left|\mathbf{q}\right|^2, \mathbf{0}\Big)$. Now we compute the complex conjugates of the amplitudes in eqs. (A.3) and (A.4)

$$\mathcal{M}_1^{\dagger} = \Big(\frac{Ze^2g_{aee}}{\left|\mathbf{q}\right|^2}\bar{u}'\Big[\frac{\gamma^0\gamma_5\not{p}_a}{m_a^2-2p_i\cdot p_a}\Big]u\Big)^{\dagger} = \frac{Ze^2g_{aee}}{\left|\mathbf{q}\right|^2}\bar{u}\cdot\gamma_0\Big[\frac{\gamma^0\gamma_5\not{p}_a}{m_a^2-2p_i\cdot p_a}\Big]^{\dagger}\gamma_0\cdot u'$$

$$= \frac{Ze^2g_{aee}}{\left|\mathbf{q}\right|^2}\bar{u}\Big[\frac{\not{p}_a\gamma^0\gamma_5}{m_a^2-2p_i\cdot p_a}\Big]u',$$

$$\mathcal{M}_2^{\dagger} = \Big(\frac{Ze^2g_{aee}}{\left|\mathbf{q}\right|^2}\bar{u}'\Big[\frac{\gamma_5\not{p}_a\gamma^0}{m_a^2+2p_f\cdot p_a}\Big]u\Big)^{\dagger} = \frac{Ze^2g_{aee}}{\left|\mathbf{q}\right|^2}\bar{u}\Big[\frac{\gamma^0\gamma_5\not{p}_a}{m_a^2+2p_f\cdot p_a}\Big]u'.$$

In order to calculate the total unpolarised Feynman amplitude $\left|\overline{\mathcal{M}}\right|^2$ it is necessary to compute the following quantities:

$$\sum_{pol}\mathcal{M}_1\mathcal{M}_2^{\dagger} = \frac{Z^2e^4g_{aee}^2}{\left|\mathbf{q}\right|^4}\frac{1}{[m_a^2-2p_i\cdot p_a][m_a^2+2p_f\cdot p_a]}\,\mathrm{Tr}[\gamma^0\gamma_5\not{p}_a(\not{p}_i+m)\gamma^0\gamma_5\not{p}_a(\not{p}_f+m)],$$

$$\sum_{pol}\mathcal{M}_2\mathcal{M}_1^{\dagger} = \frac{Z^2e^4g_{aee}^2}{\left|\mathbf{q}\right|^4}\frac{1}{[m_a^2-2p_i\cdot p_a][m_a^2+2p_f\cdot p_a]}\,\mathrm{Tr}[\not{p}_a\gamma^0\gamma_5(\not{p}_i+m)\not{p}_a\gamma^0\gamma_5(\not{p}_f+m)],$$

$$\sum_{pol}\left|\mathcal{M}_1\right|^2 = \frac{Z^2e^4g_{aee}^2}{\left|\mathbf{q}\right|^4}\frac{1}{[m_a^2-2p_i\cdot p_a]^2}\,\mathrm{Tr}[\gamma^0\gamma_5\not{p}_a(\not{p}_i+m)\not{p}_a\gamma^0\gamma_5(\not{p}_f+m)],$$

$$\sum_{pol}\left|\mathcal{M}_2\right|^2 = \frac{Z^2e^4g_{aee}^2}{\left|\mathbf{q}\right|^4}\frac{1}{[m_a^2+2p_f\cdot p_a]^2}\,\mathrm{Tr}[\not{p}_a\gamma^0\gamma_5(\not{p}_i+m)\gamma^0\gamma_5\not{p}_a(\not{p}_f+m)].$$

The `Mathematica` package `FeynCalc` [95] is used to compute these quatities. In order to obtain the unpolarised amplitude everything is summed up and divided by the number of initial polarization states (i.e. divide by 2). In addition, it is considered the limit where the mass $m_a = 0$, then the amplitude

reads:

$$
\begin{aligned}
\left|\overline{\mathcal{M}}\right|^2 &= \frac{Z^2e^4g_{aee}^2}{2\left|\mathbf{q}\right|^4}\frac{1}{(p_a\cdot p_i)^2(p_a\cdot p_f)^2}\times \\
&\quad\times\Big\{2\omega_a(p_a\cdot p_i)\Big[2\omega_a(p_a\cdot p_f)(p_i\cdot p_f-m^2)+2\omega_i(p_a\cdot p_f)(p_a\cdot p_i-p_a\cdot p_f)\Big]+ \\
&\quad+2(p_a\cdot p_i)\Big[(p_a\cdot p_f)(p_a\cdot p_f-p_a\cdot p_i)-2\omega_a\omega_f(p_a\cdot p_f)\Big](p_a\cdot p_i-p_a\cdot p_f)\Big\} \\
&= \frac{Z^2e^4g_{aee}^2}{2\left|\mathbf{q}\right|^4}\Big[\frac{4\omega_a^2(p_i\cdot p_f-m^2)}{(p_a\cdot p_i)(p_a\cdot p_f)}+\frac{4\omega_a\omega_i(p_a\cdot p_i-p_a\cdot p_f)}{(p_a\cdot p_i)(p_a\cdot p_f)}+ \\
&\qquad -2\frac{(p_a\cdot p_f-p_a\cdot p_i)^2}{(p_a\cdot p_i)(p_a\cdot p_f)}+\frac{4\omega_a\omega_f(p_a\cdot p_i-p_a\cdot p_f)}{(p_a\cdot p_i)(p_a\cdot p_f)}\Big] \\
&= \frac{Z^2e^4g_{aee}^2}{\left|\mathbf{q}\right|^4}\Big[2\omega_a^2\frac{p_i\cdot p_f-m^2-p_a\cdot(p_f-p_i)}{(p_a\cdot p_i)(p_a\cdot p_f)}+2-\frac{(p_a\cdot p_f)}{(p_a\cdot p_i)}-\frac{(p_a\cdot p_i)}{(p_a\cdot p_f)}\Big].
\end{aligned}
$$

Since the potential is static, the normalized S-matrix element is given by

$$
S_{fi}=2\pi\delta(\omega_i-\omega_f-\omega_a)\Big(\frac{1}{2\omega_iV}\Big)^{1/2}\Big(\frac{1}{2\omega_fV}\Big)^{1/2}\Big(\frac{1}{2\omega_aV}\Big)^{1/2}\mathcal{M}_{fi},
$$

from which we get the transition probability to the final states of the process

$$
\begin{aligned}
d\omega_{fi} &= \frac{\left|S_{fi}\right|^2}{T}d\Pi \\
&= (2\pi)\delta(\omega_i-\omega_f-\omega_a)\Big(\frac{1}{2\omega_iV}\Big)\Big(\frac{d^3p_f}{(2\pi)^3 2\omega_f}\Big)\Big(\frac{d^3p_a}{(2\pi)^3 2\omega_a}\Big)\left|\mathcal{M}_{fi}\right|^2.
\end{aligned}
\tag{A.5}
$$

The differential cross-section is obtained considering this transition probability for one scattering center and unit incident flux. Hence, we have to divide eq. (A.5) by the incident flux $\Phi = n_e v_e$. With our choice of normalization of the states $n_e = 1/V$:

$$
\begin{aligned}
d\sigma &= \frac{\left|\mathcal{M}_{fi}\right|^2}{8\omega_i\omega_f\omega_a v_e}\delta(\omega_i-\omega_f-\omega_a)\frac{d^3p_f d^3p_a}{32\pi} \\
&= \frac{\left|\mathcal{M}_{fi}\right|^2}{16\pi^3}\frac{\left|p_f\right|d\omega_f\omega_a d\omega_a}{\omega_i v_e}\frac{d\Omega_a}{4\pi}\frac{d\Omega_{e'}}{4\pi}\delta(\omega_i-\omega_f-\omega_a).
\end{aligned}
$$

Taking into account the Pauli blocking effect for the final states the differential

cross section reads

$$d\sigma = \frac{\left|\mathcal{M}_{fi}\right|^2}{16\pi^3}\frac{\left|p_f\right|d\omega_f\omega_a d\omega_a}{\omega_i v_e}\frac{d\Omega_a}{4\pi}\frac{d\Omega_{e'}}{4\pi}\delta(\omega_i-\omega_f-\omega_a)(1-f_e(\omega_f,T)).$$

The final state axion does not get the Bose enhancement since axions are not in thermal equilibrium. Then the (differential) number of scattering events per unit of time and volume is given by

$$\begin{aligned} d\gamma &= d\sigma\cdot\frac{dn_e v_e}{g_e}n_N \\ &= n_N\frac{dn_e}{g_e}\frac{\left|\mathcal{M}_{fi}\right|^2}{16\pi^3}\frac{\left|p_f\right|d\omega_f\omega_a d\omega_a}{\omega_i}\frac{d\Omega_a}{4\pi}\frac{d\Omega_{e'}}{4\pi}\delta(\omega_i-\omega_f-\omega_a)(1-f_e(\omega_f,T)). \end{aligned} \tag{A.6}$$

where we are using here the normalization $dn_e = g_e d^3p_i/(2\pi)^3 f_e(\omega_i,T)$ with g_e the number of internal degrees of freedom. We can integrate over $d\Omega_e$ since the process is isotropic and we can use the delta to remove the integration over $d\omega_a$. Summing over the initial and final polarizations of all particles we obtain the unpolarized expression of the scattering rate density. Finally multiplying by the axion energy ω_a, we get the differential energy loss rate per unit of volume (also called *axion emissivity*)

$$\begin{aligned} d\varepsilon &= n_N\frac{\left|\overline{\mathcal{M}}\right|^2}{16\pi^5}d\omega_i f_e(\omega_i,T)d\omega_f(1-f_e(\omega_f,T))\frac{d\Omega_{e'}}{4\pi}\frac{d\Omega_a}{4\pi}\omega_a^2\left|p_f\right|\left|p_i\right| \\ &= \frac{\alpha^2 g_{aee}^2 Z^2 n_N}{\pi^3}d\omega_i f_e(\omega_i,T)d\omega_f(1-f_e(\omega_f,T))\times \\ &\times\frac{d\Omega_{e'}}{4\pi}\frac{d\Omega_a}{4\pi}\frac{\left|p_f\right|\left|p_i\right|\omega_a^2}{\left|\mathbf{q}\right|^4}\left[2\omega_a^2\frac{p_i\cdot p_f - m^2 - p_a\cdot(p_f-p_i)}{(p_a\cdot p_i)(p_a\cdot p_f)} + 2 - \frac{(p_a\cdot p_f)}{(p_a\cdot p_i)} - \frac{(p_a\cdot p_i)}{(p_a\cdot p_f)}\right]. \end{aligned} \tag{A.7}$$

Now, let us consider the effects due to the presence of plasma described in section 2.1.1. In particular, the expression in eq. (A.7) is modified by the screening of the electrostatic fields of the ions on which the electrons scatter, and by the correlation effects of the scattering sites. By using eq. (2.14), we

obtain the expression:

$$d\varepsilon = \frac{\alpha^2 g_{aee}^2 Z^2 n_N}{\pi^3} d\omega_i f_e(\omega_i, T) d\omega_f (1 - f_e(\omega_f, T)) \times$$
$$\times \frac{d\Omega_{e'}}{4\pi} \frac{d\Omega_a}{4\pi} \frac{|p_f||p_i|\omega_a^2}{\mathbf{q}^2(\mathbf{q}^2 + k_{\rm S}^2)} \left[2\omega_a^2 \frac{p_i \cdot p_f - m^2 - p_a \cdot (p_f - p_i)}{(p_a \cdot p_i)(p_a \cdot p_f)} + 2 - \frac{(p_a \cdot p_f)}{(p_a \cdot p_i)} - \frac{(p_a \cdot p_i)}{(p_a \cdot p_f)} \right] \tag{A.8}$$

This expression has to be compared with the one found by Raffelt in [29]. Note the different sign obtained for the $p_a \cdot (p_f - p_i)$ term. Now we address the explicit computation of the axion emissivity spectrum $d\varepsilon/d\omega_a$ in a white dwarf plasma due to axion-bremsstrahlung. In order to do so we can use the energy delta in eq. (A.6) to remove the integration over $d\omega_f$ and restore the $d\omega_a$. For later convenience, we label with $\mathcal{F}$ the quantity

$$\mathcal{F} = \frac{|p_f||p_i|\omega_a^2}{\mathbf{q}^2(\mathbf{q}^2 + k_{\rm S}^2)} \left[2\omega_a^2 \frac{p_i \cdot p_f - m^2 - p_a \cdot (p_f - p_i)}{(p_a \cdot p_i)(p_a \cdot p_f)} + 2 - \frac{(p_a \cdot p_f)}{(p_a \cdot p_i)} - \frac{(p_a \cdot p_i)}{(p_a \cdot p_f)} \right], \tag{A.9}$$

so that, integrating over the solid angles of the outgoing particles and over the possible energies of the incoming electron, the axion emissivity spectrum $d\varepsilon/d\omega_a$ is formally written as

$$\frac{d\varepsilon}{d\omega_a} = \frac{\alpha^2 g_{aee}^2 Z^2 n_N}{\pi^3} \int_{m_e}^{\infty} d\omega_i f_e(\omega_i, T)(1 - f_e(\omega_i - \omega_a, T)) \int \frac{d\Omega_{e'}}{4\pi} \int \frac{d\Omega_a}{4\pi} \mathcal{F}. \tag{A.10}$$

In order to evaluate eq. (A.9), we need to compute the various scalar products between particles momenta. The high electron degeneracy of white dwarfs allows some simplifications, since in this limit the term $f_e(\omega_i, T)(1 - f_e(\omega_i - \omega_a, T))$ has a sharp peak, setting $\omega_i \simeq \omega_f \simeq \omega_{\rm F}$ and $|\mathbf{p_i}| \simeq |\mathbf{p_f}| \simeq p_{\rm F}$ to the value of the Fermi energy and Fermi momentum respectively. Hence, for the typical condition of a white dwarf plasma, $\omega_a \ll \omega_i, \omega_f \simeq \omega_{\rm F}$. In this degenerate limit and taking as reference frame the one in which the heavy

nuclei are static, the important quantities to compute eq. (A.9) are written as:

$$\begin{aligned}
p_i \cdot p_a &= \omega_i\omega_a - |\mathbf{p_i}||\mathbf{p_a}|\cos\theta_{ia} \simeq \omega_{\rm F}\omega_a(1-\beta_{\rm F}c_{ia}),\\
p_f \cdot p_a &= \omega_f\omega_a - |\mathbf{p_f}||\mathbf{p_a}|\cos\theta_{fa} \simeq \omega_{\rm F}\omega_a(1-\beta_{\rm F}c_{fa}),\\
p_i \cdot p_f &= \omega_i\omega_f - |\mathbf{p_i}||\mathbf{p_f}|\cos\theta_{if} \simeq \omega_{\rm F}^2(1-\beta_{\rm F}c_{if}),\\
p_a \cdot (p_f - p_i) &\simeq \omega_a\omega_{\rm F}(\cancel{1}-\beta_{\rm F}c_{fa}-\cancel{1}+\beta_{\rm F}c_{ia}) = \omega_a\omega_{\rm F}\beta_{\rm F}(c_{ia}-c_{fa}),\\
m_e^2 &\simeq \omega_{\rm F}^2 - p_{\rm F}^2 = \omega_{\rm F}^2(1-\beta_{\rm F}^2),\\
|\mathbf{q}|^2 &\simeq 2p_{\rm F}^2(1-c_{if}),
\end{aligned}$$

where $\beta_{\rm F} = p_{\rm F}/\omega_{\rm F}$, $c_{kl} = \cos\theta_{kl}$ with θ_{kl} $k,l = i,f,a$ the relative angles between particles. By plugging these quantities in eq. (A.9), it is possible to notice that the term $p_a \cdot (p_f - p_i)$ carries an additional ω_a dependence, which is small in high degeneracy limit. Thus, this term is safely negligible for the axion-bremsstrahlung emissivity calculation, making the differences between the result in eq. (A.7) and the one calculated by Raffelt in [20] irrelevant in this context. We point out that a recent paper by Carenza and Lucente [89] has found the same result as ours. Here the important terms for the calculation are explicitly computed:

$$\begin{aligned}
2\omega_a^2\left[(p_i\cdot p_f) - m_e^2\right] &= 2\omega_a^2\omega_{\rm F}^2(1-\beta_{\rm F}c_{if}-1+\beta_{\rm F}^2) = 2\omega_a^2\omega_{\rm F}^2(\beta_{\rm F}^2 - c_{if}\beta_{\rm F}),\\
2(p_i\cdot p_a)(p_f\cdot p_a) &= 2\omega_a^2\omega_{\rm F}^2(1-\beta_{\rm F}c_{ia})(1-\beta_{\rm F}c_{fa}),\\
&= 2\omega_a^2\omega_{\rm F}^2\left[1-(c_{ia}+c_{fa})\beta_{\rm F} + (c_{ia}c_{fa})\beta_{\rm F}^2)\right],\\
-(p_f\cdot p_a)^2 &= -\omega_a^2\omega_{\rm F}^2(1-\beta_{\rm F}c_{ia})^2 = -\omega_a^2\omega_{\rm F}^2(1-2\beta_{\rm F}c_{ia}+c_{ia}^2\beta_{\rm F}^2),\\
-(p_f\cdot p_a)^2 &= -\omega_a^2\omega_{\rm F}^2(1-\beta_{\rm F}c_{fa})^2 = -\omega_a^2\omega_{\rm F}^2(1-2\beta_{\rm F}c_{fa}+c_{fa}^2\beta_{\rm F}^2).
\end{aligned}$$

Substituting these terms inside the expression of $\mathcal{F}$ we get

$$\begin{aligned}
\mathcal{F} =& \frac{|p_f||p_i|\omega_a^2}{\mathbf{q}^2(\mathbf{q}^2+k_{\rm S}^2)}\left[2\omega_a^2\frac{p_i\cdot p_f - m^2 - p_a\cdot(p_f-p_i)}{(p_a\cdot p_i)(p_a\cdot p_f)} + 2 - \frac{(p_a\cdot p_f)}{(p_a\cdot p_i)} - \frac{(p_a\cdot p_i)}{(p_a\cdot p_f)}\right] =\\
&\simeq \frac{\omega_a^2\beta_{\rm F}^2\left[2(1-c_{if})+(c_{ia}-c_{fa})^2\right]}{4p_{\rm F}^2(1-c_{if})(1-c_{if}+\kappa_{\rm s}^2)(1-\beta_{\rm F}c_{ia})(1-\beta_{\rm F}c_{fa})}\times\frac{m_e^2}{m_e^2}\\
&= \frac{\omega_a^2\left[2(1-c_{if})+(c_{ia}-c_{fa})^2\right]}{4(1-c_{if})(1-c_{if}+\kappa_{\rm s}^2)(1-\beta_{\rm F}c_{ia})(1-\beta_{\rm F}c_{fa})}\times\frac{1-\beta_{\rm F}^2}{m_e^2},
\end{aligned}$$

where we have defined the dimensionless quantity $\kappa_{\rm s}^2 = k_{\rm S}^2/2p_{\rm F}^2$. Plugging this

quantity back in eq. (A.10), we can express the axion emissivity as

$$\frac{d\varepsilon}{d\omega_a} = \frac{\alpha^2 g_{aee}^2 Z^2 n_N}{4\pi^3 m_e^2} \int_{m_e}^{\infty} d\omega_i \omega_a^2 \, f_e(\omega_i, T)(1 - f_e(\omega_i - \omega_a, T)) \times \\ \times \int \frac{d\Omega_{e'}}{4\pi} \int \frac{d\Omega_a}{4\pi} \frac{(1-\beta_{\rm F}^2)\left[2(1-c_{if}) + (c_{ia} - c_{fa})^2\right]}{(1-c_{if})(1-c_{if}+\kappa_{\rm s}^2)(1-\beta_{\rm F} c_{ia})(1-\beta_{\rm F} c_{fa})}.$$

Now we can use the fact that in the degenerate limit $T \ll p_{\rm F}$ and the integral over the incoming electron energy ω_i can be performed analytically [20], [72] and leads to

$$\frac{d\varepsilon}{d\omega_a} = \frac{\alpha^2 g_{aee}^2 Z^2 n_N}{4\pi^3 m_e^2} \frac{\omega_a^3}{e^{\omega_a/T} - 1} F, \tag{A.11}$$

where we have defined the dimensionless form factor F as

$$F = \int \frac{d\Omega_{e'}}{4\pi} \int \frac{d\Omega_a}{4\pi} \frac{(1-\beta_{\rm F}^2)\left[2(1-c_{if}) + (c_{ia} - c_{fa})^2\right]}{(1-c_{if})(1-c_{if}+\kappa_{\rm s}^2)(1-\beta_{\rm F} c_{ia})(1-\beta_{\rm F} c_{fa})}. \tag{A.12}$$

It is now possible to generalize the expression of the axion emissivity to the presence of multiple species. In fact, by using eq. (2.3) we can recast eq. (A.11) as

$$\frac{d\varepsilon}{d\omega_a} = \frac{\alpha^2 g_{aee}^2}{4\pi^3 m_e^2} \frac{\omega_a^3}{e^{\omega_a/T} - 1} \sum_s \frac{Z_s^2 \rho_s}{A_s m_u} F. \tag{A.13}$$

Appendix B

Axion-photon conversion probability

Consider the axion-photon mixing equations introduced in section 3.1.3:

$$\left[i\partial_r + \omega + \begin{pmatrix} \Delta_\parallel & \Delta_B \\ \Delta_B & \Delta_a \end{pmatrix}\right] \begin{pmatrix} A_\parallel \\ a \end{pmatrix} = 0, \tag{B.1}$$

we introduce the particle "state vector" Ψ such that

$$\Psi(r) = \begin{pmatrix} A_\parallel(r) \\ a(r) \end{pmatrix}. \tag{B.2}$$

With this substitution, the mixing equation resembles a Schrödinger equation for Ψ, where time has been replaced with a trajectory coordinate r:

$$\left[i\partial_r + \omega + \begin{pmatrix} \Delta_\parallel & \Delta_B \\ \Delta_B & \Delta_a \end{pmatrix}\right] \Psi(r) = 0. \tag{B.3}$$

Assuming the weak-mixing limit, we can apply the formalism of "time" perturbation theory. We define the Hamiltonian $H(r)$ as composed of a free part $H_0(r)$ and a perturbative interaction part $H_1(r)$, such that:

$$H_0(r) = -\begin{pmatrix} \omega + \Delta_\parallel(r) & 0 \\ 0 & \omega + \Delta_a \end{pmatrix}, \qquad H_1(r) = -\begin{pmatrix} 0 & \Delta_B(r) \\ \Delta_B(r) & 0 \end{pmatrix}. \tag{B.4}$$

This separation is motivated by the fact that we assume the mixing term Δ_B to be small compared to the diagonal terms in eq. (B.3), which is always

the case. With this separation, our mixing equations can be rewritten as:

$$i\partial_r \Psi(r) = \left[H_0(r) + H_1(r)\right] \Psi(r). \tag{B.5}$$

This naturally leads to describing the evolution of the state vector Ψ in the interaction picture. The transition to states and operators in the interaction picture is given by the following relations:

$$\begin{aligned} \Psi &= U_0 \Psi^{\text{int}}, \\ H_1^{\text{int}} &= U_0^\dagger H_1 U_0, \end{aligned} \tag{B.6}$$

where we have defined the time evolution operator for the "time"-dependent free Hamiltonian $H_0(r)$:

$$U_0(r) = \exp\left(-i \int_0^r H_0(r')dr'\right). \tag{B.7}$$

For simplicity, we have chosen the starting coordinate as $r_0 = 0$. For an arbitrary initial point, the limits of the integral in eq. (B.7) should be adjusted accordingly.

One can easily check that under these redefinitions, the axion-photon mixing equations are rewritten as:

$$i\partial_r \Psi^{\text{int}} = H_1^{\text{int}} \Psi^{\text{int}}. \tag{B.8}$$

The general solution to this equation is formally given by:

$$\Psi^{\text{int}}(r) = U(r)\Psi^{\text{int}}(0), \tag{B.9}$$

where $U(r)$ is the "time" evolution operator for H_1^{int}, which can be written as a *Dyson series*:

$$U(r) = \sum_{n=0}^{\infty} \frac{(-i)^n}{n!} \int_0^r dr_1 \cdots \int_0^r dr_n \mathcal{P}_r(H_1^{\text{int}}(r_1) \cdots H_1^{\text{int}}(r_n)), \tag{B.10}$$

and $\mathcal{P}_r$ is a path-ordering operator. Therefore, to first order in perturbation theory, the state vector can be approximated as:

$$\Psi^{\text{int}}(r) \simeq \left(\mathbb{I} - i \int_0^r dr' H_1^{\text{int}}(r')\right) \Psi(0), \tag{B.11}$$

where we used $\Psi^{\rm int}(0) = \Psi(0)$ and $\mathbb{I}$ is the identity matrix.

Returning to the Schrödinger picture, we write:

$$\Psi(r) = U_0(r)\left(\mathbb{I} - i\int_0^r dr' U_0^\dagger(r') H_1(r') U_0(r')\right)\Psi(0). \tag{B.12}$$

We now have all the ingredients to compute the axion-photon conversion probability for an axion that has traveled a distance r along its trajectory. Indeed, $p_{a\to\gamma}$ is calculated by squaring the transition amplitude of an initially pure axion state emerging as a photon at a distance r. Hence, the initial condition for the state vector is $\Psi(0) = (0,1)^T \equiv |a\rangle$, corresponding to a pure axion state. The final state we are interested in is a pure photon $(1,0)^T \equiv |\gamma\rangle$, thus:

$$\begin{aligned}\mathcal{A}_{a\to\gamma} = (1,0)\cdot\Psi(r) &= -i\,\langle\gamma|U_0(r)|\gamma\rangle\int_0^r dr'\langle\gamma|\left[U_0^\dagger(r')H_1(r')U_0(r')\right]|a\rangle \\ &= -i\,[U_0(r)]_{\gamma\gamma}\int_0^r dr'\exp\left(i\int_0^{r'} dr''(\Delta_a - \Delta_\parallel)\right)\Delta_B(r').\end{aligned} \tag{B.13}$$

Taking the square of the modulus, setting $r\to\infty$ and restoring $\mathrm{R_{WD}}$ as initial propagation point, we obtain:

$$p_{a\to\gamma} = \left|\int_{\mathrm{R_{WD}}}^\infty dr'\Delta_B(r')e^{i\Delta_a r' - \int_0^{r'} dr''\Delta_\parallel(r'')}\right|^2. \tag{B.14}$$

Bibliography

[1] K. Fujikawa, "Path-integral measure for gauge-invariant fermion theories", *Phys. Rev. Lett.*, vol. 42, pp. 1195–1198, 18 1979. DOI: 10.1103/PhysRevLett.42.1195. [Online]. Available: https://link.aps.org/doi/10.1103/PhysRevLett.42.1195.

[2] C. Abel, S. Afach, N. Ayres, *et al.*, "Measurement of the permanent electric dipole moment of the neutron", *Physical Review Letters*, vol. 124, no. 8, Feb. 2020. DOI: 10.1103/physrevlett.124.081803. [Online]. Available: http://dx.doi.org/10.1103/PhysRevLett.124.081803.

[3] C. A. Baker, D. D. Doyle, P. Geltenbort, *et al.*, "Improved experimental limit on the electric dipole moment of the neutron", *Physical Review Letters*, vol. 97, no. 13, Sep. 2006. DOI: 10.1103/physrevlett.97.131801. [Online]. Available: http://dx.doi.org/10.1103/PhysRevLett.97.131801.

[4] C. Vafa and E. Witten, "Parity conservation in quantum chromodynamics", *Phys. Rev. Lett.*, vol. 53, pp. 535–536, 6 1984. DOI: 10.1103/PhysRevLett.53.535. [Online]. Available: https://link.aps.org/doi/10.1103/PhysRevLett.53.535.

[5] L. Di Luzio, M. Giannotti, E. Nardi, *et al.*, "The landscape of qcd axion models", *Physics Reports*, vol. 870, 1–117, Jul. 2020. DOI: 10.1016/j.physrep.2020.06.002. [Online]. Available: http://dx.doi.org/10.1016/j.physrep.2020.06.002.

[6] R. D. Peccei and H. R. Quinn, "CP Conservation in the Presence of Instantons", *Phys. Rev. Lett.*, vol. 38, pp. 1440–1443, 1977. DOI: 10.1103/PhysRevLett.38.1440.

[7] R. D. Peccei and H. R. Quinn, "Constraints Imposed by CP Conservation in the Presence of Instantons", *Phys. Rev. D*, vol. 16, pp. 1791–1797, 1977. DOI: 10.1103/PhysRevD.16.1791.

[8] S. Weinberg, "A New Light Boson?", *Phys. Rev. Lett.*, vol. 40, pp. 223–226, 1978. DOI: 10.1103/PhysRevLett.40.223.

[9] F. Wilczek, "Problem of Strong P and T Invariance in the Presence of Instantons", *Phys. Rev. Lett.*, vol. 40, pp. 279–282, 1978. DOI: 10.1103/PhysRevLett.40.279.

[10] Y. Asano, E. Kikutani, S. Kurokawa, *et al.*, "A new experimental limit for the decay $K^+ \to \pi + \gamma\gamma$", *Physics Letters B*, vol. 113, no. 2, pp. 195–198, 1982. DOI: https://doi.org/10.1016/0370-2693(82)90423-3. [Online]. Available: https://www.sciencedirect.com/science/article/pii/0370269382904233.

[11] C. Edwards, R. Partridge, C. Peck, *et al.*, "Upper limit for $\frac{J}{\Psi} \to \gamma +$ *Axion*", *Phys. Rev. Lett.*, vol. 48, pp. 903–906, 14 1982. DOI: 10.1103/PhysRevLett.48.903. [Online]. Available: https://link.aps.org/doi/10.1103/PhysRevLett.48.903.

[12] M. Sivertz, J. Lee-Franzini, J. E. Horstkotte, *et al.*, "Upper limit for axion production in radiative Υ decay", *Phys. Rev. D*, vol. 26, pp. 717–719, 3 1982. DOI: 10.1103/PhysRevD.26.717. [Online]. Available: https://link.aps.org/doi/10.1103/PhysRevD.26.717.

[13] J. E. Kim, "Weak Interaction Singlet and Strong CP Invariance", *Phys. Rev. Lett.*, vol. 43, p. 103, 1979. DOI: 10.1103/PhysRevLett.43.103.

[14] M. A. Shifman, A. I. Vainshtein, and V. I. Zakharov, "Can Confinement Ensure Natural CP Invariance of Strong Interactions?", *Nucl. Phys. B*, vol. 166, pp. 493–506, 1980. DOI: 10.1016/0550-3213(80)90209-6.

[15] L. Di Luzio, F. Mescia, and E. Nardi, "Redefining the axion window", *Physical Review Letters*, vol. 118, no. 3, Jan. 2017. DOI: 10.1103/physrevlett.118.031801. [Online]. Available: http://dx.doi.org/10.1103/PhysRevLett.118.031801.

[16] L. Di Luzio, F. Mescia, and E. Nardi, "Window for preferred axion models", *Physical Review D*, vol. 96, no. 7, Oct. 2017. DOI: 10.1103/physrevd.96.075003. [Online]. Available: http://dx.doi.org/10.1103/PhysRevD.96.075003.

[17] V. Plakkot and S. Hoof, "Anomaly ratio distributions of hadronic axion models with multiple heavy quarks", *Physical Review D*, vol. 104, no. 7, Oct. 2021. DOI: 10.1103/physrevd.104.075017. [Online]. Available: http://dx.doi.org/10.1103/PhysRevD.104.075017.

[18] M. Dine, W. Fischler, and M. Srednicki, "A Simple Solution to the Strong CP Problem with a Harmless Axion", *Phys. Lett. B*, vol. 104, pp. 199–202, 1981. DOI: 10.1016/0370-2693(81)90590-6.

[19] A. R. Zhitnitsky, "On Possible Suppression of the Axion Hadron Interactions. (In Russian)", *Sov. J. Nucl. Phys.*, vol. 31, p. 260, 1980.

[20] G. G. Raffelt, *Stars as laboratories for fundamental physics: The astrophysics of neutrinos, axions, and other weakly interacting particles*. May 1996.

[21] G. G. Raffelt, "Astrophysical methods to constrain axions and other novel particle phenomena", *Physics Reports*, vol. 198, no. 1, pp. 1–113, 1990. DOI: https://doi.org/10.1016/0370-1573(90)90054-6. [Online]. Available: https://www.sciencedirect.com/science/article/pii/0370157390900546.

[22] J. P. Hansen, "Statistical mechanics of dense ionized matter. i. equilibrium properties of the classical one-component plasma", *Phys. Rev. A*, vol. 8, pp. 3096–3109, 6 1973. DOI: 10.1103/PhysRevA.8.3096. [Online]. Available: https://link.aps.org/doi/10.1103/PhysRevA.8.3096.

[23] S. Galam and J.-P. Hansen, "Statistical mechanics of dense ionized matter. vi. electron screening corrections to the thermodynamic properties of the one-component plasma", *Phys. Rev. A*, vol. 14, pp. 816–832, 2 1976. DOI: 10.1103/PhysRevA.14.816. [Online]. Available: https://link.aps.org/doi/10.1103/PhysRevA.14.816.

[24] G. G. di Cortona, E. Hardy, J. P. Vega, *et al.*, "The qcd axion, precisely", *Journal of High Energy Physics*, vol. 2016, no. 1, Jan. 2016. DOI: 10.1007/jhep01(2016)034. [Online]. Available: http://dx.doi.org/10.1007/JHEP01(2016)034.

[25] L. Di Luzio, M. Fedele, M. Giannotti, *et al.*, "Stellar evolution confronts axion models", *Journal of Cosmology and Astroparticle Physics*, vol. 2022, no. 02, p. 035, Feb. 2022. DOI: 10.1088/1475-7516/2022/02/035. [Online]. Available: http://dx.doi.org/10.1088/1475-7516/2022/02/035.

[26] A. Friedland, M. Giannotti, and M. Wise, "Constraining the axion-photon coupling with massive stars", *Physical Review Letters*, vol. 110, no. 6, Feb. 2013. DOI: 10.1103/physrevlett.110.061101. [Online]. Available: http://dx.doi.org/10.1103/PhysRevLett.110.061101.

[27] G. Raffelt and A. Caputo, "Astrophysical axion bounds: The 2024 edition", in *Proceedings of 1st General Meeting and 1st Training School of the COST Action COSMIC WSIPers — PoS(COSMICWISPers)*, ser. COSMICWISPers, Sissa Medialab, Mar. 2024. DOI: 10.22323/1.454.0041. [Online]. Available: http://dx.doi.org/10.22323/1.454.0041.

[28] O. Straniero, I. Dominguez, L. Piersanti, *et al.*, "The initial mass–final luminosity relation of type ii supernova progenitors: Hints of new physics?", *The Astrophysical Journal*, vol. 881, no. 2, p. 158, 2019. DOI: 10.3847/1538-4357/ab3222. [Online]. Available: https://dx.doi.org/10.3847/1538-4357/ab3222.

[29] G. G. Raffelt, "Axion bremsstrahlung in red giants", *Phys. Rev. D*, vol. 41, pp. 1324–1326, 1990. DOI: 10.1103/PhysRevD.41.1324.

[30] A. Pantziris and K. Kang, "Axion emission rates in stars and constraints on its mass", *Phys. Rev. D*, vol. 33, pp. 3509–3518, 12 1986. DOI: 10.1103/PhysRevD.33.3509. [Online]. Available: https://link.aps.org/doi/10.1103/PhysRevD.33.3509.

[31] S. Dimopoulos, J. A. Frieman, B. W. Lynn, *et al.*, "Axiorecombination: A New Mechanism for Stellar Axion Production", *Phys. Lett. B*, vol. 179, pp. 223–227, 1986. DOI: 10.1016/0370-2693(86)90570-8.

[32] J. Redondo, "Solar axion flux from the axion-electron coupling", *Journal of Cosmology and Astroparticle Physics*, vol. 2013, no. 12, 008–008, Dec. 2013. DOI: 10.1088/1475-7516/2013/12/008. [Online]. Available: http://dx.doi.org/10.1088/1475-7516/2013/12/008.

[33] P. Sikivie, "Experimental tests of the "invisible" axion", *Phys. Rev. Lett.*, vol. 51, pp. 1415–1417, 16 1983. DOI: 10.1103/PhysRevLett.51.1415. [Online]. Available: https://link.aps.org/doi/10.1103/PhysRevLett.51.1415.

[34] G. G. Raffelt and D. S. P. Dearborn, "Bounds on hadronic axions from stellar evolution", *Phys. Rev. D*, vol. 36, pp. 2211–2225, 8 1987. DOI: 10.1103/PhysRevD.36.2211. [Online]. Available: https://link.aps.org/doi/10.1103/PhysRevD.36.2211.

[35] P. Gondolo and G. G. Raffelt, "Solar neutrino limit on axions and kev-mass bosons", *Physical Review D*, vol. 79, no. 10, May 2009. DOI: 10.1103/physrevd.79.107301. [Online]. Available: http://dx.doi.org/10.1103/PhysRevD.79.107301.

[36] N. Vinyoles, A. Serenelli, F. Villante, *et al.*, "New axion and hidden photon constraints from a solar data global fit", *Journal of Cosmology and Astroparticle Physics*, vol. 2015, no. 10, 015–015, Oct. 2015. DOI: 10.1088/1475-7516/2015/10/015. [Online]. Available: http://dx.doi.org/10.1088/1475-7516/2015/10/015.

[37] M. C. Gonzalez-Garcia, M. Maltoni, J. P. Pinheiro, *et al.*, "Status of direct determination of solar neutrino fluxes after borexino", *Journal of High Energy Physics*, vol. 2024, no. 2, Feb. 2024. DOI: 10.1007/jhep02(2024)064. [Online]. Available: http://dx.doi.org/10.1007/JHEP02(2024)064.

[38] I. Irastorza, F. Avignone, S Caspi, *et al.*, "Towards a new generation axion helioscope", *Journal of Cosmology and Astroparticle Physics*, vol. 2011, no. 06, 013–013, Jun. 2011. DOI: 10.1088/1475-7516/2011/06/013. [Online]. Available: http://dx.doi.org/10.1088/1475-7516/2011/06/013.

[39] K. van Bibber, P. M. McIntyre, D. E. Morris, *et al.*, "Design for a practical laboratory detector for solar axions", *Phys. Rev. D*, vol. 39, pp. 2089–2099, 8 1989. DOI: 10.1103/PhysRevD.39.2089. [Online]. Available: https://link.aps.org/doi/10.1103/PhysRevD.39.2089.

[40] "New cast limit on the axion–photon interaction", *Nature Physics*, vol. 13, no. 6, 584–590, May 2017. DOI: 10.1038/nphys4109. [Online]. Available: http://dx.doi.org/10.1038/nphys4109.

[41] C. O'Hare, *Cajohare/axionlimits: Axionlimits*, https://cajohare.github.io/AxionLimits/, version v1.0, Jul. 2020. DOI: 10.5281/zenodo.3932430.

[42] K. Barth, A. Belov, B. Beltran, *et al.*, "Cast constraints on the axion-electron coupling", *Journal of Cosmology and Astroparticle Physics*, vol. 2013, no. 05, p. 010, 2013. DOI: 10.1088/1475-7516/2013/05/010. [Online]. Available: https://dx.doi.org/10.1088/1475-7516/2013/05/010.

[43] R. Buonanno, A. Buzzoni, C. E. Corsi, *et al.*, "High precision photometry of 10,000 stars in m 3", in *The Harlow-Shapley Symposium on Globular Cluster Systems in Galaxies*, J. E. Grindlay and A. G. Davis Philip, Eds., Dordrecht: Springer Netherlands, 1988, pp. 621–622.

[44] M. Haft, G. Raffelt, and A. Weiss, "Standard and nonstandard plasma neutrino emission revisited", *The Astrophysical Journal*, vol. 425, p. 222, Apr. 1994. DOI: 10.1086/173978. [Online]. Available: http://dx.doi.org/10.1086/173978.

[45] O. Straniero, C. Pallanca, E. Dalessandro, *et al.*, "The rgb tip of galactic globular clusters and the revision of the axion-electron coupling bound", *Astronomy & Astrophysics*, vol. 644, A166, Dec. 2020. DOI: 10.1051/0004-6361/202038775. [Online]. Available: http://dx.doi.org/10.1051/0004-6361/202038775.

[46] A. Ayala, I. Domínguez, M. Giannotti, *et al.*, "Revisiting the bound on axion-photon coupling from globular clusters", *Physical Review Letters*, vol. 113, no. 19, Nov. 2014. DOI: 10.1103/physrevlett.113.191302. [Online]. Available: http://dx.doi.org/10.1103/PhysRevLett.113.191302.

[47] O. Straniero, A. Ayala, M. Giannotti, *et al.*, "Axion-Photon Coupling: Astrophysical Constraints", in *11th Patras Workshop on Axions, WIMPs and WISPs*, 2015, pp. 77–81. DOI: 10.3204/DESY-PROC-2015-02/straniero_oscar.

[48] M. Giannotti, "Hints of new physics from stars", *PoS*, vol. ICHEP2016, p. 076, 2016. DOI: 10.22323/1.282.0076. arXiv: 1611.04651 [astro-ph.HE].

[49] M. M. Bertolami, B. Melendez, L. Althaus, *et al.*, "Revisiting the axion bounds from the galactic white dwarf luminosity function", *Journal of Cosmology and Astroparticle Physics*, vol. 2014, no. 10, 069–069, Oct. 2014. DOI: 10.1088/1475-7516/2014/10/069. [Online]. Available: http://dx.doi.org/10.1088/1475-7516/2014/10/069.

[50] H. C. Harris, J. A. Munn, M. Kilic, *et al.*, "The white dwarf luminosity function from sloan digital sky survey imaging data", *The Astronomical Journal*, vol. 131, no. 1, 571–581, Jan. 2006. DOI: 10.1086/497966. [Online]. Available: http://dx.doi.org/10.1086/497966.

[51] N. Rowell and N. Hambly, *White dwarfs in the supercosmos sky survey: The thin disk, thick disk and spheroid luminosity functions*, 2011. arXiv: 1102.3193 [astro-ph.GA].

[52] M. Giannotti, I. Irastorza, J. Redondo, *et al.*, "Cool wisps for stellar cooling excesses", *Journal of Cosmology and Astroparticle Physics*, vol. 2016, no. 05, p. 057, 2016. DOI: 10.1088/1475-7516/2016/05/057. [Online]. Available: https://dx.doi.org/10.1088/1475-7516/2016/05/057.

[53] A. H. Córsico, L. G. Althaus, M. M. Miller Bertolami, *et al.*, "Pulsating white dwarfs: New insights", *The Astronomy and Astrophysics Review*, vol. 27, no. 1, Sep. 2019. DOI: 10.1007/s00159-019-0118-4. [Online]. Available: http://dx.doi.org/10.1007/s00159-019-0118-4.

[54] S. O. Kepler, D. E. Winget, Z. P. Vanderbosch, *et al.*, "The pulsating white dwarf g117-b15a: Still the most stable optical clock known", *The Astrophysical Journal*, vol. 906, no. 1, p. 7, Dec. 2020. DOI: 10.3847/1538-4357/abc626. [Online]. Available: http://dx.doi.org/10.3847/1538-4357/abc626.

[55] L. Ferrario and D. T. Wickramasinghe, "Magnetic fields and rotation in white dwarfs and neutron stars", *Monthly Notices of the Royal Astronomical Society*, vol. 356, no. 2, pp. 615–620, Jan. 2005. DOI: 10.1111/j.1365-2966.2004.08474.x. eprint: https://academic.oup.com/mnras/article-pdf/356/2/615/3975704/356-2-615.pdf. [Online]. Available: https://doi.org/10.1111/j.1365-2966.2004.08474.x.

[56] L. Ferrario, D. de Martino, and B. T. Gänsicke, "Magnetic white dwarfs", *Space Science Reviews*, vol. 191, no. 1–4, 111–169, May 2015. DOI: 10.1007/s11214-015-0152-0. [Online]. Available: http://dx.doi.org/10.1007/s11214-015-0152-0.

[57] J. Bilíková, Y.-H. Chu, R. A. Gruendl, *et al.*, "Hard x-ray emission associated with white dwarfs. iii.", *The Astronomical Journal*, vol. 140, no. 5, p. 1433, 2010. DOI: 10.1088/0004-6256/140/5/1433. [Online]. Available: https://dx.doi.org/10.1088/0004-6256/140/5/1433.

[58] I. J. O'Dwyer, Y.-H. Chu, R. A. Gruendl, *et al.*, "Hard X-Ray Emission Associated with White Dwarfs",, vol. 125, no. 4, pp. 2239–2254, Apr. 2003. DOI: 10.1086/373929. arXiv: astro-ph/0301275 [astro-ph].

[59] C. Dessert, A. J. Long, and B. R. Safdi, "X-ray signatures of axion conversion in magnetic white dwarf stars", *Physical Review Letters*, vol. 123, no. 6, Aug. 2019. DOI: 10.1103/physrevlett.123.061104. [Online]. Available: http://dx.doi.org/10.1103/PhysRevLett.123.061104.

[60] D. Saumon, S. Blouin, and P.-E. Tremblay, "Current challenges in the physics of white dwarf stars", *Physics Reports*, vol. 988, 1–63, Nov. 2022. DOI: 10.1016/j.physrep.2022.09.001. [Online]. Available: http://dx.doi.org/10.1016/j.physrep.2022.09.001.

[61] M. Nakagawa, Y. Kohyama, and N. Itoh, "Axion Bremsstrahlung in Dense Stars", *Astrophys. J.*, vol. 322, p. 291, 1987. DOI: 10.1086/165724.

[62] M. Nakagawa, T. Adachi, Y. Kohyama, *et al.*, "Axion Bremsstrahlung in Dense Stars. II. Phonon Contributions",, vol. 326, p. 241, Mar. 1988. DOI: 10.1086/166085.

[63] W. L. Slattery, G. D. Doolen, and H. E. DeWitt, "Improved equation of state for the classical one-component plasma", *Phys. Rev. A*, vol. 21, pp. 2087–2095, 6 1980. DOI: 10.1103/PhysRevA.21.2087. [Online]. Available: https://link.aps.org/doi/10.1103/PhysRevA.21.2087.

[64] W. L. Slattery, G. D. Doolen, and H. E. DeWitt, "N dependence in the classical one-component plasma monte carlo calculations", *Phys. Rev. A*, vol. 26, pp. 2255–2258, 4 1982. DOI: 10.1103/PhysRevA.26.2255. [Online]. Available: https://link.aps.org/doi/10.1103/PhysRevA.26.2255.

[65] G. Raffelt and L. Stodolsky, "Mixing of the photon with low-mass particles", *Phys. Rev. D*, vol. 37, pp. 1237–1249, 5 1988. DOI: 10.1103/PhysRevD.37.1237. [Online]. Available: https://link.aps.org/doi/10.1103/PhysRevD.37.1237.

[66] A. J. Millar, G. G. Raffelt, J. Redondo, *et al.*, "Dielectric haloscopes to search for axion dark matter: Theoretical foundations", *Journal of Cosmology and Astroparticle Physics*, vol. 2017, no. 01, 061–061, Jan.

2017. DOI: 10.1088/1475-7516/2017/01/061. [Online]. Available: http://dx.doi.org/10.1088/1475-7516/2017/01/061.

[67] C. Biggio, E. Massó, and J. Redondo, "Mixing of photons with massive spin-two particles in a magnetic field", *Physical Review D*, vol. 79, no. 1, Jan. 2009. DOI: 10.1103/physrevd.79.015012. [Online]. Available: http://dx.doi.org/10.1103/PhysRevD.79.015012.

[68] G. Cowan, K. Cranmer, E. Gross, *et al.*, "Asymptotic formulae for likelihood-based tests of new physics", *The European Physical Journal C*, vol. 71, no. 2, Feb. 2011. DOI: 10.1140/epjc/s10052-011-1554-0. [Online]. Available: http://dx.doi.org/10.1140/epjc/s10052-011-1554-0.

[69] P. A. Zyla *et al.*, "Review of Particle Physics", *PTEP*, vol. 2020, no. 8, p. 083C01, 2020. DOI: 10.1093/ptep/ptaa104.

[70] S. S. Wilks, "The Large-Sample Distribution of the Likelihood Ratio for Testing Composite Hypotheses", *Annals Math. Statist.*, vol. 9, no. 1, pp. 60–62, 1938. DOI: 10.1214/aoms/1177732360.

[71] A. Wald, "Tests of statistical hypotheses concerning several parameters when the number of observations is large", *Transactions of the American Mathematical Society*, vol. 54, pp. 426–482, 1943. [Online]. Available: https://api.semanticscholar.org/CorpusID:54174575.

[72] C. Dessert, A. J. Long, and B. R. Safdi, "No evidence for axions from chandra observation of the magnetic white dwarf re j0317-853", *Physical Review Letters*, vol. 128, no. 7, Feb. 2022. DOI: 10.1103/physrevlett.128.071102. [Online]. Available: http://dx.doi.org/10.1103/PhysRevLett.128.071102.

[73] S. J. Kleinman, S. O. Kepler, D. Koester, *et al.*, "Sdss dr7 white dwarf catalog", *The Astrophysical Journal Supplement Series*, vol. 204, no. 1, p. 5, Dec. 2012. DOI: 10.1088/0067-0049/204/1/5. [Online]. Available: http://dx.doi.org/10.1088/0067-0049/204/1/5.

[74] A. G. A. Brown, A. Vallenari, T. Prusti, *et al.*, "Gaia data release 2: Summary of the contents and survey properties", *Astronomy & Astrophysics*, vol. 616, A1, Aug. 2018. DOI: 10.1051/0004-6361/201833051. [Online]. Available: http://dx.doi.org/10.1051/0004-6361/201833051.

[75] B. Külebi, S. Jordan, E. Nelan, *et al.*, "Constraints on the origin of the massive, hot, and rapidly rotating magnetic white dwarf re j 0317-853 from an hst parallax measurement", *Astronomy & Astrophysics*, vol. 524, A36, Nov. 2010. DOI: 10.1051/0004-6361/201015237. [Online]. Available: http://dx.doi.org/10.1051/0004-6361/201015237.

[76] M. A. Barstow, S. Jordan, D. O'Donoghue, *et al.*, "RE J0317 – 853: the hottest known highly magnetic DA white dwarf", *Monthly Notices of the Royal Astronomical Society*, vol. 277, no. 3, pp. 971–985, Dec. 1995. DOI: 10.1093/mnras/277.3.971. eprint: https://academic.oup.com/mnras/article-pdf/277/3/971/3775474/mnras277-0971.pdf. [Online]. Available: https://doi.org/10.1093/mnras/277.3.971.

[77] M. R. Burleigh, S. Jordan, and W. Schweizer, "Phase-resolved far-ultraviolet [ital]hubble space telescope[/ital] spectroscopy of the peculiar magnetic white dwarf re j0317-853", *The Astrophysical Journal*, vol. 510, no. 1, L37–L40, Jan. 1999. DOI: 10.1086/311794. [Online]. Available: http://dx.doi.org/10.1086/311794.

[78] L. Ferrario, S. Vennes, D. T. Wickramasinghe, *et al.*, "EUVE J0317 — 855: a rapidly rotating, high-field magnetic white dwarf", *Monthly Notices of the Royal Astronomical Society*, vol. 292, no. 2, pp. 205–217, Dec. 1997. DOI: 10.1093/mnras/292.2.205. eprint: https://academic.oup.com/mnras/article-pdf/292/2/205/18249895/292-2-205.pdf. [Online]. Available: https://doi.org/10.1093/mnras/292.2.205.

[79] A. G. A. Brown, A. Vallenari, T. Prusti, *et al.*, "Gaia early data release 3: Summary of the contents and survey properties (corrigendum)", *Astronomy & Astrophysics*, vol. 650, p. C3, Jun. 2021. DOI: 10.1051/0004-6361/202039657e. [Online]. Available: http://dx.doi.org/10.1051/0004-6361/202039657e.

[80] M. E. Camisassa, L. G. Althaus, A. H. Córsico, *et al.*, "The evolution of ultra-massive white dwarfs", *Astronomy & Astrophysics*, vol. 625, A87, May 2019. DOI: 10.1051/0004-6361/201833822. [Online]. Available: http://dx.doi.org/10.1051/0004-6361/201833822.

[81] A. Rohatgi, *Webplotdigitizer*, version 4.7, 2024. [Online]. Available: https://automeris.io/WebPlotDigitizer.html.

[82] S. K. Lam, A. Pitrou, and S. Seibert, "Numba: A llvm-based python jit compiler", in *Proceedings of the Second Workshop on the LLVM Compiler Infrastructure in HPC*, ser. LLVM '15, Austin, Texas: Association for Computing Machinery, 2015. DOI: 10.1145/2833157.2833162. [Online]. Available: https://doi.org/10.1145/2833157.2833162.

[83] Chandra X-ray Center, *The Chandra Proposers' Observatory Guide, Version 26.0*, http://cxc.cfa.harvard.edu/proposer/POG/, Chandra X-ray Center (CXC), Cambridge, MA, 2023.

[84] F. N. Fritsch and J. Butland, "A method for constructing local monotone piecewise cubic interpolants", *SIAM Journal on Scientific and Statistical Computing*, vol. 5, no. 2, pp. 300–304, 1984. DOI: 10.1137/0905021. eprint: https://doi.org/10.1137/0905021. [Online]. Available: https://doi.org/10.1137/0905021.

[85] A. Fruscione, J. C. McDowell, G. E. Allen, *et al.*, "CIAO: Chandra's data analysis system", in *Observatory Operations: Strategies, Processes, and Systems*, D. R. Silva and R. E. Doxsey, Eds., International Society for Optics and Photonics, vol. 6270, SPIE, 2006, p. 62701V. DOI: 10.1117/12.671760. [Online]. Available: https://doi.org/10.1117/12.671760.

[86] P. Virtanen, R. Gommers, T. Oliphant, *et al.*, "Scipy 1.0: Fundamental algorithms for scientific computing in python", *Nature Methods*, vol. 17, pp. 1–12, Feb. 2020. DOI: 10.1038/s41592-019-0686-2.

[87] P. Lipari, "The origin of the power–law form of the extragalactic gamma–ray flux", *Astroparticle Physics*, vol. 125, p. 102 507, 2021. DOI: https://doi.org/10.1016/j.astropartphys.2020.102507. [Online]. Available: https://www.sciencedirect.com/science/article/pii/S0927650520300797.

[88] W. Kluzniak and J. R. Wilson, "Hard X-Rays with a Power Law Spectrum from a Neutron Star Accreting Through the Relativistic Gap", in *Two Topics in X-Ray Astronomy, Volume 1: X Ray Binaries. Volume 2: AGN and the X Ray Background*, J. Hunt and B. Battrick, Eds., ser. ESA Special Publication, vol. 1, Nov. 1989, p. 477.

[89] P. Carenza and G. Lucente, "Revisiting axion-electron bremsstrahlung emission rates in astrophysical environments", *Physical Review D*, vol. 103, no. 12, Jun. 2021. DOI: 10.1103/physrevd.103.123024. [Online]. Available: http://dx.doi.org/10.1103/PhysRevD.103.123024.

[90] L. Darmé, L. Di Luzio, M. Giannotti, *et al.*, "Selective enhancement of the qcd axion couplings", *Physical Review D*, vol. 103, no. 1, Jan. 2021. DOI: 10.1103/physrevd.103.015034. [Online]. Available: http://dx.doi.org/10.1103/PhysRevD.103.015034.

[91] L. Di Luzio, B. Gavela, P. Quilez, *et al.*, "An even lighter qcd axion", *Journal of High Energy Physics*, vol. 2021, no. 5, May 2021. DOI: 10.1007/jhep05(2021)184. [Online]. Available: http://dx.doi.org/10.1007/JHEP05(2021)184.

[92] S. Moriyama, "Proposal to search for a monochromatic component of solar axions using ^{57}Fe", *Phys. Rev. Lett.*, vol. 75, pp. 3222–3225, 18 1995. DOI: 10.1103/PhysRevLett.75.3222. [Online]. Available: https://link.aps.org/doi/10.1103/PhysRevLett.75.3222.

[93] L. Di Luzio *et al.*, "Probing the axion–nucleon coupling with the next generation of axion helioscopes", *Eur. Phys. J. C*, vol. 82, no. 2, p. 120, 2022. DOI: 10.1140/epjc/s10052-022-10061-1. arXiv: 2111.06407 [hep-ph].

[94] L. Fleury, I. Caiazzo, and J. Heyl, "Constraining axions with ZTF J1901+1458", *Phys. Rev. D*, vol. 107, no. 10, p. L101303, 2023. DOI: 10.1103/PhysRevD.107.L101303. arXiv: 2208.00405 [astro-ph.HE].

[95] V. Shtabovenko, R. Mertig, and F. Orellana, "Feyncalc 9.3: New features and improvements", *Computer Physics Communications*, vol. 256, p. 107 478, Nov. 2020. DOI: 10.1016/j.cpc.2020.107478. [Online]. Available: http://dx.doi.org/10.1016/j.cpc.2020.107478.

[96] S. Weinberg, "The u(1) problem", *Phys. Rev. D*, vol. 11, pp. 3583–3593, 12 1975. DOI: 10.1103/PhysRevD.11.3583. [Online]. Available: https://link.aps.org/doi/10.1103/PhysRevD.11.3583.

[97] R. L. Workman *et al.*, "Review of Particle Physics", *PTEP*, vol. 2022, p. 083C01, 2022. DOI: 10.1093/ptep/ptac097.

[98] S. S. Wilks, "The Large-Sample Distribution of the Likelihood Ratio for Testing Composite Hypotheses", *The Annals of Mathematical Statistics*, vol. 9, no. 1, pp. 60 –62, 1938. DOI: 10.1214/aoms/1177732360. [Online]. Available: https://doi.org/10.1214/aoms/1177732360.

[99] G. Colonna and A. Laricchiuta, "Thermodynamic and transport properties of equilibrium debye plasmas", *Entropy*, vol. 22, p. 237, Feb. 2020. DOI: 10.3390/e22020237.

[100] M. Marsh, J. H. Matthews, C. Reynolds, *et al.*, "Fourier formalism for relativistic axion-photon conversion with astrophysical applications", *Physical Review D*, vol. 105, no. 1, Jan. 2022. DOI: 10.1103/physrevd.105.016013. [Online]. Available: http://dx.doi.org/10.1103/PhysRevD.105.016013.

[101] S. Asztalos, E. Daw, H. Peng, *et al.*, "Large-scale microwave cavity search for dark-matter axions", *Phys. Rev. D*, vol. 64, p. 092 003, 9 2001. DOI: 10.1103/PhysRevD.64.092003. [Online]. Available: https://link.aps.org/doi/10.1103/PhysRevD.64.092003.

[102] G. G. Raffelt, "Astrophysical axion bounds diminished by screening effects", *Phys. Rev. D*, vol. 33, pp. 897–909, 4 1986. DOI: 10.1103/PhysRevD.33.897. [Online]. Available: https://link.aps.org/doi/10.1103/PhysRevD.33.897.